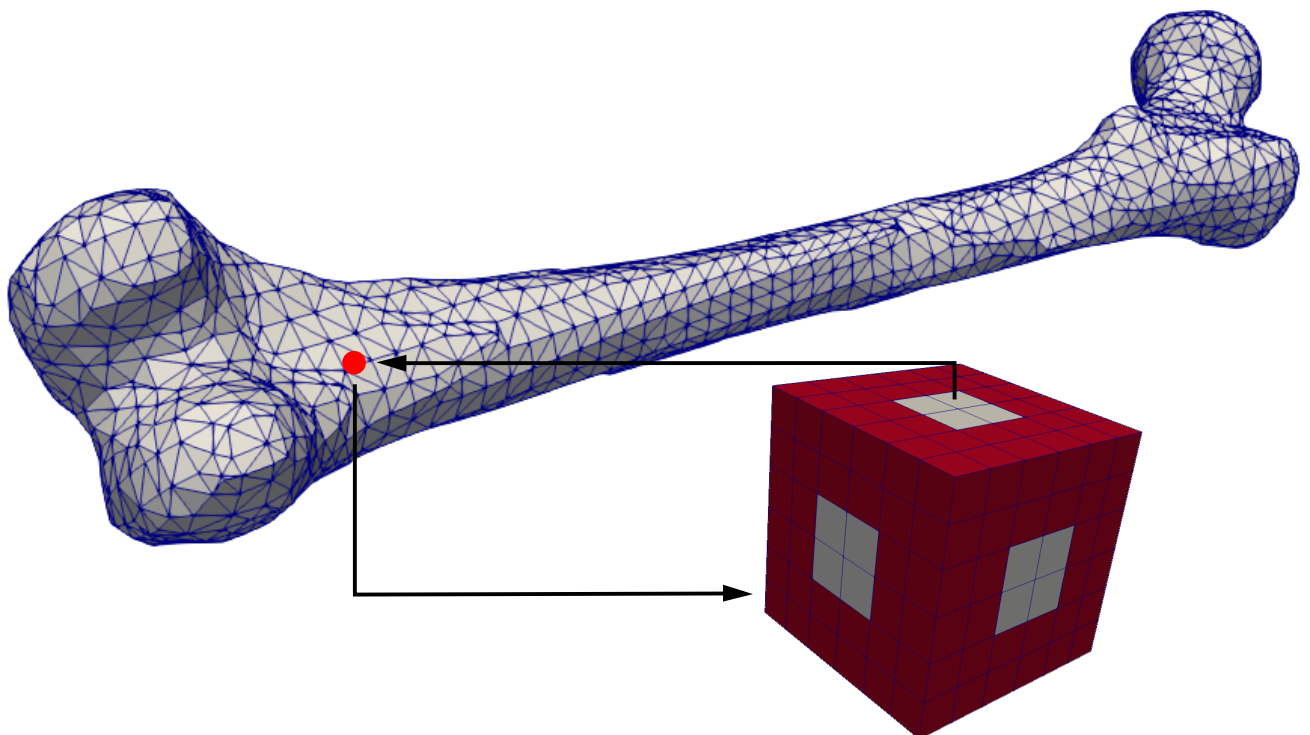


Forward and inverse multiscale modeling of bone considering the full coupling of mechanical, electric and magnetic effects

Mischa Blaszczyk



Forward and inverse multiscale modeling of bone considering the full coupling of mechanical, electric, and magnetic effects

Dissertation zur Erlangung des Grades

Doktor-Ingenieur

der Fakultät für Maschinenbau
der Ruhr-Universität Bochum

von

Mischa Blaszczyk
aus Recklinghausen

Bochum 2024

Herausgeber (publisher):

Institut für Mechanik
— Schriftenreihe —
Ruhr-Universität Bochum
D-44780 Bochum

ISBN 978-3-935892-74-2

This material is presented to ensure timely dissemination of scholarly and technical work. Copyright and all rights therein are retained by the copyright holders. All persons copying this information are expected to adhere to the terms and constraints invoked by the author's copyright. These works or parts of it may not be used to repost reprint/republish or for creating new collective works for resale or redistribution to servers or lists without the explicit permission of the copyright holder.

Dieses Werk ist urheberrechtlich geschützt. Die dadurch begründeten Rechte, insbesondere die der Übersetzung, des Nachdrucks, des Vortrags, der Entnahme von Abbildungen und Tabellen, der Funksendung, der Mikroverfilmung oder der Vervielfältigung auf anderen Wegen und der Speicherung in Datenverarbeitungsanlagen, bleiben, auch bei nur auszugsweiser Verwertung, vorbehalten. Eine Vervielfältigung dieses Werkes oder von Teilen dieses Werkes ist zulässig. Sie ist grundsätzlich vergütungspflichtig. Zuwiderhandlungen unterliegen den Strafbestimmungen des Urheberrechtsgesetzes.

©2024 Mischa Blaszczyk, Institut für Mechanik der Ruhr-Universität Bochum

Printed in Germany

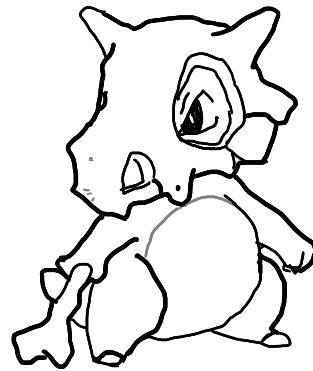
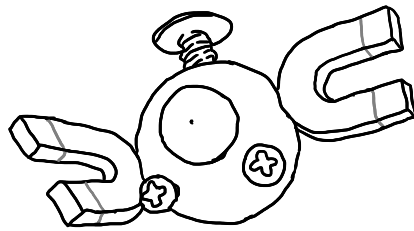
Einreichung der Dissertation (thesis submission): 24. Mai 2024

Tag der mündlichen Prüfung (thesis defense): 07. Oktober 2024

Erster Gutachter (first referee): Prof. Dr. rer. nat. Klaus Hackl

Zweiter Gutachter (second referee): Prof. Dr.-Ing. habil. Sandra Klinge

Vorsitzender (committee chair): Prof. Dr. Alexander Hartmaier



M.B.

für meine Eltern

"I do not know what I may appear to the world, but to myself I seem to have been only like a boy playing on the sea-shore, and diverting myself in now and then finding a smoother pebble or a prettier shell than ordinary, whilst the great ocean of truth lay all undiscovered before me." - Isaac Newton

Danksagung

Die vorliegende Dissertation ist während meiner Tätigkeit am Lehrstuhl für Mechanik – Materialtheorie unter der Leitung von Prof. Dr. rer. nat. Klaus Hackl im Zeitraum von 2019 bis 2024 entstanden.

Zunächst möchte ich mich bei meinem Doktorvater Prof. Dr. rer. nat. Klaus Hackl für die Möglichkeit bedanken, an seinem Institut und unter seiner Betreuung arbeiten zu dürfen. Seine Art und Weise, mir gleichzeitig den nötigen Freiraum und das Vertrauen für meine eigenen Ideen zu geben und bei Fragen und Problemen immer als zuverlässiger Ansprechpartner zur Verfügung zu stehen, schätze ich sehr. Die familiäre Atmosphäre am Institut verdanken wir nicht zuletzt der Art und Weise seiner Institutsleitung. Dr.-Ing. Ulrich Hoppe stand mir stets bei jeglichen Fragen zur Verfügung. Seine administrativen Tätigkeiten und seine häufig einfach nachvollziehbaren Erklärungen selbst bei komplexen Sachverhalten sind eine große Bereicherung für unser Institut.

Als nächstes möchte ich mich bei meinen aktuellen und ehemaligen Arbeitskollegen Hendrik, Kerem, Christopher, Sarah, Ghina, Golnaz, Barbara, Julia, Asim, Stephan, Dustin, Philipp, Minh, Piao, Prof. Yiqian He, Prof. Robert Gilbert und Prof. Dr.-Ing. Johanna Waimann für die gemeinsame Zeit bedanken. Durch die Arbeit in der Wissenschaft bin ich insbesondere mit der Ferrite-Community und den Gamm Juniors in Berührung gekommen. Diese Gemeinschaften, welche mich nicht nur in meiner fachlichen, sondern auch meiner menschlichen Entwicklung erheblich weitergebracht haben, haben mir zudem nach der Corona-Pandemie gezeigt, wie wichtig und ertragreich Austausch und Teamwork in der Wissenschaft sind.

An dieser Stelle möchte ich mich bei all meinen Bekannten und Freunden für die gemeinsame Zeit und die Unterstützung bedanken, von denen ich einige besonders hervorheben möchte: Den MB-Achter, die ehemaligen Hiwis, die ega-Jungs, Team Kolk, die Boulder-Connection, die Lego-Jungs, die Flüchtlingshilfe Sprockhövel, meine beste Freundin Marie und meinen besten Freund Rolf.

Zuletzt möchte ich mich bei meinen Geschwistern Jana und Yannik und meinen Eltern Sabine und Ralf bedanken, auf deren Liebe und Unterstützung ich mich stets verlassen konnte und welche mir immer die Möglichkeit gegeben haben, mich frei entfalten zu können.

Mischa Blaszczyk - Bochum, 2024

Summary

Osteoporosis is the most common bone disease worldwide. It is particularly prevalent in the elderly population. The disease is characterized by a reduction in bone density over its course. This results in a reduction of bone strength, thereby increasing the likelihood of fractures. Sonography may be a promising future diagnostic method for the early detection of osteoporosis, as it is less invasive and less costly compared to current standards. Modeling and simulations are useful tools to support the development of this diagnostic method and to better understand effects observed in measurements.

This cumulative thesis reports the research progress on the development of a multiscale material model for cancellous bone. The primary objective of this work is the solution of the forward and inverse problem of bone modeling that can be used for the early detection of osteoporosis by sonography. The content of this thesis is given through three research articles published by the author (and his coauthors), and presented in the following.

The first part of this thesis is devoted to the development of the material model. Due to the heterogeneous structure of cancellous bone, a multiscale approach consisting of macroscale and microscale is employed. On the microscale, a distinction is made between the phases cortical bone and bone marrow. The main novelty of the material model is the consideration of the full coupling of mechanical, electric, and magnetic effects, including Maxwell's equations. A thermodynamically consistent material model is derived from energy methods in mechanics. The solution of the resulting coupled partial differential equations (forward problem) is carried out using the finite element square method (FE²). Representative volume elements (RVE) with different volume percentages of cortical bone were constructed to simulate different stages of osteoporosis. The magnetic field strength resulting from a small mechanical displacement is determined for various models.

The second part of this thesis addresses the solution of the inverse problem. In order to draw conclusions about the bone health, it is necessary to determine the volume percentage of cortical bone from the magnetic field strength. A synthetic dataset was constructed from simulation results. Subsequently, the data was utilized as input for artificial neural networks (ANN). The objective of the networks' training is to identify the bone structure used in the simulation.

The third part is concerned with significant extensions to the model. On the one hand the simulation domain is extended to also include a surrounding medium. Consequently, the investigation of the decay of the electromagnetic fields beyond the simulated bone model is enabled. On the other hand a distinction is made between different bone phases on the macroscale. This improves the applicability and closeness to reality of the simulations.

Kurzfassung

Osteoporose ist die am weitesten verbreitete Knochenkrankheit weltweit. Sie kommt insbesondere bei der älteren Bevölkerung vor. Die Krankheit zeichnet sich durch eine Reduktion der Knochendichte über ihren Verlauf aus. Dies führt zu einer Verringerung der Knochenfestigkeit, dadurch steigt die Wahrscheinlichkeit für Knochenbrüche. Sonographie könnte ein vielversprechendes zukünftiges Diagnoseverfahren für die Früherkennung von Osteoporose darstellen, da es weniger invasiv und weniger kostenträchtig ist als aktuelle Standards. Modellierung und Simulation sind nützliche Hilfsmittel um die Entwicklung dieses Diagnoseverfahrens zu unterstützen und um bei Messungen beobachtete Effekte besser zu verstehen.

Diese kumulative Doktorarbeit berichtet über den Forschungsfortschritt bei der Entwicklung eines Materialmodells für spongiösen Knochen. Das vorrangige Ziel dieser Arbeit ist die Lösung des direkten und inversen Problems der Knochenmodellierung, welches zur Früherkennung von Osteoporose mittels Sonographie verwendet werden kann. Der Inhalt dieser Arbeit ist in Form von drei Fachzeitschriftenartikeln gegeben, welche von dem Autor (und seinen Koautoren) veröffentlicht wurden und wird im Folgenden präsentiert.

Der erste Teil dieser Arbeit wird für die Entwicklung des Materialmodells verwendet. Aufgrund der heterogenen Struktur von spongiösem Knochen wird ein Mehrskalensatz bestehend aus Makroskala und Mikroskala angewendet. Auf der Mikroskala wird zwischen den Phasen kortikaler Knochen und Knochenmark unterschieden. Die wesentliche Novität des Materialmodells ist die Berücksichtigung der vollständigen Kopplung von mechanischen, elektrischen und magnetischen Effekten, inklusive der Maxwell-Gleichungen. Ein thermodynamisch konsistentes Materialmodell basierend auf Energiemethoden der Mechanik wird hergeleitet. Die Lösung der resultierenden gekoppelten partiellen Differentialgleichungen (direktes Problem) wird mittels der Finite Elemente Square Methode (FE^2) realisiert. Repräsentative Volumenelemente (RVE) mit verschiedenen Volumenprozent-Anteilen von kortikalem Knochen wurden entworfen, um die verschiedenen Stufen von Osteoporose zu simulieren. Die Stärke des Magnetfeldes, welches aus einer kleinen mechanischen Belastung resultiert, wurde für unterschiedliche Modelle ermittelt.

Der zweite Teil dieser Arbeit behandelt die Lösung des inversen Problems. Um Rückschlüsse auf den Gesundheitszustand des Knochens zu ziehen, ist es notwendig, den Volumenprozent-Anteil von kortikalem Knochen aus der Stärke des Magnetfeldes zu ermitteln. Ein synthetischer Datensatz wurde aus Simulationsergebnissen erzeugt. Anschließend wurden diese Daten als Input für Künstliche neuronale Netzwerke (KNN, engl. ANN) genutzt. Das Ziel des Trainings der Netzwerke ist es, die Knochenstruktur zu ermitteln, welche in der Simulation verwendet wurde.

Der dritte Teil befasst sich mit wichtigen Erweiterungen des Modells. Zum einen wird der Simulationsbereich ausgeweitet, um zusätzlich auch ein Umgebungsmedium zu berücksichtigen. Dadurch wird die Untersuchung des Abfalls der elektromagnetischen Felder über

das simulierte Knochenmodell hinaus ermöglicht. Zum anderen wird auf der Makroskala zwischen verschiedenen Knochenphasen unterschieden. Dies erhöht die Anwendbarkeit und Realitätsnähe der Simulationen.

List of Publications

The present dissertation is a cumulative thesis consisting of the journal articles listed below. Furthermore, the contributions of the individual authors are listed there. The usage of a publication is indicated at the beginning of each respective chapter. In the case that further thematically related publications of the author were used, this is indicated by a citation, so that the publication is listed in the bibliography at the end of this thesis. A comprehensive list of all of the authors publications can be found at the end of this thesis in the Chapter Lebenslauf (CV).

1. Blaszczyk M. and Hackl K. (2022). Multiscale modeling of cancellous bone considering full coupling of mechanical, electric and magnetic effects. *Biomechanics and Modeling in Mechanobiology* 21(1), 163-187.
M. Blaszczyk: derivation of the mathematical model, methodology, development and programming of software framework, analysis of simulation results, writing (original draft)
K. Hackl: conceptualization, supervision, writing (review)
2. Stieve V., Blaszczyk M. and Hackl K. (2022). Inverse modeling of cancellous bone using artificial neural networks. *ZAMM-Journal of Applied Mathematics and Mechanics/Zeitschrift für Angewandte Mathematik und Mechanik* 102(6), e202100541.
V. Stieve: programming of the ANNs, analysis of results, writing (original draft)
M. Blaszczyk: methodology, programming of the code for data collection, supervision, writing (original draft and review)
K. Hackl: conceptualization, writing (review)
3. Blaszczyk M. and Hackl K. (2024). On the effects of a surrounding medium and phase split in coupled bone simulations. *ZAMM-Journal of Applied Mathematics and Mechanics/Zeitschrift für Angewandte Mathematik und Mechanik* 104(5), e202200595.
M. Blaszczyk: conceptualization, methodology, programming, analysis of results, writing (original draft)
K. Hackl: writing (review)

Contents

1	Introduction	1
1.1	Motivation	1
1.2	State of the art	3
1.2.1	Electromechanically coupled modeling	4
1.2.2	Mechanical modeling of bone	6
1.2.3	Multiphysics modeling of bone	7
1.2.4	Multiscale modeling	8
1.2.5	Artificial neural networks	11
1.3	Outline of the dissertation	12
1.4	Conclusion and outlook	15
2	Article 1: Multiscale modeling of cancellous bone considering full coupling of mechanical, electric and magnetic effects	19
2.1	Abstract	20
2.2	Introduction	20
2.3	Material model	22
2.3.1	Structure and properties of cancellous bone	22
2.3.2	Concept of the FE ² method	23
2.3.3	Variational formulation of the microscale problem	23
2.3.4	Weak and strong form of the microscale problem	26
2.3.5	Macroscale problem	27
2.4	Numerical implementation	28
2.4.1	Finite element method	28
2.4.2	Transition between the scales	31
2.4.3	Implementation	33
2.5	Simulation results	34
2.5.1	Parameters and material tensors	34
2.5.2	Microscale model	35
2.5.3	Cylinder model	37
2.5.4	True to scale bone model	44
2.6	Conclusion and outlook	49
2.7	Appendix A: Calculation of the strong form for the micro problem	50
2.8	Appendix B: Derivation of the matrix form for the FEM	52
3	Article 2: Inverse modeling of cancellous bone using artificial neural networks	55
3.1	Abstract	56
3.2	Introduction	56
3.3	Material model of the forward problem	58
3.4	Data Collection	60
3.5	Neural Network Design	62
3.6	Results	63
3.7	Conclusion	66

4	Article 3: On the effects of a surrounding medium and phase split in coupled bone simulations	67
4.1	Abstract	68
4.2	Introduction	68
4.3	Material model	70
4.3.1	Two-phase coupled model of bone	70
4.3.2	Inclusion of a surrounding medium	72
4.3.3	Differentiation of macroscale phases	73
4.4	Numerical implementation	75
4.5	Simulation results	76
4.5.1	Influence of the surrounding medium air compared to previous results	76
4.5.2	Results for the three-way split cylinder model	80
4.6	Conclusion	80

List of Figures

1.1	Schematic anatomy of a long bone, from Betts et al. (2013).	2
1.2	Detailed image of cancellous bone in the epiphysis of a human femur, from Klimešová (2019), cf. also Tandler (1919). The photographed item is a part of the anthropological collections of the Department of Biology and Environmental Studies of the Faculty of Education of Charles University (Czech Republic). For purposes of exhibition, the bone is shown in a dry state, i.e., the bone marrow and other organic material have been removed.	2
1.3	Left: Images of sagittal cuts through vertebral body of a young man (top) and an elderly woman whose bone is affected by osteoporosis (bottom) (cf. Turner Biomechanics Laboratory (2011)). Right: Schematic depiction of cancellous bone and cortical bone for a healthy bone (top) and a bone affected by osteoporosis (bottom) (cf. Ringe et al. (2019)).	3
1.4	Schematic illustration of intrinsic electromechanical coupling effects (cf. Chae et al. (2018)). From top to bottom: piezoelectricity, electrostriction, flexoelectricity. The red arrows indicate the direction of electric dipoles. The blue arrows represent mechanical stress.	4
1.5	Left: inhomogeneous example body containing inclusions and cavities. Right: computational model of the body with scale transition for the example of structure mechanics, with macroscopic strain $\bar{\epsilon}$ and macroscopic stress $\bar{\sigma}$	10
1.6	Schematic structure of a feed-forward neural network.	12
2.1	Bone phases depending on osteoporosis stage (cf. Laboratoires Servier (2019)) and corresponding RVEs.	22
2.2	Transition between macro- and microscale. State variables enter as boundary conditions of the RVE problem. Flux quantities at the macroscale are calculated by averaging the RVE quantities.	23
2.3	Program flow of the multiscale simulations.	33
2.4	Periodic RVE with cortical bone phase (gray) and bone marrow phase (transparent red) and lengths parameters.	35
2.5	Microscale simulation results of a coarse and fine mesh (left and right respectively) for all flux quantities. Top left: mechanical stress σ_{xy} [GPa], top right: mechanical stress σ_{xy} [GPa] in the xz -plane with $y = 0$, bottom left: magnitude of the electric displacement field \mathbf{D} [A s/m ²], bottom right: magnitude of the magnetic field strength \mathbf{H} [A/m].	36
2.6	Used meshes for the complete RVE (left) and only the cortical bone phase (right). a coarse hexahedron mesh, b fine hexahedron mesh, c coarse tetrahedron mesh, d fine tetrahedron mesh.	36
2.7	Effective Young's modulus E_{eff} against cortical bone volume fraction ρ_b for different RVEs.	38
2.8	Cylinder mesh and displacement boundary conditions (red: all directions restricted, orange: only the x-direction restricted, blue-gray: no directions restricted).	38
2.9	Cylinder front in the xy -plane for $z = 0$ with grounded nodes in red.	39

2.10	Amplitude of the displacement function a against the time step t	39
2.11	Magnitude of the average electric displacement field \mathbf{D} [As/m ²], plotted against the time t	40
2.12	Magnitude of the average magnetic field strength \mathbf{H} [A/m], plotted against the time t	40
2.13	Simulation results for RVE 1 (top) to 6 (bottom): stress σ_{xy} [GPa], $t = 25$	41
2.14	Simulation results for RVE 1 (top) to 6 (bottom): magnitude of the electric displacement field \mathbf{D} [As/m ²], $t = 25$	41
2.15	Simulation results for RVE 1 (top) to 6 (bottom): magnitude of the magnetic field strength \mathbf{H} [A/m], $t = 50$	42
2.16	Simulation results for RVE 1 (top) to 6 (bottom): magnitude of the electric current density \mathbf{J} [A/m ²], $t = 50$	42
2.17	Simulation results for RVE 1 for the magnetic field strength \mathbf{H} [A/m] with $\kappa_1 = 1 \cdot 10^2$ S/m (top), $\kappa_1 = 1 \cdot 10^4$ S/m (in the middle) and $\kappa_1 = 1 \cdot 10^6$ S/m (bottom), $t = 50$	43
2.18	Simulation results for RVE 1 for the electric current density \mathbf{J} [A/m ²] with $\kappa_1 = 1 \cdot 10^2$ S/m (top), $\kappa_1 = 1 \cdot 10^4$ S/m (in the middle) and $\kappa_1 = 1 \cdot 10^6$ S/m (bottom), $t = 50$	43
2.19	Anisotropic RVE with cortical bone phase (gray) and bone marrow phase (transparent red) and lengths parameters.	43
2.20	Simulation results for RVE 6 (top) and the anisotropic RVE (bottom) for the stress σ_{xy} [GPa], $t = 25$	44
2.21	Simulation results for RVE 6 (top) and the anisotropic RVE (bottom) for the magnetic field strength \mathbf{H} [A/m], $t = 50$	44
2.22	Femur bone mesh and displacement boundary conditions (red: all directions restricted, orange: only the x-direction restricted, blue-gray: no directions restricted).	44
2.23	Femur bone front with grounded nodes in red.	44
2.24	Simulation results for RVE 1 (top) to 6 (bottom): stress σ_{xy} [GPa], $t = 25$	45
2.25	Simulation results for RVE 1 (top) to 6 (bottom): magnitude of the electric displacement field \mathbf{D} [As/m ²], $t = 25$	45
2.26	Simulation results for RVE 1 (top) to 6 (bottom): magnitude of the magnetic field strength \mathbf{H} [A/m], $t = 50$	46
2.27	Simulation results for RVE 1 (top) to 6 (bottom): magnitude of the electric current density \mathbf{J} [A/m ²], $t = 50$	46
2.28	Simulation results for RVE 1 (top) to 6 (bottom): magnitude of the magnetic field strength \mathbf{H} [A/m], slice, $t = 50$	47
2.29	Simulation results for RVE 1 (top) to 6 (bottom): magnitude of the electric current density \mathbf{J} [A/m ²], slice, $t = 50$	47
2.30	Average magnetic field strength for the different RVEs at $t = 50$	48
2.31	Maximum magnetic field strength for the different RVEs at $t = 50$	48
3.1	Overview and schematic flow of the task.	56
3.2	Mesh of the cylinder, (a) along the length, (b) in the cross section. The different colors refer to the sections with the same volume fractions of cortical bone. . . .	60
3.3	Average magnetic field strength for different RVEs (cf.[Błaszczuk and Hackl (2022), Błaszczuk and Hackl (2021b)]).	62
4.1	Cross section of human bone, from Ref. Pbrks/Wikimedia (2022).	74

4.2	Schematic comparison of the structure of long human bones in the center and at its endings with corresponding cross section models (white: cortical bone, light red: spongy bone (phase mixture), dark red: bone marrow), image composed from Refs. Laboratoires Servier (2022); Klimešová (2022a,b).	74
4.3	Boundary conditions of the model. For the cylinder model nodes, red: $\mathbf{u} = \mathbf{0}$, light orange: mechanical displacement in x -direction applied, blue-gray: no directions restricted. For the outside box corner nodes, black grounding: $\mathbf{A} = \mathbf{0}$, red grounding: $\varphi = 0$	75
4.4	Amplitude of the displacement function a against the time step t	76
4.5	Simulation results for the four used meshes (only cylinder part shown): magnetic field strength $\mathbf{H}[\text{A/m}]$, at $t = 50$. From top to bottom: previous used cylinder mesh, cylinder mesh with air, finer cylinder mesh with air, cylinder mesh with air and wider boundary box.	78
4.6	Simulation results with adjusted color scale for the previous used cylinder mesh (top) and cylinder mesh with air (bottom, only cylinder part shown): magnetic field strength $\mathbf{H}[\text{A/m}]$, at $t = 50$	78
4.7	Simulation results for model two to four: magnetic field strength $\mathbf{H}[\text{A/m}]$, at $t = 50$. Slice of plane with x -normal vector in the middle of the cylinder. The white line shows the boundary of the cylinder.	79
4.8	Simulation results for model two to four: magnetic field strength $\mathbf{H}[\text{A/m}]$, at $t = 50$. Slice of plane with z -normal vector in the middle of the cylinder. The white line shows the boundary of the cylinder.	81
4.9	Simulation results: magnetic field strength $\mathbf{H}[\text{A/m}]$, at $t = 50$. Left and right cylinder base of previous model (top) and model including surrounding medium (bottom).	82
4.10	Cylinder model with surrounding medium and differentiation between the macroscale phases bone marrow, cancellous (spongy) bone and cortical bone (from the center to the cylinder boundary).	82
4.11	Simulation results for the RVEs 1 (top) to 6 (bottom) for three-way split cylinder macroscopic model: magnetic field strength $\mathbf{H}[\text{A/m}]$, at $t = 50$	83

List of Tables

2.1	Load and numerical time step increment for the different models.	34
2.2	Default material parameters.	35
2.3	Lengths parameter of the different RVEs.	37
3.1	Possible volume fraction values depending on the ID key (RVE number). . . .	60
3.2	Used activation functions and optimizers for both approaches.	63
3.3	Quality of the different networks (maximum = 4000).	64
3.4	Comparison of the network types with respect to the different classes.	64
3.5	Distances from the expected outputs.	65
3.6	Influence of the activation function to the number of correct classifications (maximum = 4000).	65
3.7	Influence of the optimizer to the number of correct classifications (maximum = 4000).	65
4.1	Default material parameters.	77
4.2	Comparison of finite element meshes used for calculating simulation results. Top left: previously used cylinder mesh (1767 nodes, 1440 elements), top right: cylinder mesh with air (5365 nodes, 4608 elements), bottom left: finer cylinder mesh with air (20165 nodes, 18432 elements), bottom right: cylinder mesh with air and wider boundary box (10019 nodes, 8736 elements).	78

1 Introduction

1.1 Motivation

Osteoporosis is the most common bone disease in the world. It is especially prevalent in the elderly and more often found in women [Reginster and Burlet (2006), Wade et al. (2014)]. In order to gain a comprehensive understanding of the disease, the anatomy of the organ bone must first be examined in detail. Figure 1.1 illustrates the general structure of long bones.

Cortical (compact) bone forms the outer shell of the bone. The diaphysis (bone shaft) contains the medullary cavity, which is filled with bone marrow, while the epiphyses (ends of the bone) are primarily composed of cancellous (spongy) bone. Cancellous bone, also referred to as trabecula, is a composite material consisting of cortical bone and bone marrow. In more precise terms, its geometry resembles a network of small and thin interconnected beams, shells and plates of cortical bone, with bone marrow situated in the interstices. Figure 1.2 illustrates the structural composition of cancellous bone, exemplified by a human femur bone.

The disease osteoporosis is characterized by a loss of cortical bone material, i.e., bone tissue deteriorates and the volume density of cortical bone is reduced. Typically, the trabecula is more strongly affected than the outer shell. While the volume fraction of cortical bone in healthy bones can reach 30%, it may be reduced to 5% in later stages of osteoporosis [Steeb (2010), Ilić et al. (2010)]. As a result, the bone becomes weaker and thinner, making it more susceptible to fractures. The reduction of bone density is evident from Figure 1.3, left. Two images are shown comparing the bone condition of a healthy young man to an elderly woman, whose bone is affected by osteoporosis. A schematic progression of the disease is illustrated in Figure 1.3, right. Notably, some complete beams of cortical bone are absent in the trabecula, resulting in the formation of a bone impression due to the reduced stiffness.

Currently, a number of different methods exist for the diagnosis of osteoporosis. While radiography is a widely available diagnostic tool, it has the limitation that osteoporosis can only be detected in the later stages of the disease [Grampp et al. (1997)]. The current "gold standard" for the diagnosis of osteoporosis is dual energy X-ray absorptiometry (DXA), which can accurately measure bone mineral density and provide information about fracture risks and the necessity of treatment [Blake and Fogelman (2007)]. Both methods have the disadvantage that patients are exposed to radiation during the procedure. For these reasons, it is desirable to develop cheaper and less invasive tools for the early detection of osteoporosis.

An alternative diagnostic method could be sonography. This approach relies on the piezoelectric properties of bone, as demonstrated in Fukada and Yasuda (1957). Ultrasonic waves entering the bone cause a small mechanical deformation, which generates an electric field.

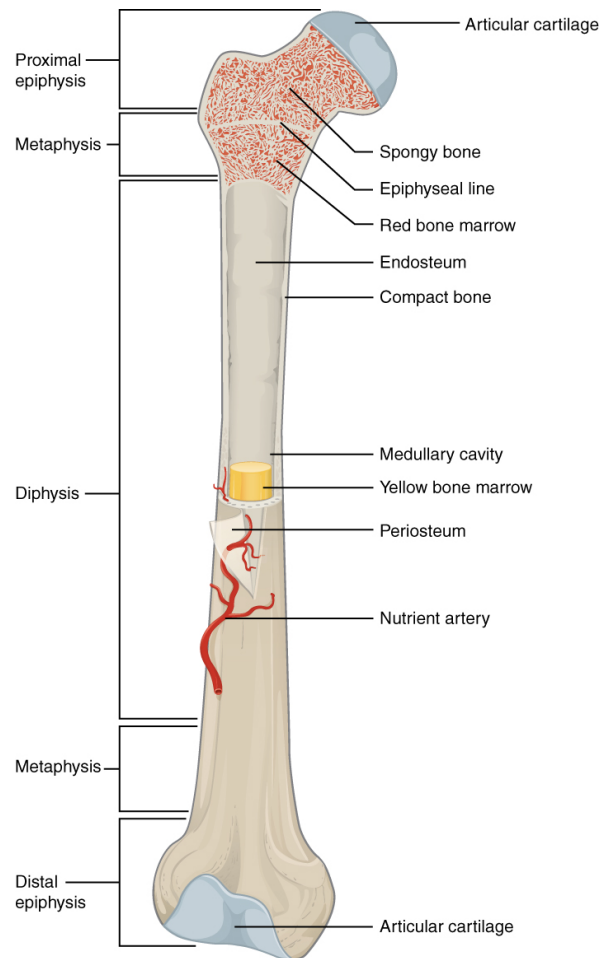


Figure 1.1: Schematic anatomy of a long bone, from Betts et al. (2013).



Figure 1.2: Detailed image of cancellous bone in the epiphysis of a human femur, from Klimešová (2019), cf. also Tandler (1919). The photographed item is a part of the anthropological collections of the Department of Biology and Environmental Studies of the Faculty of Education of Charles University (Czech Republic). For purposes of exhibition, the bone is shown in a dry state, i.e., the bone marrow and other organic material have been removed.

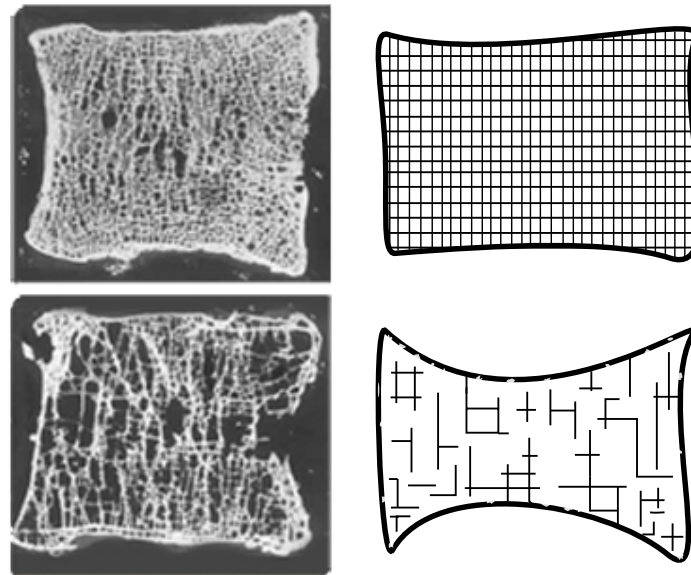


Figure 1.3: Left: Images of sagittal cuts through vertebral body of a young man (top) and an elderly woman whose bone is affected by osteoporosis (bottom) (cf. Turner Biomechanics Laboratory (2011)). Right: Schematic depiction of cancellous bone and cortical bone for a healthy bone (top) and a bone affected by osteoporosis (bottom) (cf. Ringe et al. (2019)).

As the process is time-dependent, the electric field changes with time. Consequently, a magnetic field is induced according to the coupling in Maxwell's equations (Ampère's circuital law), which relates mechanical, electric, and magnetic effects. As the composition of bone is altered by osteoporosis, the magnetic field strength may vary depending on the health condition of the bone. Thus, measuring the magnetic fields after exposing a bone to ultrasonic waves could allow to draw conclusions about its composition [Güzelsu and Saha (1981)]. Modeling and simulation are important tools to advance the development of this diagnostic method, pursuing the long-term ambition to enable the usage of sonography for the early detection of osteoporosis.

The primary objective of this thesis is the development of a multiscale and multiphase material model for cancellous bone that considers the full coupling of mechanical, electric, and magnetic effects. Subsequently, the model is employed to solve the forward and inverse problem of bone modeling in the context of sonography-based early detection of osteoporosis. The forward problem refers to the solution of the resulting partial differential equations (PDEs) to obtain the magnetic field strength, comparing different stages of osteoporosis. The inverse problem is concerned with the determination of the bone health condition from the magnetic field data.

1.2 State of the art

This chapter provides an overview of the current state of the art in various fields. It covers electromechanically coupled modeling in Chapter 1.2.1, mechanically and multiphysics modeling of bone in Chapters 1.2.2 and 1.2.3, respectively, multiscale modeling in Chapter 1.2.4 and artificial neural networks in Chapter 1.2.5.

1.2.1 Electromechanically coupled modeling

Electromechanical coupling describes all physical phenomena where a material produces an electric charge when subjected to a mechanical force, or where a material exhibits a strain response when being exposed to an electric field. The different kinds of coupling can be divided into intrinsic effects (piezoelectricity, electrostriction, flexoelectricity) and extrinsic effects (electrochemical effect, electrostatic effect) [Chae et al. (2018)]. Intrinsic effects originate from the atomic structure of the material, e.g., the molecular structure or crystal symmetry. Extrinsic effects are not directly related to the atomic structure but rather systemic (e.g., the movement of ions). In the following, the mentioned coupling phenomena are explained in detail. Figure 1.4 schematically summarizes the different intrinsic coupling effects.

Piezoelectricity is a linear coupling between the domains and is the most common kind of electromechanical coupling. The application of a force/stress to a piezoelectric material

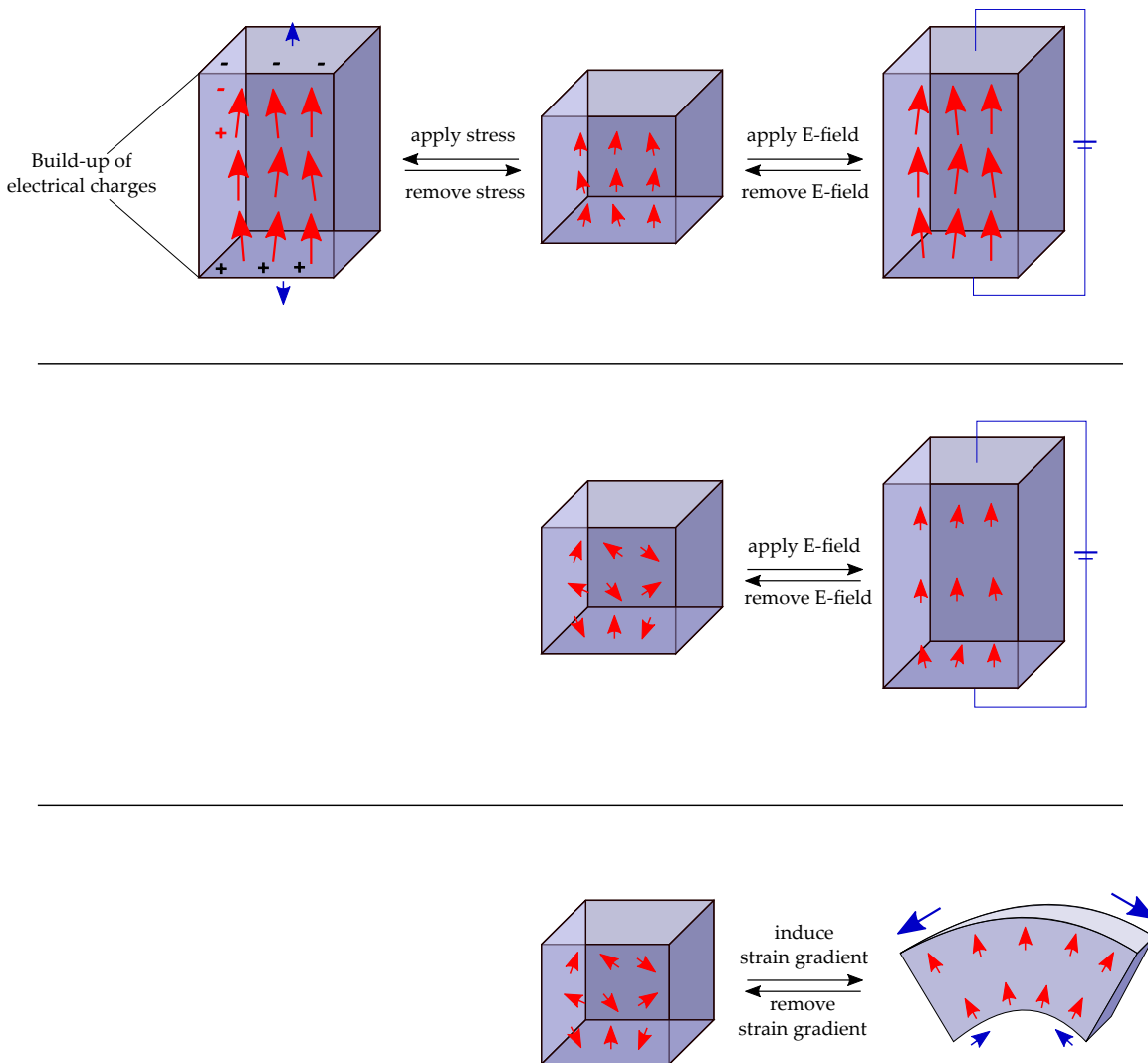


Figure 1.4: Schematic illustration of intrinsic electromechanical coupling effects (cf. Chae et al. (2018)). From top to bottom: piezoelectricity, electrostriction, flexoelectricity. The red arrows indicate the direction of electric dipoles. The blue arrows represent mechanical stress.

induces a polarization / electric field in the material (direct effect). Vice versa, an electric field applied to the material results in a strain response (converse effect). Discovered in 1880 [Curie and Curie (1880)], piezoelectricity occurs in materials that are not centrosymmetric, i.e., lack of inversion symmetry. The application of a force results in the displacement of the negative and positive centers of charge, which ultimately induces a dipole moment.

Electrostriction occurs in all dielectric materials [Chae et al. (2018)]. The material exhibits a quadratic strain response to the application of an external electric field. Consequently, the effect is limited to the portion of the strain response that is independent of the direction of the electric field applied. This implies that reversing the direction of the electric field does not reverse the direction of the deformation. The effect originates from the alignment of electric dipoles under electric loads and thus applies to all crystal symmetries (in contrast to the piezoelectric effect, which is linear and occurs only for materials possessing certain crystal symmetries).

Flexoelectricity couples polarization / electric field and strain gradient of a material. For non-uniform deformations (e.g., bending), the inversion symmetry of the material can be broken. Therefore, flexoelectricity occurs in any dielectric material. Importantly, flexoelectricity is size-dependent. As the length scale is reduced, the strain gradient increases, resulting in an enhanced magnitude of the flexoelectric effect. For this reason, the effect is especially important in very small applications, such as those at the nanoscale [Zhuang et al. (2020)].

In the following, extrinsic electromechanical coupling effects are shortly discussed. The electrochemical effect may occur during the exposure to an electric field, when a material comprises an anisotropic distribution of ions. Then, the ions move and induce a mechanical deformation. Conversely, applying a mechanical stress may induce an electric field. The electrostatic effect originates from the Coulomb forces between separated charges, which can also deform the material.

Electromechanical coupled modeling has a wide range of different applications, e.g., sensors and actuators [Busch-Vishniac (1998)], microelectromechanical systems (MEMS) [Bao (2005)] and the study of biomaterials [Pandolfi et al. (2016), Chae et al. (2018)]. Many early electric devices contained electromechanical parts until solid-state (semiconductor) electronics replaced these parts in many modern devices.

The solution of the resulting coupled problems may be approached through the application of a variety of methodologies. Analytical methods can be employed in the case of simple geometries (e.g., Chaffey and Austin (2002)), however, such approaches are usually constrained by their inherent limitations. Other examples include the application to machine drive systems [Szolc et al. (2014)] and energy harvesting [Zhou et al. (2021)], though the latter contribution compares the results obtained from analytical methods to results computed with numerical methods.

Many physical phenomena can be described by differential equations, which therefore commonly arise in modeling and engineering. The finite element method (FEM) [Zienkiewicz et al. (2005)] is a powerful tool to numerically solve differential equations for arbitrary geometries. The most common application of the method is the field of structural mechanics. However, it is also commonly used in the areas of heat flow, electromagnetics or fluid flow [Chao et al. (2002), Jin (2015)]. A key advantage of FEM is its ability to accurately solve

the underlying equations for complex geometries, which occur frequently in engineering applications. By contrast, the finite difference method (FDM) is susceptible to numerical errors in the context of irregular meshes and boundaries. Due to the steadily increasing computational power of modern computer generations, the importance of the FEM continued to grow, as complex simulations and calculations can nowadays be conducted within reasonable computational times. The method is therefore an essential part in the design of new products [Bathe (2006)]. Due to its flexibility, the FEM is also widely used for the solution of electromechanically coupled problems. Here, simulations can be carried out either in time or frequency domain [Wojcik et al. (1993), Amini et al. (2016)]. Applications include various topics from the field of biomechanics, such as modeling of skeletal muscle [Röhrle et al. (2008)] or cardiac tissues [Nardinocchi and Teresi (2013)], and energy harvesters [Martínez-Cisneros et al. (2020)].

1.2.2 Mechanical modeling of bone

Mechanical modeling of bone has a long history. While reputedly scholars living during the Renaissance speculated on the subject [Frost (1990)], one of the first accurate description of mechanical effects in bone was the postulation of Wolff's law [Wolff (1892)]. The law introduced applied mechanics to the field of biology by stating that bone in a living, healthy animal will adapt to increasing loads by remodeling itself to become stronger. This implies that training and exercise, e.g., in the form of weight lifting, increases the bone density over time, which was confirmed in experimental studies [Bassey and Ramsdale (1994)]. Conversely, the opposite is also true. A lack of loading means a lack of stimulus for remodeling, which in turn weakens the bone over time. An example for this effect is "stress shielding", which may occur in patients with a prosthesis or an implant. If the majority of the mechanical load is borne by the prosthesis, which is significantly stiffer than the surrounding bone, the bone will eventually become weakened [Mi et al. (2007)]. Therefore, preventing stress shielding is an important aspect of implant design.

Bone is a remarkable material, inspiring interest across diverse scientific disciplines, including material science. Hamed et al. (2010) lists the following properties: bone has a high strength, stiffness and fracture toughness, while at the same time being very light. A crucial mechanical property of bone is its capacity for shock absorption. Injuries and fractures occur, when the material is unable to dissipate energy (e.g., from impacts) in a timely manner. Therefore, it is essential that bone is capable of absorbing energy in order to prevent injuries from occurring as a result of everyday incidents [Evans and Thomas (1973)]. Spongy bone plays an important role in the energy absorption process. Furthermore, in Evans and Thomas (1973), spongy bone is described as a "good energy-absorbing material" due to its "foam-like structure," referencing experiments supporting this claim conducted as early as 1827. The rheology of bone marrow remains a topic of significant research interest [Sobotková et al. (1988)].

Despite the early interest in modeling of bone, it took many decades for the topic to gain importance. A main reason for this is likely that bone is a very complex organ and a lot of theory had to be developed before accurate modeling could be achieved. Moreover, modeling bone requires to combine various different mechanisms, which are usually treated in distinct scientific fields. Wolff's law itself only states what will happen, but not how, which means it does not offer a mathematical framework for the description of the observed ef-

fects. An important work advancing the field was provided by Frost and Straatsma (1964). The authors discussed bone physiology, remodeling of bone and the nature of osteoporosis. Mathematical methodology was derived by considering physical laws and patient data. Another reason for the gradual development of the field is likely to be the advancements in computer technology. In order to obtain accurate simulation results, high computation power is necessary, which has become accessible only in the last decades.

Analytical solutions are often based on Biot's theory [Biot (1956a), Biot (1956b)]. Some recent examples of this theory used in the context of bone modeling are Buchanan and Gilbert (2007), Steeb (2010) and Chen et al. (2018). As discussed in Chapter 1.1, bone consists of different phases. In these works, cortical bone is modeled as a solid, while bone marrow is assumed to be a fluid. A mathematical formulation in the context of acoustic measurements is proposed to calculate mechanical material parameters of the bone phases, which are then compared to parameters obtained from experiments.

The finite element method has been used for bone modeling starting in the early 1970s (cf., e.g., Mehta and Rajani (1970), Pugh et al. (1973)). While initial results were promising, the computational limits at that time meant the models often had to be simplified, limiting the validity of the results [Zysset et al. (2013)]. Overviews regarding state of the art and usage of the FEM in the context of bone modeling can be found in Boccaccio et al. (2011), Zysset et al. (2013) and Parashar and Sharma (2016). The latter describes how the finite element analysis is used as a helpful tool in the diagnostics and treatment of bone diseases. First, a CT scan of a patient is performed. Subsequently, a finite element model of the bone is created by incorporating information regarding material properties and loads / boundary conditions. The model can be used to perform various analyses to obtain information regarding stresses and strains or fracture toughness [Ural et al. (2011)]. The described procedure has already been used in clinical studies for the last decade and offers valuable information regarding drug treatment effects and fracture risks [Keaveny (2010)].

Further examples include obtaining mechanical properties of bone [Zysset et al. (2013), Robson Brown et al. (2014)], bone remodeling [Hambli et al. (2016)] and also fracture risk and treatment [de Bakker et al. (2017), Meng et al. (2013), Uth et al. (2017)]. In Ilić et al. (2010), the multiscale FEM is used to model bone as a complex composite material, which is also discussed in detail in Chapter 1.2.4.

1.2.3 Multiphysics modeling of bone

In the field of bone modeling, mechanical effects are often the sole consideration. However, the underlying mechanisms for growth and remodeling involve physical, chemical, and mechanical coupled interactions [Giorgio et al. (2019)]. This makes the problems very complex and accurate modeling challenging. Some examples are given in the following. In Garcia-Aznar et al. (2005), a model coupling the mechanical and biological effects for bone remodeling was developed. A basic multicellular unit (BMU) was introduced, which enabled the modeling of microdamage growth and repair. A similar approach can be found in Scheiner et al. (2013). The authors directly coupled systems biology with multiscale mechanics. The conducted simulations of bone remodeling aligned with the experimentally observed loss of bone density during aging.

Following the discovery of the piezoelectric effect in bone [Fukada and Yasuda (1957)], a number of subsequent studies were conducted which included the investigation of electric effects in the modelling process. A review of electromechanical properties of bone tissue and bone piezoelectricity can be found in the works of Güzelsu and Demiray (1979) and Mohammadkhah et al. (2019). Flexoelectricity is the effect of electrical polarization induced by a strain gradient (cf. Chapter 1.2.1). In Witt et al. (2022), both piezoelectricity and flexoelectricity are considered for the remodeling of bone and the recovery of cracks. The different bone cell types that are mainly involved in the remodeling process are all accounted for, so that the resulting model includes chemo-electro-mechanical coupling.

In the field of multiphysics modeling of bone, only few studies address the inclusion of magnetic effects. A study regarding the electro-mechanical wave propagation in long bones was conducted by Güzelsu and Saha (1981). The authors obtained analytical solutions for the simple case of a hollow cylinder model and compared their results with *in vitro* experimental values. Noteworthy, the authors considered magnetic effects and highlighted that the magnetic field created from a stress wave exists beyond the bone itself. In Spadaro (1997), the author discusses the interactions between mechanical and electromagnetic effects in the context of bone remodeling.

1.2.4 Multiscale modeling

Using multiple scales for the modeling of a material is a useful approach for materials with important properties on different scales in time and/or in space. Here, a single scale is insufficient to capture all important effects to accurately model the material. While the usage of multiple time scales is common when modeling, e.g., chemical processes, multiple scales in space are widespread to model materials with a very complex, heterogenous microstructure. This allows to capture effects on a small scale without the need for a very fine macroscopic resolution.

Analytical methods. Analytical efforts calculating effective material parameters, i.e., establishing a macroscopic constitutive model based on the microscopic material composition, date back to the works of Voigt [Voigt (1889)] and Reuss [Reuß (1929)], who were concerned with obtaining effective stiffness tensors for micro-heterogenous media, such as isotropic polycrystals. Later it was shown that the obtained results only reflect the upper and lower bounds of the effective parameters [Hashin and Shtrikman (1963)]. The difference between these bounds may be very noticeable [Schröder and Hackl (2013)], as not only the volume percentage of the different microscopic phases may influence the results but also their geometric arrangement. Further works emerged, which improved the bounds or the overall estimates, using variational principles [Hashin and Shtrikman (1963)] or perturbation methods [Willis (1981)]. While analytical methods are usually easy to implement and possess a fast computation speed, they are limited in their accuracy and can often only be applied in the case of simple microstructures. Therefore, different numerical methods emerged.

Phase field modeling. The phase field method is a very common choice in multiscale modeling to describe the evolution of the microstructure. The underlying equations were originally introduced to model demixing of phases and solidification dynamics of crystals [Cahn and Hilliard (1958), Cahn and Allen (1977)]. On this basis, the first phase field

models emerged a few years later (e.g., in Langer (1986)). Since that time, the method has continued to spread, and it is now used in a wide range of applications. Examples from the field of microstructure modeling are damage and fracture mechanics [Wu et al. (2020)], hydrogen embrittlement [Kristensen et al. (2020)] and many more. Reviews about the method and its applications can be found, e.g., in Chen (2002) and Boettinger et al. (2002).

The key idea of the method is to introduce the (local) phase field variable φ , also called order parameter, to differentiate between two states (e.g., undamaged and damaged material in fracture mechanics), which may correspond to the values $\varphi = 0$ and $\varphi = 1$, respectively. Importantly, intermediate values are also possible, creating continuous transitions between the phases, which makes the model easy to use. The interfaces between the phases become diffuse. Thus, they do not have to be tracked explicitly, making the model also efficient regarding computation times. A distinction can be made between conservative and non-conservative models. Conservative models are relaxation-like problems tracking the spatial rearrangement of the phases over time, e.g., phase separation. Here, the total volume percentages of the phases are given at the start and do not change afterwards. By contrast, non-conservative models are diffusion-like problems, where the total amounts of the phases may change during the evolution, as, e.g., in damage modeling. In both cases, the choice of the underlying energy functional determines the behavior of the model, which makes the method very flexible.

Some exemplary applications of the method combining the usage of the FEM in the field of microscale evolution are ferroelectrics [Schrade et al. (2007)], damage and fracture [Miehe et al. (2010), Kuhn and Müller (2010)], shape memory alloys and plasticity [Paranjape et al. (2016)] and chemomechanics [Svendsen et al. (2018)].

Fast Fourier transform (FFT) methods. Another numerical method is the Fast Fourier transform, an algorithm to efficiently calculate the Fourier integral transform. The method is commonly used, e.g., in signal processing to transform a signal from time domain to frequency domain, but can also be applied to multiscale modeling [Moulinec and Suquet (1995)] and homogenization [Schneider (2021)]. After having been combined with FEM for the first time by Spahn et al. in 2014 [Spahn et al. (2014)], FE-FFT methods gained in popularity as a numerical method for multiscale simulations. A review of the method and its state of the art can be found in Gierden et al. (2022). Example applications are modeling the evolution of the microstructure [Kochmann et al. (2016)], damage modeling [Fang et al. (2019)], fracture and fatigue [Lucarini and Segurado (2019), Chen et al. (2019)] and simulations of polycrystals [Prakash and Lebensohn (2009)].

The main idea of FFT-based multiscale approaches is to reformulate the microscopic boundary value problem by introducing the stiffness tensor of a homogenous reference material and a "polarization" stress, which is the stress difference between the reference material and its microscopic inclusions. The resulting PDE problem can be solved very fast and efficiently by transforming it into Fourier space, obtaining a fixed-point scheme. One of the main advantages of this method is its low computational time. However, in order to apply the method efficiently, the microscopic grid must be constructed in a regular voxel-based structure. Consequently, the method is only applicable to periodic problems and regular grids.

Finite element square method (FE²). The finite element square method extends the concept of the standard FEM to multiple scales and is used in this thesis. Basic works include, e.g., Willis (1981), Suquet (1987) and Castaneda and Suquet (1997). An introduction to the method can be found, e.g., in Schröder (2000), Feyel (2003) and Schröder and Hackl (2013). The method can be applied to a wide range of topics, for example, the modeling of fibre/matrix composite materials [Feyel (1999)], polycrystalline materials [Miehe et al. (1999)], piezoelectric composite materials [Schröder and Keip (2012)], thermomechanical coupled materials [Sengupta et al. (2012)] and multiscale topology optimization [Sivapuram et al. (2016)]. Examples of the method used in the context of bone modeling are Ilić et al. (2010) and Klinge et al. (2013).

The key idea of the method is that, instead of using a macroscopic constitutive model, a microscale simulation is performed, calculating the necessary flux quantities, which then are returned to the macroscopic scale. For this purpose, usually a representative volume element (RVE) is created, which is a (periodic) microscopic unit cell resolving the heterogeneous structure of the simulated medium. Alternatively, a statistically similar representative volume element (SSRVE) can be used [Balzani et al. (2014)].

To consider micro-heterogeneities, the model of the microscopic scale needs to be more detailed in some way. It follows that by sending information back to the macroscopic scale, some information is lost. The Hill-Mandel condition [Hill (1963), Hill (1972)] states that the virtual work during scale transition needs to stay constant, a concept which was introduced originally to solid mechanics but can also be generalized for electric and magnetic modeling [Schröder et al. (2016), Labusch et al. (2019)]. In practice, most macroscopic quantities can be obtained by calculating the volume average of the corresponding microscopic quantity in the microscopic domain. For example, for the microscopic quantity f , the volume average is defined as

$$\bar{f}(\mathbf{x}) = \frac{1}{\Omega} \int_{\Omega} f(\mathbf{y}) dV. \quad (1.1)$$

Here, Ω is the total volume of the microscopic domain, the coordinates \mathbf{x} and \mathbf{y} refer to the macroscopic and microscopic coordinate system and the use of the bar symbol indicates the affiliation of a quantity to the macroscopic scale. The process is illustrated in Figure 1.5 for the example of purely mechanical modeling with small deformations.

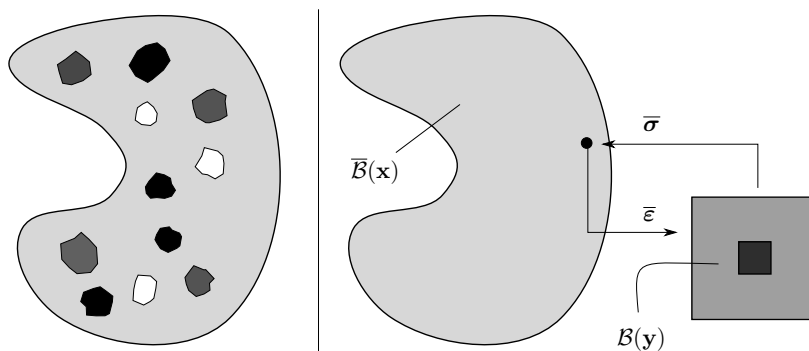


Figure 1.5: Left: inhomogeneous example body containing inclusions and cavities. Right: computational model of the body with scale transition for the example of structure mechanics, with macroscopic strain $\bar{\epsilon}$ and macroscopic stress $\bar{\sigma}$.

The scale transition is straightforward for static problems. By contrast, dynamic problems are usually modeled quasistatically when applying the FE². Recent work also included

inertia effects in the context of finite-strain applications [Tamsen and Balzani (2021)] to account for time-dependent effects. However, an extension to electromechanical problems may be a topic for future research.

It is well known that the choice of the unit cell / RVE can influence the results of the calculation. In Schröder (2000), it was shown that the usage of periodic boundary conditions in the microscopic model ensures that the obtained results are (nearly) independent from the relative position of the inclusion used and should therefore be applied when using FE².

1.2.5 Artificial neural networks

Artificial neural networks (ANNs, often simply called neural networks) are computing systems inspired by animal brains. Originally introduced in 1943 [McCulloch and Pitts (1943)], important milestones were the perceptron model [Rosenblatt (1957)] and networks with many layers [Ivakhnenko and Lapa (1965)]. The advent of high-performance computing has led to a surge in the popularity of neural networks, particularly over the past decade.

An important property of artificial neural networks is their ability to model non-linear problems. Therefore, they are used for a wide range of applications, an overview of which can be found in Abiodun et al. (2018). The fields of interest for the use of ANNs are, e.g., engineering and science [Samarasinghe (2016)], medicine [Amato et al. (2013), Shahid et al. (2019), Jumper et al. (2021)], finance [Bahrammirzaee (2010)] and strategy games [Silver et al. (2016), Silver et al. (2018)].

Similar to biological neurons, an artificial neural network consists of a group of neurons, which are nodes that are organized in layers and are interconnected. Feed-forward neural networks restrict the possible connections between the neurons to one direction, i.e., the output of a neuron depends only on inputs from the previous layer. Recurrent networks also allow connections to neurons of the same or previous layers. In both cases, the first layer receives the input data, while the last layer calculates the final result. In-between layers are called hidden layers. Figure 1.6 illustrates the structure of a feed-forward artificial neural network.

In order to obtain a result, the ANN has to calculate the output $o(x)$ of each neuron, which is carried out sequentially for each layer:

$$o(x) = a \left(\sum_{i=1}^n w_i x_i \right). \quad (1.2)$$

Here, x_i is the input data (originating strictly from the previous layer in the case of a feed-forward network), w_i are the weights and n is the number of total inputs connected to the neuron. The activation function a is applied after computing the sum, which enables, e.g., to represent non-linearities or to force an output within a determined interval.

The "learning" phase of the network is realized by inserting large amounts of training data into the network and checking, if the network produces the expected (known) output. During this phase, the network adapts to better match the output. This can be done in different ways, e.g., by creating or deleting neurons, by creating or deleting connections and by modifying

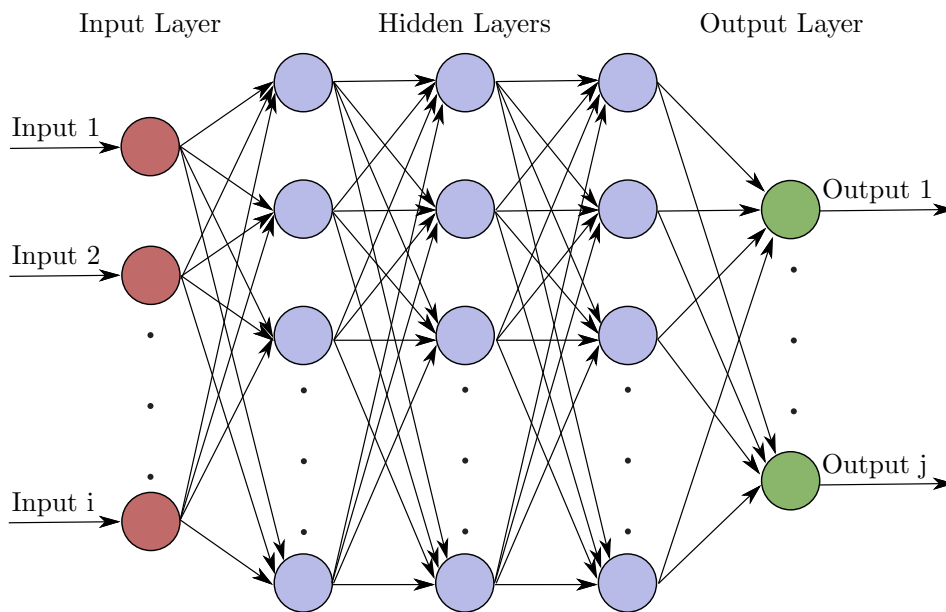


Figure 1.6: Schematic structure of a feed-forward neural network.

the activation functions. In practice, the easiest and most common way of network adaption is the change of weights in each single neuron. To evaluate the quality of the network, an error function is used to quantify the difference between computed and expected output and the network changes the neuron weights according to a learning rule. This process is repeated until the network produces similar output to the expected ones. Test data is used in between to make sure that the network does not simply "memorize" the training data. During calculations using the test data, the network is not modified. Once the network is trained, validation data may be used to proof that the network is able to correctly predict results based on its training for data it has never seen before.

The main challenges for constructing ANNs are choosing hyperparameters (e.g., the number of neurons per layer, the number of hidden layers, the activation function, the learning rate etc.) that work well. Possible problems during the training phase are underfitting (i.e., the difference between computed and expected output is too high) and overfitting (i.e., the network calculates good results for the training data but is not able to generalize regarding to the test data). ANNs are used in this thesis for the solution of the inverse problem.

1.3 Outline of the dissertation

The present cumulative dissertation is organized as follows. Chapter 2 represents one of the author's (and his coauthor's) published works, which is concerned with the development of a novel, fully coupled multiscale model of cancellous bone considering mechanical, electric, and magnetic effects. For this purpose, the finite element square method and a two-phase model on the microscale are employed. The goal of this model is to simulate bones affected by different stages of osteoporosis. Solving the resulting PDEs (forward problem) reveals that a small mechanical impact creates significantly different magnetic field responses depending on the health condition of the bone.

Chapter 3 covers the inverse problem. The objective is to recover the distribution of cortical bone mass density from the magnetic field calculated by the FE^2 simulations and thus, draw conclusions about the bone health. Artificial Neural Networks are trained to solve this task with high accuracies.

Finally, in Chapter 4, significant extensions of the base model introduced in Chapter 2 are addressed. The focus here is on the division of the macroscale into different parts. This approach permits the modeling of a surrounding medium and also allows for the application of improved boundary conditions. Additionally, the macroscopic model is split not only between the bone domain and the surroundings, but also within the bone domain to describe different bone structures in a more realistic and physiological way.

A more detailed summary of each chapter, including a short conclusion and a respective outlook, is provided in the following.

A comprehensive overview of the topic, the discussion of the state of the art and the conclusion of the entire thesis is presented in Chapter 1. Chapter 2 features the multiscale material model for cancellous bone. The microscale consists of two phases, cortical bone and bone marrow. Cortical bone is modeled as a piezoelectric, insulating solid. Bone marrow is described as a viscoelastic and conducting solid. The novelty of the model is the combination of mechanical, electric, and magnetic effects, while considering full coupling originating from both, the material model and the Maxwell equations. The reason for this model choice is given together with a short introduction on the structure of bones. Furthermore, the basic concept of FE^2 is presented. The required equations for the solution of the microscale problem are derived from energy methods in mechanics to obtain a thermodynamically consistent model. Starting with a thermodynamic energy functional, the weak and strong form of the problem are calculated. The macroscale model is shortly introduced. The application of FE^2 to the introduced model, the transition between the scales and the implementation are discussed.

Results are presented for different cases. Starting with the microscale, mesh independence and quadratic convergence behavior are confirmed for a simple cubic RVE. To model different stages of osteoporosis, six different RVEs with different volume percentages of cortical bone are created. The calculation of the effective Young's modulus shows a significant reduction for models with low volume percentage of cortical bone. Multiscale calculations are performed for a cylinder model and a model of a human femur bone using the discussed way of applying FE^2 . In both cases, all quantities are reduced, when RVEs with low volume percentage of cortical bone are used. Most importantly, this especially applies for the magnetic field strength, which is the measured quantity in sonography-based early detection of osteoporosis. The average and the maximum magnetic field strengths show a similar trend. Notably, the difference between the obtained magnetic field strength is higher the lower the volume percentage of cortical bone is for the RVEs used.

While the results shown are already promising for the application of sonography in diagnostics, certain aspects limit the applicability of the model and, therefore, have to be addressed. The RVEs used for the microscale calculations are coarse and contain sharp edges, which may lead to numerical inaccuracies. Furthermore, the model does not include a boundary box. This means, the influence of a surrounding medium like air or water is not considered and no proper decay of the electromagnetic fields is achieved. An extension of the model concerning this point is discussed in Chapter 4. Lastly, the model only predicts the mag-

netic field strength from given input data. The inverse problem of finding the corresponding composition of bone (i.e., the distribution of cortical bone phase at the macroscale) from the magnetic field strength data is of great importance for diagnostics.

Chapter 3 is concerned with solving the inverse problem. For this purpose, the material model discussed in the previous chapter is used to generate a large sample of magnetic field data. This data is then utilized as the input for ANNs, which are trained to output the correct distribution of bone material. After a short reintroduction of the material model used, the data collection and neural network design is explained. For the data generation, the cylinder model is split into eight parts along its length and the RVEs used in each part are randomly chosen from six different RVEs, the same set which was also investigated in the previous chapter. Haar functions are used to obtain more realistic volume fraction distributions of cortical bone, dismissing distributions where large jumps between neighboring cylinder parts occur.

Two approaches for the design of the ANNs are investigated. The aim of the regression approach is to approximate the volume fractions of cortical bone in the different parts of the cylinder. For the classification approach, one network for each cylindrical part is employed to output the ID of the RVE used. This is possible as the number of different RVEs is finite. As discussed before, the differences between the magnetic field strength is very low if the two RVEs with the highest volume fraction of cortical bone are used (RVE 5 and 6). To differentiate between these classes can be troublesome for ANNs. Therefore, additional ANNs are created that consider these two RVEs both as a single class (healthy bone). Validation data is used together with the pocket algorithm to achieve a good performance. Overfitting is prevented by the usage of the early stopping method.

All ANN designs show very good results by reaching accuracies of more than 96%. The classification approach is slightly better compared to the single network regression approach. Merging the fifth and sixth classes further improves the performance, as the ANNs built for six different classes show difficulties in differentiating the last two classes. Both the choice of the activation function and the optimizer used are shown to significantly impact the results of the networks. Finally, the low computational cost of classification using the obtained neural network is confirmed, which qualifies the method as a standard diagnosis tool.

The obtained results are satisfactory, but there are some aspects that require further attention to enhance the applicability of the model with the long-term objective of making it a useful tool in the early detection of osteoporosis. A more detailed model of the bone could be used to improve the simulation results on which the performance of the ANNs is based. So far, only simulations are used to obtain the required input data for the ANNs. Experimental research is necessary to validate the simulation results. Furthermore, in the model it is assumed that the magnetic field strength is known precisely at every node of finite element mesh. The resolution of the data for real-world setups depends on the measurement technology used and may be worse. For this reason, future research could investigate, if ANNs are still able to accurately predict the health of the bone when given less or less accurate input, respectively. Lastly, finer separations of both the bone volume fractions and parts along the length of the bone could be investigated.

Chapter 4 deals with extensions of the basic bone model presented in Chapter 2. Three different parts are addressed, all related to subdividing the macroscopic model. A boundary box around the cylinder model is constructed to account for effects of a surrounding medium

(this could, e.g., be air or water) and allow the decay of the electromagnetic fields. This way, the boundary conditions chosen for the magnetic vector potential are more suitable. Lastly, the differentiation between the phases was not only implemented between the cylinder and the surrounding medium, but also within the cylinder. With this approach, it is possible to describe the macroscale in a more physiological way and assign cortical bone, bone marrow and the phase mixture (spongy/cancellous bone) to different parts of the cylinder model.

The previously established material model is shortly reintroduced. The different extensions of the model are presented in detail, especially considering the physiological properties of real bones. The numerical implementation is discussed, showing the different meshes and boundary conditions used. Noticeably, two different types of models are shown. The first model is the cylinder model including the boundary box to investigate the influence of a surrounding medium and to compare the results to previously obtained ones. The second model is the three-way split cylinder model, where the cylinder is divided starting from the center to its boundary into three parts of bone, i.e., bone marrow, spongy bone (phase mixture where again the FE^2 is applied) and cortical bone. The three-way split cylinder model also includes the boundary box.

The results for the first model show a slight increase in magnetic field strength compared to previous results. By contrast, the magnetic field strength at the left end of the cylinder is significantly reduced, resulting in a symmetric field distribution due to the use of improved boundary conditions. The results for the three-way split cylinder are conform with previously obtained results.

The chapter dealt with important extensions of the basic bone model, improving the applicability of the model. Especially the improvement of the boundary conditions yielded the desired effects as shown in the results. Despite that, further improvements are possible. Nédélec function spaces for the magnetic vector potential could be used to improve the numerical performance of the model. While it is straightforward to construct a boundary box for simple geometries like the cylinder model used, it can be very complicated for more complex geometries, for example real human femur bones. The discontinuous Galerkin method could be used without introducing additional computational costs. The complex part of the geometry could be inserted into a larger boundary domain without the necessity of matching the mesh resolution of the different parts.

1.4 Conclusion and outlook

In this thesis, multiscale modeling of cancellous bone has been investigated. A novel multiscale and multiphase material model was developed. FE^2 simulations were evaluated, demonstrating that the magnetic field strength is significantly influenced by the volume percentage of cortical bone of the RVEs used. The magnetic field strength is drastically reduced for RVEs with low volume percentages of cortical bone (representing later stages of osteoporosis) in comparison to RVEs with high volume percentages of cortical bone (representing a healthy bone). The inverse problem can be solved with high accuracy by employing ANNs. The results demonstrate that the models investigated are functioning as intended. Therefore, this work constitutes an important part of fundamental research to advance the development of sonography for the early-detection of osteoporosis.

While the results obtained are promising, there are several unanswered questions and aspects that could be addressed in future research. The most significant issues are summarized below.

For the multiscale model of cancellous bone, important aspects are given in the following:

- The presented work is purely theoretical in nature. In order to ascertain the realism of the data obtained from the model, it must be compared with data obtained from experiments. The outcome may be either a confirmation of the simulations and the model, if the data is similar. Otherwise, the experimental data may show significant differences, which would draw attention to possibly underrepresented aspects in the simulations that have to be addressed in future research. This includes the possibility of obtaining accurate material parameters from experiments, which could then be used for the simulations.
- The current model uses standard (nodal) finite elements. It is well known, that nodal elements may cause numerical issues and inaccuracies in the context of electromagnetic problems. Spurious solutions may arise due to the inability of the shape functions to resolve discontinuities in the solution fields, which may occur, for instance, at the interface between different materials (with different material parameters). An alternative approach is the Nédélec $H(\text{curl}; \Omega)$ -conforming finite element (introduced in Nédélec (1980)), which possesses its degrees of freedom at the edges of the element. However, implementation would require additional effort. In Mur (1998) the author claims that the problems cannot be resolved by the choice of the element type but instead by a proper finite element formulation. Further investigation is required to review this for the presented model, in particular with regard to the behavior of the model at the scale transition.
- The RVEs used in the simulations are very coarse and simple in their design. Different RVEs could be investigated, which may contain, e.g., a finer resolution, a different size or additional geometric details. Furthermore, anisotropic RVEs could be employed. This way, the influence of the RVE used on the macroscale results could be investigated further. This also includes random rotations of the microstructure: different orientations for each integration point could be investigated.
- An alternative multiscale method could be used in place of FE^2 . A FE-FFT approach may be suitable to utilize the periodic structure of the RVEs. This could speed up the computations significantly and allow multiscale simulations of RVEs representing real bone structures.
- A dimensionless formulation of the PDE system could be introduced to generalize and simplify the problem. This improvement could enhance the numerical quality and stability of the simulations.

Some further possible expansions of the model are:

- The Discontinuous Galerkin method may be introduced to enable the easy usage of a boundary box for complex macroscopic geometries (e.g., the model of a human femur bone, which was previously used without a boundary box) [Cockburn (2003)]. Here, the main advantage would be that a matching mesh resolution of different model parts

(e.g., femur and boundary box) is not necessarily required.

- The inclusion of flexoelectricity in the presented model could be reasonable, as the effect has been shown to be prevalent in bone, particularly at crack tips. For this reason, the effect may play an important role in repair and remodeling of bone [Vasquez-Sancho et al. (2018), Witt et al. (2022)]. As flexoelectric materials may have different possible applications, the computational modeling, though not necessarily related to bone, has been investigated extensively [Zhuang et al. (2020), Zhuang et al. (2023)], making the implementation accessible.
- Wave propagation in bone could be investigated in more detail. By deriving the equations in the complex domain, the expansion of waves and the (eigen-)frequencies could be obtained (cf. Ilić et al. (2010)).
- Other applications of the same or a slightly modified model may be possible, for example the extension to soft tissues, by rewriting the equations for the case of large deformations.

Finally, concerning the inverse modeling of cancellous bone, the following points might be addressed in future research:

- The modeling is purely theoretical. Therefore, the obtained data from the simulations has to be compared to experimental data to examine the quality of the results.
- In the model used it is assumed that the magnetic field strength is known precisely at every node of the finite element mesh. In practice, this is not the case. Instead, the resolution of the obtained magnetic field depends on the measurement techniques applied. It is therefore likely that in real world applications the input data is less accurate. It could be investigated, if neural networks are still able to make accurate predictions when given less or less accurate input to account for the difference between simulations and real world.

2 Article 1: Multiscale modeling of cancellous bone considering full coupling of mechanical, electric and magnetic effects

This article was published as:

Blaszczyk M. and Hackl K. (2022). Multiscale modeling of cancellous bone considering full coupling of mechanical, electric and magnetic effects. *Biomechanics and Modeling in Mechanobiology* 21(1), 163-187.

2.1 Abstract

Modeling of cancellous bone has important applications in the detection and treatment of fatigue fractures and diseases like osteoporosis. In this paper, we present a fully coupled multiscale approach considering mechanical, electric and magnetic effects by using the multiscale finite element method and a two-phase material model on the microscale. We show numerical results for both scales, including calculations for a femur bone, comparing a healthy bone to ones affected by different stages of osteoporosis. Here, the magnetic field strength resulting from a small mechanical impact decreases drastically for later stages of the disease, confirming experimental research.

2.2 Introduction

In the present contribution, we develop a multiscale model for cancellous bone taking mechanical, electric and magnetic effects into account. An important application of this model is the early detection of osteoporosis. This bone disease reduces the mass density of the bone, making it thinner and weaker, increasing the likelihood of fractures. Sonography is used as a cheap, fast and non-invasive early detection technique for osteoporosis [Kaufman et al. (2008)]. Material modeling and numerical simulations are helpful tools in order to understand and evaluate experimental measurements and enable medical diagnostics based on this method.

Bone is a composite material with impressive properties, drawing the interest of researchers of many different fields. As a material, it is very strong and stiff and has a high fracture toughness, while also maintaining a light weight [Hamed et al. (2010)]. Thus in recent decades, a lot of different approaches to investigate and simulate the material behavior of bone have appeared. Many analytical solutions are based on Biot's famous theory [Biot (1956a), Biot (1956b)]. Examples include Buchanan and Gilbert (2007), Chen et al. (2018) and Steeb (2010). Here, cortical bone is modeled as a solid, while bone marrow is assumed to be a fluid. The acoustic properties of bone material are then used to obtain mechanical material parameters of bone and the parameters of Biot's model. Additionally, the results are compared with the findings of experiments.

In contrast to the analytical solutions, many numerical approaches exist in the scope of bone modeling as well. The finite difference method was used in Kaufman et al. (2008) to obtain numerical results of ultrasound propagation in bone. Applications of the finite element method (FEM) on the topic of bone modeling include the simulation of mechanical properties of bone [Gardner et al. (2000), Miller et al. (2002)] and the simulation of osteogenic effects [Wang et al. (2017)]. In Christen et al. (2010) patient-specific FEM simulations are proposed in order to estimate the likelihood of osteoporotic fractures.

Since the bone microstructure is very complex and heterogenous, material modeling should take place on different scales. Currently used single scale models are criticized in Christen et al. (2010) as oversimplified and multiscale approaches proposed instead. In Hamed et al. (2010), the mechanical properties of bone are modeled on five different length scales from the nanoscale to the macroscale. Multiscale approaches can also be combined with numerical methods. The finite element square method (FE²) extends the standard FEM approach

by applying the multiscale concept and solving the differential equation systems on two scales via the FEM. An overview of the method can be found in Schröder (2000), Schröder and Hackl (2013). Basic works on this method include for example Willis (1981), Suquet (1987), Castaneda and Suquet (1997) and applications to different materials can be found for example in Ilić and Hackl (2004), Miehe et al. (2002). An application of the FE² within the scope of bone modeling can be found in Ural and Mischinski (2013), Podshivalov et al. (2011), Pahr and Zysset (2008), proposing different models to capture the microstructure of bone, allowing to investigate mechanical effects. In Ilić et al. (2010) and Klinge et al. (2013), macroscopic material parameters were recovered by simulations on the microscale. The results obtained were subsequently used for macroscale simulations of wave propagation.

So far, all presented contributions focus only on the mechanical effects of bone. However, cortical bone possesses the properties of a piezoelectric solid. After the discovery of this effect Fukada and Yasuda (1957), Shamos et al. (1963), research considering these coupled physical effects has started. A review on computer modeling of bone piezoelectricity can be found in Mohammadkhah et al. (2019). There, applications are discussed as well. Since electric and magnetic effects are coupled physically via the Maxwell equations, it may be necessary to include magnetic effects as well. In Güzelsu and Saha (1981), bone was modeled as a hollow cylinder and analytical solutions of the coupled equations of all three effects were studied. The results were then compared to *in vitro* experimental measurements.

In this work, we present a fully coupled multiscale approach for modeling cancellous bone considering mechanical, electric and magnetic effects and using two scales, the macro- and microscale. At the microscale, we assume a heterogeneous material consisting of two phases, cortical bone and bone marrow. Cortical bone is modeled as piezoelectric, insulating solid, bone marrow as viscoelastic, conducting solid. Electric and magnetic effects are coupled via the Maxwell equations. Based on energy methods in mechanics, we establish a thermodynamically consistent material model and derive the weak and strong form of the corresponding boundary value problem. We apply the FEM to solve the problem numerically. For multiscale analysis, we resort to the FE² method. To apply this method, we constructed a periodic representative volume element (RVE) and discuss the transition between scales.

The article is structured as follows: in Section 2.3 we discuss the material structure of cancellous bone and the FE² method. Then, we introduce the microscopic material model and derive the weak and strong form of the corresponding variational problem. Additionally, we cover the macroscale boundary value problem. In Section 2.4 we present the FEM implementation of the model and show details regarding scale transition and programming. In Section 2.5 we present numerical results, starting with microscale calculations, on to multiscale simulations for a cylindrical body and finally a true to scale model of a human femur bone. To close this article, we draw a short conclusion and give an outlook to future research envisioned in Section 2.6.

2.3 Material model

2.3.1 Structure and properties of cancellous bone

Our work focuses on the description of the internal structure of cancellous (spongy) bone, which consists of small beams or shells of interconnected cortical bone and interstitial bone marrow. Cortical bone is mainly composed of elastic collagen fibers, which act as charge carriers. When applying a shear stress, these collagen fibers slip past each other, thus producing a piezoelectric effect. This was first measured in Fukada and Yasuda (1957) and later validated in Shamos et al. (1963). This means that, whenever a mechanical strain is present in the bone, an electric field is generated due to the piezoelectric effect. A time-dependent fluctuation of the electric field then creates a magnetic field due to Ampère's circuital law, coupling mechanical, electric and magnetic effects all together.

An important application of bone modeling is the early detection of osteoporosis, a bone disease, which manifests itself in the reduction of the cortical bone phase, thus reducing the strength of the bone and increasing the likelihood of fractures. Compared to a healthy bone, the volume fraction of cortical bone for an affected bone can be reduced from 30% to 5% [Steeb (2010), Ilić et al. (2010)]. Figure 2.1 shows a comparison depending on the osteoporosis stage and illustrates the heterogeneity of the material. During the course of osteoporosis, the cortical bone (represented brighter) reduces and is replaced by bone marrow (represented in dark). Thus, we will employ different RVEs for the simulations. Here, the cortical bone phase is represented in gray, while the bone marrow phase is drawn in transparent red color.

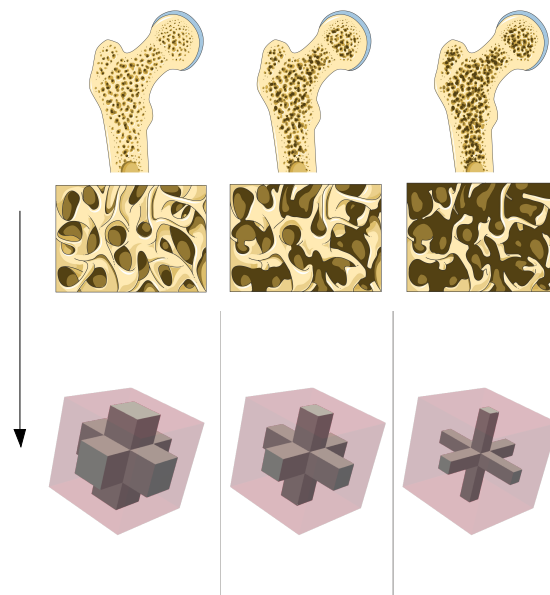


Figure 2.1: Bone phases depending on osteoporosis stage (cf. Laboratoires Servier (2019)) and corresponding RVEs.

Early detection of osteoporosis can be done via sonography: ultrasonic waves enter the bone and due to the described effects create a magnetic field, which can be measured [Güzelsu and Saha (1981)] and - depending on the results - conclusions on the health status of the

investigated bone can be drawn. In this contribution, we introduce a material model including all the described effects. It is important to note, that there are two different forms of coupling: while the piezoelectric coupling is captured via a suitable material model, the Maxwell coupling is of physical (electrodynamical) nature.

2.3.2 Concept of the FE^2 method

To include micro-heterogeneities directly, an extremely fine resolution of the problem would be necessary, resulting in a very high computation cost for the simulations. Alternatively, the FE^2 method is a homogenization technique, which captures the structure of micro-heterogeneities by introducing a second - smaller - scale to the problem. If the material is statistically regular on the smaller scale, it can be modeled by a corresponding RVE [Schröder (2000), Schröder and Hackl (2013)]. In this paper, we denote the larger scale as the macroscale and the smaller scale as the microscale. To obtain accurate results, the quotient of the characteristic lengths between micro- and macroscale should tend to zero, so the RVE has to be much smaller than the simulated macroscopic body. Figure 2.2 illustrates this procedure: instead of using a material model on the macroscale, the state variables are linked to the microscale, where the RVE problem is solved. The microscale calculations yield average flux quantities and consistent tangent matrices, which then can be used for the solution of the macroscale problem, replacing a macroscopic material model.

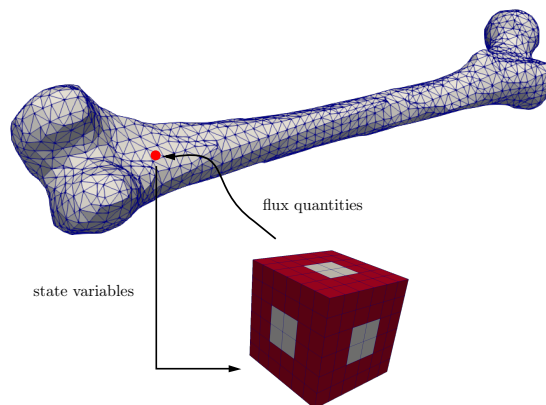


Figure 2.2: Transition between macro- and microscale. State variables enter as boundary conditions of the RVE problem. Flux quantities at the macroscale are calculated by averaging the RVE quantities.

We denote spatial coordinates on the macroscale by \mathbf{x} and on the microscale by \mathbf{y} . Quantities denoted as $\overline{(\cdot)}$ are affiliated to the macroscale. The transition between the scales regarding energy conservation and numerical treatment is discussed in Section 2.4.2.

2.3.3 Variational formulation of the microscale problem

The domain $\Omega := \Omega_{\mathbf{y}}$, representing the RVE of the micro problem, is split into a cortical bone part $\Omega_{\mathbf{b}}$ and a bone marrow part $\Omega_{\mathbf{m}}$. For any quantity, the indices $(\cdot)_{\mathbf{m}}$ and $(\cdot)_{\mathbf{b}}$ are used to denote the affiliation to each phase. If no index is present, the quantity or equation

is valid for both phases. We employ the following thermodynamic energy functional at the microscale:

$$\begin{aligned} \Pi = & \int_{\Omega_b} \Psi_b(\boldsymbol{\varepsilon}, \mathbf{E}, \mathbf{B}) dV + \int_{\Omega_m} \Psi_m(\boldsymbol{\varepsilon}, \boldsymbol{\varepsilon}^i, \mathbf{E}, \mathbf{B}) + \mathcal{C} dV \\ & + \int_{\Omega_m} \int_t \Delta(\dot{\boldsymbol{\varepsilon}}^i, \dot{\mathbf{A}}) dt dV + \int_{\Omega} \Psi_g(\nabla \cdot \mathbf{A}) dV - W_{\text{ext}}. \end{aligned} \quad (2.1)$$

The functional contains the energy densities Ψ_b and Ψ_m of both phases, a volume constraint \mathcal{C} , dissipation and gauge functionals (Δ and Ψ_g) and the potential of the generalized external forces W_{ext} . The main variables of the problem are then the mechanical displacements \mathbf{u} , the electric scalar potential φ and the magnetic vector potential \mathbf{A} , yielding seven unknown variables for the three-dimensional model. The state variables are the mechanical strain $\boldsymbol{\varepsilon}$, the electric field \mathbf{E} and the magnetic flux density \mathbf{B} , calculated as

$$\boldsymbol{\varepsilon} = \frac{1}{2} (\nabla \mathbf{u} + \nabla^T \mathbf{u}), \quad \mathbf{E} = -\nabla \varphi - \dot{\mathbf{A}} \quad \text{and} \quad \mathbf{B} = \nabla \times \mathbf{A}. \quad (2.2)$$

This way, two of the four Maxwell equations are already satisfied:

$$\begin{aligned} \nabla \times \mathbf{E} &= \nabla \times (-\nabla \varphi - \dot{\mathbf{A}}) = -\dot{\mathbf{B}} \quad \text{and} \\ \nabla \cdot \mathbf{B} &= \nabla \cdot (\nabla \times \mathbf{A}) = \mathbf{0}. \end{aligned} \quad (2.3)$$

For the mechanical strain, we use Voigt's notation [Mehrabadi and Cowin (1990)] as

$$\boldsymbol{\varepsilon} = (\varepsilon_{xx} \quad \varepsilon_{yy} \quad \varepsilon_{zz} \quad 2\varepsilon_{xy} \quad 2\varepsilon_{yz} \quad 2\varepsilon_{xz})^T. \quad (2.4)$$

Then, the energy densities for both phases are

$$\begin{aligned} \Psi_b &= \frac{1}{2} (\boldsymbol{\varepsilon} \cdot \mathbb{C}_b \cdot \boldsymbol{\varepsilon} - \mathbf{E} \cdot \boldsymbol{\xi}_b \cdot \mathbf{E} + \mathbf{B} \cdot \boldsymbol{\mu}_b^{-1} \cdot \mathbf{B}) - \mathbf{e}_b \cdot \boldsymbol{\varepsilon} \cdot \mathbf{E} \quad \text{and} \\ \Psi_m &= \frac{1}{2} ((\boldsymbol{\varepsilon} - \boldsymbol{\varepsilon}^i) \cdot \mathbb{C}_m \cdot (\boldsymbol{\varepsilon} - \boldsymbol{\varepsilon}^i) - \mathbf{E} \cdot \boldsymbol{\xi}_m \cdot \mathbf{E} + \mathbf{B} \cdot \boldsymbol{\mu}_m^{-1} \cdot \mathbf{B}), \end{aligned} \quad (2.5)$$

consisting of quadratic energies for mechanical, electric and magnetic effects, resulting in a linear problem. We include a piezoelectric energy term for the cortical bone phase. For the bone marrow phase, an inelastic strain $\boldsymbol{\varepsilon}^i$ is introduced. Here, \mathbb{C} is the mechanical stiffness tensor, $\boldsymbol{\xi}$ is the permittivity tensor, $\boldsymbol{\mu}^{-1}$ is the inverse permeability tensor and \mathbf{e}_b is the piezoelectric tensor. While it is possible to switch between state and flux variables via a Legendre transformation, the present formulation proves as the most suitable for our model, as it allows an easy inclusion of the Maxwell coupling and the electric dissipation. For linear problems, the transformation would change an extremal into a saddle point problem, thus excluding solvers, that require positive definiteness of the system matrix as a precondition. The constraint function reads

$$\mathcal{C} = \lambda \text{tr}(\boldsymbol{\varepsilon}^i), \quad (2.6)$$

enforcing volume conservation of the inelastic deformation. Here, λ is a Lagrange multiplier. The dissipation function is

$$\Delta = \frac{1}{2} (\boldsymbol{\mu}_v^{-1} |\dot{\boldsymbol{\varepsilon}}^i|^2 - \boldsymbol{\kappa} \mathbf{E}^2), \quad \text{with} \quad \mathbf{J} = \boldsymbol{\kappa} \mathbf{E}. \quad (2.7)$$

Thus, Δ governs the evolution of the inelastic strain and the energy loss due to conduction. The latter satisfies Ohm's law (Eq. (2.7), right). Both parts of the dissipation only occur in the bone marrow phase. Here, the viscosity parameter $\mu_v^{-1} > 0$, the electric conductivity tensor $\boldsymbol{\kappa} = \kappa_1 \mathbf{I}$, with the identity tensor \mathbf{I} , the electric conductivity $\kappa_1 > 0$ and the electric current density \mathbf{J} are introduced. The gauge function is

$$\Psi_g = \frac{\gamma}{2} (\nabla \cdot \mathbf{A})^2 \quad (2.8)$$

and ensures, that a unique solution for the magnetic vector potential \mathbf{A} is obtained by penalizing its divergence, effectively requiring, that $\nabla \cdot \mathbf{A}$ vanishes and thus improving the numerical stability [Semenov et al. (2006)]. The penalty parameter γ is a numerical parameter used to control the gauge term. Finally, the potential of generalized external forces is

$$W_{\text{ext}} = \int_{\Omega} (\mathbf{f} \cdot \mathbf{u} - q_v \cdot \varphi + \mathbf{j}_v \cdot \mathbf{A}) dV + \int_{\partial\Omega} (\mathbf{t} \cdot \mathbf{u} - q_s \cdot \varphi + \mathbf{j}_s \cdot \mathbf{A}) dA . \quad (2.9)$$

Here, \mathbf{f} and \mathbf{t} are the mechanical volume and surface forces, q_v and q_s are the electric volume and surface charges and \mathbf{j}_v and \mathbf{j}_s are the volume and surface currents.

By calculating the derivative of the energy density with respect to the state variables, we find the following constitutive equations for both phases:

$$\begin{aligned} \boldsymbol{\sigma} &:= \frac{\partial \Psi_b}{\partial \boldsymbol{\varepsilon}} = \mathbb{C}_b \cdot \boldsymbol{\varepsilon} - \mathbf{e}_b^T \cdot \mathbf{E} , \\ \mathbf{D} &:= -\frac{\partial \Psi_b}{\partial \mathbf{E}} = \mathbf{e}_b \cdot \boldsymbol{\varepsilon} + \boldsymbol{\xi}_b \cdot \mathbf{E} , \\ \mathbf{H} &:= \frac{\partial \Psi_b}{\partial \mathbf{B}} = \boldsymbol{\mu}_b^{-1} \cdot \mathbf{B} , \\ \\ \boldsymbol{\sigma} &:= \frac{\partial \Psi_m}{\partial \boldsymbol{\varepsilon}} = \mathbb{C}_m \cdot (\boldsymbol{\varepsilon} - \boldsymbol{\varepsilon}^i) , \\ \mathbf{D} &:= -\frac{\partial \Psi_m}{\partial \mathbf{E}} = \boldsymbol{\xi}_m \cdot \mathbf{E} \quad \text{and} \\ \mathbf{H} &:= \frac{\partial \Psi_m}{\partial \mathbf{B}} = \boldsymbol{\mu}_m^{-1} \cdot \mathbf{B} . \end{aligned} \quad (2.10)$$

For the bone marrow, the additional constitutive equations are

$$\begin{aligned} \boldsymbol{\sigma} &:= -\frac{\partial \Psi_m}{\partial \boldsymbol{\varepsilon}^i} = \mathbb{C}_m \cdot (\boldsymbol{\varepsilon} - \boldsymbol{\varepsilon}^i) \quad \text{and} \\ \mathbf{J} &:= \frac{\partial \Delta}{\partial \mathbf{E}} = -\frac{\partial \Delta}{\partial \dot{\mathbf{A}}} = \boldsymbol{\kappa}_m \mathbf{E} , \end{aligned} \quad (2.11)$$

introducing the flux quantities mechanical stress $\boldsymbol{\sigma}$, electric displacement \mathbf{D} and magnetic field strength \mathbf{H} . For the cortical bone phase the viscosity parameter μ_v^{-1} and the electric conductivity tensor $\boldsymbol{\kappa}$ vanish. The material tensors satisfy

$$\begin{aligned} \mathbb{C} &:= \frac{\partial \boldsymbol{\sigma}}{\partial \boldsymbol{\varepsilon}} , & \boldsymbol{\xi} &:= \frac{\partial \mathbf{D}}{\partial \mathbf{E}} , & \mathbf{e} &:= \frac{\partial \mathbf{D}}{\partial \boldsymbol{\varepsilon}} = -\left(\frac{\partial \boldsymbol{\sigma}}{\partial \mathbf{E}}\right)^T , \\ \boldsymbol{\mu}^{-1} &:= \frac{\partial \mathbf{H}}{\partial \mathbf{B}} , & \boldsymbol{\kappa} &:= \frac{\partial \mathbf{J}}{\partial \mathbf{E}} . \end{aligned} \quad (2.12)$$

2.3.4 Weak and strong form of the microscale problem

To calculate the weak and strong form of the problem, the energy functional has to become stationary with respect to the main variables and internal variables, leading to

$$\int_{t_0}^{t_1} \Pi dt \rightarrow \underset{\mathbf{u}, \varphi, \mathbf{A}, \boldsymbol{\varepsilon}^i}{stat} . \quad (2.13)$$

The stationary condition of the first variation of the energy functional reads then

$$\begin{aligned} \int_{\Omega_b} \left(\frac{\partial \Psi_b}{\partial \boldsymbol{\varepsilon}} \delta \boldsymbol{\varepsilon} + \frac{\partial \Psi_b}{\partial \mathbf{E}} \delta \mathbf{E} + \frac{\partial \Psi_b}{\partial \mathbf{B}} \delta \mathbf{B} \right) dV + \int_{\Omega_m} \left(\frac{\partial \Psi_m}{\partial \boldsymbol{\varepsilon}} \delta \boldsymbol{\varepsilon} + \frac{\partial \Psi_m}{\partial \boldsymbol{\varepsilon}^i} \delta \boldsymbol{\varepsilon}^i \right. \\ \left. + \frac{\partial \Psi_m}{\partial \mathbf{E}} \delta \mathbf{E} + \frac{\partial \Psi_m}{\partial \mathbf{B}} \delta \mathbf{B} + \frac{\partial \Delta}{\partial \dot{\boldsymbol{\varepsilon}}^i} \delta \dot{\boldsymbol{\varepsilon}}^i + \frac{\partial \Delta}{\partial \dot{\mathbf{A}}} \delta \dot{\mathbf{A}} + \lambda \mathbf{I} \delta \boldsymbol{\varepsilon}^i \right) dV \\ + \int_{\Omega} \frac{\partial \Psi_g}{\partial (\nabla \cdot \mathbf{A})} \delta (\nabla \cdot \mathbf{A}) dV - \delta W_{ext} = \delta \Pi = 0 \quad \forall \delta \mathbf{u}, \delta \varphi, \delta \mathbf{A}, \delta \boldsymbol{\varepsilon}^i. \end{aligned} \quad (2.14)$$

The variation of the generalized external forces is

$$\delta W_{ext} = \int_{\Omega} (\mathbf{f} \cdot \delta \mathbf{u} - q_v \cdot \delta \varphi + \mathbf{j}_v \cdot \delta \mathbf{A}) dV + \int_{\partial \Omega} (\mathbf{t} \cdot \delta \mathbf{u} - q_s \cdot \delta \varphi + \mathbf{j}_s \cdot \delta \mathbf{A}) dA . \quad (2.15)$$

Using the introduced energy densities, constraint, dissipation and gauge functions, Eqs. (2.5), (2.6), (2.7), (2.8), and inserting the constitutive equations Eq. (2.10), Eq. (2.14) simplifies to

$$\begin{aligned} \int_{\Omega} (\boldsymbol{\sigma} \cdot \delta \boldsymbol{\varepsilon} - \mathbf{D} \cdot \delta \mathbf{E} + \mathbf{H} \cdot \delta \mathbf{B} - \mathbf{J} \cdot \delta \mathbf{A} + \gamma (\nabla \cdot \mathbf{A}) \cdot \delta (\nabla \cdot \mathbf{A}) \\ + (-\boldsymbol{\sigma} + \mu_v^{-1} \dot{\boldsymbol{\varepsilon}}^i + \lambda \mathbf{I}) \delta \boldsymbol{\varepsilon}^i) dV - \delta W_{ext} = 0 \quad \forall \delta \mathbf{u}, \delta \varphi, \delta \mathbf{A}, \delta \boldsymbol{\varepsilon}^i. \end{aligned} \quad (2.16)$$

Here, the identity vector is denoted as \mathbf{I} . We find the evolution equation of the inelastic strain:

$$-\boldsymbol{\sigma} + \mu_v^{-1} \dot{\boldsymbol{\varepsilon}}^i + \lambda \mathbf{I} = \mathbf{0} . \quad (2.17)$$

To calculate the Lagrange multiplier, the trace is applied to Eq. (2.17):

$$-\text{tr}(\boldsymbol{\sigma}) + \underbrace{\mu_v^{-1} \text{tr}(\dot{\boldsymbol{\varepsilon}}^i)}_{=0} + \lambda \text{tr}(\mathbf{I}) = 0 \Rightarrow \lambda = \frac{1}{3} \text{tr}(\boldsymbol{\sigma}) . \quad (2.18)$$

The second term in Eq. (2.18) must vanish because of the introduced volume constraint. This leads to the final evolution equation

$$\dot{\boldsymbol{\varepsilon}}^i = \mu_v \boldsymbol{\sigma}_{dev} , \quad (2.19)$$

with $\boldsymbol{\sigma}_{dev} = \boldsymbol{\sigma} - \frac{1}{3} \text{tr}(\boldsymbol{\sigma}) \mathbf{I}$ denoting the deviatoric part of the mechanical stress $\boldsymbol{\sigma}$. The time integration of the evolution equation is discussed in Section 2.4.

To calculate the strong form of the problem, the remaining variational equation is used:

$$\int_{\Omega} (\boldsymbol{\sigma} \cdot \delta \boldsymbol{\varepsilon} - \mathbf{D} \cdot \delta \mathbf{E} + \mathbf{H} \cdot \delta \mathbf{B} - \mathbf{J} \cdot \delta \mathbf{A} + \gamma (\nabla \cdot \mathbf{A}) \cdot \delta (\nabla \cdot \mathbf{A})) dV - \delta W_{\text{ext}} = 0 \quad \forall \delta \mathbf{u}, \delta \varphi, \delta \mathbf{A}. \quad (2.20)$$

This form is later used to insert a FEM ansatz. We apply partial integration to each term. Details can be found in Appendix A (Sec. 2.7). We obtain

$$\begin{aligned} \nabla \cdot \boldsymbol{\sigma} + \mathbf{f} &= \mathbf{0} && \text{in } \Omega \\ \boldsymbol{\sigma} \cdot \mathbf{n} &= \mathbf{t} && \text{on } \partial\Omega \\ \nabla \cdot \mathbf{D} &= q_v && \text{in } \Omega \\ \mathbf{D} \cdot \mathbf{n} &= -q_s && \text{on } \partial\Omega \\ \nabla \times \mathbf{H} &= \dot{\mathbf{D}} + \mathbf{J} + \gamma \nabla (\nabla \cdot \mathbf{A}) + \mathbf{j}_v && \text{in } \Omega \\ \mathbf{H} \times \mathbf{n} &= \mathbf{j}_s - \gamma (\nabla \cdot \mathbf{A}) \mathbf{n} && \text{on } \partial\Omega \end{aligned} \quad (2.21)$$

recovering the mechanical equilibrium condition, the two remaining Maxwell equations and boundary conditions, including the gauge. Here, \mathbf{n} is the normal vector pointing outwards. Additionally, we receive the jump conditions between the phases ¹

$$\begin{aligned} [[\boldsymbol{\sigma}]]_{\text{bm}} \cdot \mathbf{n} &= \mathbf{t} && \text{on } \partial\Omega_{\text{bm}} \\ [[\mathbf{D}]]_{\text{bm}} \cdot \mathbf{n} &= -q_s && \text{on } \partial\Omega_{\text{bm}} \\ [[\mathbf{H}]]_{\text{bm}} \times \mathbf{n} &= \mathbf{j}_s - \gamma [[\nabla \cdot \mathbf{A}]]_{\text{bm}} \mathbf{n} && \text{on } \partial\Omega_{\text{bm}} \end{aligned} \quad (2.22)$$

on the interface $\partial\Omega_{\text{bm}}$ and the evolution equation of the inelastic strain Eq. (2.19) in Ω_{m} . Here $[[\cdot]]_{12} := (\cdot)_1 - (\cdot)_2$ denotes the difference between the phases. It should be noted that the strong form is valid for both phases, but the calculation of the flux variables and the inelastic strain evolution depends on the specific material parameters and thus in which phase the calculation is done.

2.3.5 Macroscale problem

For the macroscale, the following boundary value problem in the domain Ω_{x} has to be solved: find the set $\{\bar{\mathbf{u}}, \bar{\varphi}, \bar{\mathbf{A}}\}$, such that

$$\begin{aligned} \nabla \cdot \bar{\boldsymbol{\sigma}} + \bar{\mathbf{f}} &= \mathbf{0} && \text{in } \Omega_{\text{x}} \\ \bar{\boldsymbol{\sigma}} \cdot \mathbf{n} &= \bar{\mathbf{t}} && \text{on } \partial\Omega_{\text{x}} \\ \nabla \cdot \bar{\mathbf{D}} &= \bar{q}_v && \text{in } \Omega_{\text{x}} \\ \bar{\mathbf{D}} \cdot \mathbf{n} &= -\bar{q}_s && \text{on } \partial\Omega_{\text{x}} \\ \nabla \times \bar{\mathbf{H}} &= \dot{\bar{\mathbf{D}}} + \bar{\mathbf{J}} + \gamma \nabla (\nabla \cdot \bar{\mathbf{A}}) + \bar{\mathbf{j}}_v && \text{in } \Omega_{\text{x}} \\ \bar{\mathbf{H}} \times \mathbf{n} &= \bar{\mathbf{j}}_s - \gamma (\nabla \cdot \bar{\mathbf{A}}) \mathbf{n} && \text{on } \partial\Omega_{\text{x}}, \end{aligned} \quad (2.23)$$

¹Corrected the missing equation part, cf. Blaszczyk and Hackl (2022).

with the state variables

$$\bar{\boldsymbol{\varepsilon}} = \frac{1}{2} (\nabla \bar{\mathbf{u}} + \nabla^T \bar{\mathbf{u}}), \quad \bar{\mathbf{E}} = -\nabla \bar{\varphi} - \dot{\bar{\mathbf{A}}} \quad \text{and} \quad \bar{\mathbf{B}} = \nabla \times \bar{\mathbf{A}}, \quad (2.24)$$

and the calculation of the fluxes depending on the microscale calculations

$$(\bar{\boldsymbol{\sigma}}, \bar{\mathbf{D}}, \dot{\bar{\mathbf{D}}}, \bar{\mathbf{H}}, \bar{\mathbf{J}}) = f_{\text{RVE}}(\bar{\boldsymbol{\varepsilon}}, \bar{\mathbf{E}}, \bar{\mathbf{B}}). \quad (2.25)$$

We transform the strong form into the weak form by multiplying with test functions of the main variables and again using partial integration:

$$\begin{aligned} & \int_{\Omega_{\mathbf{x}}} (\bar{\boldsymbol{\sigma}} \cdot \delta \bar{\boldsymbol{\varepsilon}} - \bar{\mathbf{D}} \cdot \delta \bar{\mathbf{E}} + \bar{\mathbf{H}} \cdot \delta \bar{\mathbf{B}} - \bar{\mathbf{J}} \cdot \delta \bar{\mathbf{A}} \\ & + \gamma (\nabla \cdot \bar{\mathbf{A}}) \cdot \delta (\nabla \cdot \bar{\mathbf{A}})) dV - \delta \bar{W}_{\text{ext}} = 0 \quad \forall \delta \bar{\mathbf{u}}, \delta \bar{\varphi}, \delta \bar{\mathbf{A}}. \end{aligned} \quad (2.26)$$

Here, the variation of the macroscopic generalized external forces is

$$\delta \bar{W}_{\text{ext}} = \int_{\Omega_{\mathbf{x}}} (\bar{\mathbf{f}} \cdot \delta \bar{\mathbf{u}} - \bar{q}_v \cdot \delta \bar{\varphi} + \bar{\mathbf{j}}_v \cdot \delta \bar{\mathbf{A}}) dV + \int_{\partial \Omega_{\mathbf{x}}} (\bar{\mathbf{t}} \cdot \delta \bar{\mathbf{u}} - \bar{q}_s \cdot \delta \bar{\varphi} + \bar{\mathbf{j}}_s \cdot \delta \bar{\mathbf{A}}) dA. \quad (2.27)$$

This form is again used in the next section to formulate the FEM.

2.4 Numerical implementation

2.4.1 Finite element method

To solve the boundary value problems on both scales, we insert a standard finite element approach [Zienkiewicz et al. (2005)] into the weak form of the problem for all main variables. In this section, we derive the resulting system for the microscale. It should be noted that the same system has to be solved for the macroscale, but each quantity (\cdot) has to be replaced by its macro-average quantity $(\bar{\cdot})$. The inelastic strain is only present on the microscale and vanishes on the macroscale. Its calculation is not done via the FEM, but directly by using the evolution equation Eq. (2.19) on the integration point level. Details regarding the calculation of macro-fluxes and consistent material tensors are given in the next subsection. Here, we denote nodal FEM values by $(\hat{\cdot})$. For the evolution equation of the inelastic strain on the micro-scale, we apply an explicit Euler scheme, yielding:

$$\boldsymbol{\varepsilon}_{n+1}^i = \boldsymbol{\varepsilon}_n^i + \Delta t \dot{\boldsymbol{\varepsilon}}^i \quad \text{with} \quad \dot{\boldsymbol{\varepsilon}}^i = \mu_v \boldsymbol{\sigma}_{\text{dev}}. \quad (2.28)$$

Here, Δt is the time increment between two time steps. The standard FEM approach for the remaining system is

$$\begin{aligned} \mathbf{u} &\approx \mathbf{N}_u \hat{\mathbf{u}} & \boldsymbol{\varphi} &\approx \mathbf{N}_\varphi \hat{\boldsymbol{\varphi}} & \mathbf{A} &\approx \mathbf{N}_A \hat{\mathbf{A}} \\ \delta \mathbf{u} &\approx \mathbf{N}_u \delta \hat{\mathbf{u}} & \delta \boldsymbol{\varphi} &\approx \mathbf{N}_\varphi \delta \hat{\boldsymbol{\varphi}} & \delta \mathbf{A} &\approx \mathbf{N}_A \delta \hat{\mathbf{A}} \end{aligned} \quad (2.29)$$

approximating the main variable and their variations by shape functions times the nodal values of the functions $(\cdot) \approx \mathbf{N} \cdot (\hat{\cdot})$. For the state variables and the gauge this approach yields

$$\begin{aligned} \hat{\boldsymbol{\varepsilon}} &= \mathbf{B}_u \hat{\mathbf{u}}, & \hat{\mathbf{E}} &= -\mathbf{B}_{\text{grad}} \hat{\boldsymbol{\varphi}} - \mathbf{N}_A \hat{\mathbf{A}}, \\ \hat{\mathbf{B}} &= \mathbf{B}_{\text{curl}} \hat{\mathbf{A}}, & \nabla \cdot \hat{\mathbf{A}} &= \mathbf{B}_{\text{div}} \hat{\mathbf{A}}. \end{aligned} \quad (2.30)$$

Here, the operator matrices are

$$\begin{aligned} \mathbf{B}_u &= \begin{pmatrix} \frac{\partial}{\partial x} & 0 & 0 \\ 0 & \frac{\partial}{\partial y} & 0 \\ 0 & 0 & \frac{\partial}{\partial z} \\ \frac{\partial}{\partial y} & \frac{\partial}{\partial x} & 0 \\ 0 & \frac{\partial}{\partial z} & \frac{\partial}{\partial y} \\ \frac{\partial}{\partial z} & 0 & \frac{\partial}{\partial x} \end{pmatrix} \cdot \mathbf{N}_u \\ \mathbf{B}_{\text{grad}} &= \begin{pmatrix} \frac{\partial}{\partial x} \\ \frac{\partial}{\partial y} \\ \frac{\partial}{\partial z} \end{pmatrix} \cdot \mathbf{N}_\varphi \\ \mathbf{B}_{\text{curl}} &= \begin{pmatrix} 0 & \frac{\partial}{\partial z} & -\frac{\partial}{\partial y} \\ -\frac{\partial}{\partial z} & 0 & \frac{\partial}{\partial x} \\ \frac{\partial}{\partial y} & -\frac{\partial}{\partial x} & 0 \end{pmatrix} \cdot \mathbf{N}_A \\ \mathbf{B}_{\text{div}} &= \begin{pmatrix} \frac{\partial}{\partial x} & \frac{\partial}{\partial y} & \frac{\partial}{\partial z} \end{pmatrix} \cdot \mathbf{N}_A \end{aligned} \quad (2.31)$$

Inserting these equations into the reduced weak form of the micro-problem Eq. (2.20) and by using the arbitrariness of the test functions, we find the final equation system in matrix form as follows (a detailed derivation is given in Appendix B (Sec. 2.8)):

$$\mathbf{R} := \mathbf{F} - \mathbf{M}\ddot{\mathbf{d}} - \mathbf{C}\dot{\mathbf{d}} - \mathbf{K}\mathbf{d} \stackrel{!}{=} \mathbf{0} \quad (2.32)$$

with the residual vector $\mathbf{R} = (\mathbf{R}_u \quad \mathbf{R}_\varphi \quad \mathbf{R}_A)^T =$

$$\begin{pmatrix} \hat{\mathbf{f}} + \int_{\Omega} -\mathbf{B}_u^T \hat{\boldsymbol{\sigma}} dV \\ \hat{\mathbf{q}} + \int_{\Omega} -\mathbf{B}_{\text{grad}}^T \hat{\mathbf{D}} dV \\ \hat{\mathbf{j}} + \int_{\Omega} (\mathbf{N}_A^T (\hat{\mathbf{D}} + \hat{\mathbf{J}}) - \mathbf{B}_{\text{curl}}^T \hat{\mathbf{H}} - \gamma \mathbf{B}_{\text{div}} \mathbf{B}_{\text{div}}^T \hat{\mathbf{A}}) dV \end{pmatrix} \quad (2.33)$$

and the generalized force and displacement vectors together with the mass, damping and stiffness matrices as follows:

$$\begin{aligned} \mathbf{d} &:= \begin{pmatrix} \hat{\mathbf{u}} \\ \hat{\boldsymbol{\varphi}} \\ \hat{\mathbf{A}} \end{pmatrix}, & \mathbf{F} &= \begin{pmatrix} \hat{\mathbf{f}} \\ \hat{\mathbf{q}} \\ \hat{\mathbf{j}} \end{pmatrix}, \\ \mathbf{M} &= \begin{pmatrix} \mathbf{0} & \mathbf{0} & \mathbf{0} \\ \mathbf{0} & \mathbf{0} & \mathbf{0} \\ \mathbf{0} & \mathbf{0} & \mathbf{M}_{AA} \end{pmatrix}, & \mathbf{C} &= \begin{pmatrix} \mathbf{0} & \mathbf{0} & \mathbf{C}_{uA} \\ \mathbf{0} & \mathbf{0} & \mathbf{C}_{\varphi A} \\ \mathbf{C}_{Au} & \mathbf{C}_{A\varphi} & \mathbf{C}_{AA} \end{pmatrix}, \\ \mathbf{K} &= \begin{pmatrix} \mathbf{K}_{uu} & \mathbf{K}_{u\varphi} & \mathbf{0} \\ \mathbf{K}_{\varphi u} & \mathbf{K}_{\varphi\varphi} & \mathbf{0} \\ \mathbf{0} & \mathbf{K}_{A\varphi} & \mathbf{K}_{AA} \end{pmatrix}. \end{aligned}$$

$$\begin{aligned}
\mathbf{K}_{\mathbf{u}\mathbf{u}} &:= -\frac{\partial \mathbf{R}_{\mathbf{u}}}{\partial \hat{\mathbf{u}}} = \int_{\Omega} \mathbf{B}_{\mathbf{u}}^T \mathbf{C}_{\text{tang}} \mathbf{B}_{\mathbf{u}} \, dV, \\
\mathbf{K}_{\mathbf{u}\varphi} &:= -\frac{\partial \mathbf{R}_{\mathbf{u}}}{\partial \hat{\varphi}} = \int_{\Omega} \mathbf{B}_{\mathbf{u}}^T \mathbf{e}^T \mathbf{B}_{\text{grad}} \, dV, \\
\mathbf{K}_{\varphi\mathbf{u}} &:= -\frac{\partial \mathbf{R}_{\varphi}}{\partial \hat{\mathbf{u}}} = \int_{\Omega} \mathbf{B}_{\text{grad}}^T \mathbf{e} \mathbf{B}_{\mathbf{u}} \, dV, \\
\mathbf{K}_{\varphi\varphi} &:= -\frac{\partial \mathbf{R}_{\varphi}}{\partial \hat{\varphi}} = \int_{\Omega} -\mathbf{B}_{\text{grad}}^T \boldsymbol{\xi} \mathbf{B}_{\text{grad}} \, dV, \\
\mathbf{K}_{\mathbf{A}\mathbf{A}} &:= -\frac{\partial \mathbf{R}_{\mathbf{A}}}{\partial \hat{\mathbf{A}}} = \int_{\Omega} \mathbf{B}_{\text{curl}}^T \boldsymbol{\mu}^{-1} \mathbf{B}_{\text{curl}} + \gamma \mathbf{B}_{\text{div}} \mathbf{B}_{\text{div}}^T \, dV, \\
\mathbf{K}_{\mathbf{A}\varphi} &:= -\frac{\partial \mathbf{R}_{\mathbf{A}}}{\partial \hat{\varphi}} = \int_{\Omega} \mathbf{N}_{\mathbf{A}}^T \boldsymbol{\kappa} \mathbf{B}_{\text{grad}} \, dV, \\
\mathbf{C}_{\mathbf{u}\mathbf{A}} &:= -\frac{\partial \mathbf{R}_{\mathbf{u}}}{\partial \hat{\mathbf{A}}} = \int_{\Omega} \mathbf{B}_{\mathbf{u}}^T \mathbf{e}^T \mathbf{N}_{\mathbf{A}} \, dV, \\
\mathbf{C}_{\mathbf{A}\mathbf{u}} &:= -\frac{\partial \mathbf{R}_{\mathbf{A}}}{\partial \hat{\mathbf{u}}} = \int_{\Omega} -\mathbf{N}_{\mathbf{A}}^T \mathbf{e} \mathbf{B}_{\mathbf{u}} \, dV, \\
\mathbf{C}_{\varphi\mathbf{A}} &:= -\frac{\partial \mathbf{R}_{\varphi}}{\partial \hat{\mathbf{A}}} = \int_{\Omega} -\mathbf{B}_{\text{grad}}^T \boldsymbol{\xi} \mathbf{N}_{\mathbf{A}} \, dV, \\
\mathbf{C}_{\mathbf{A}\varphi} &:= -\frac{\partial \mathbf{R}_{\mathbf{A}}}{\partial \hat{\varphi}} = \int_{\Omega} \mathbf{N}_{\mathbf{A}}^T \boldsymbol{\xi} \mathbf{B}_{\text{grad}} \, dV, \\
\mathbf{C}_{\mathbf{A}\mathbf{A}} &:= -\frac{\partial \mathbf{R}_{\mathbf{A}}}{\partial \hat{\mathbf{A}}} = \int_{\Omega} \mathbf{N}_{\mathbf{A}}^T \boldsymbol{\kappa} \mathbf{N}_{\mathbf{A}} \, dV, \\
\mathbf{M}_{\mathbf{A}\mathbf{A}} &:= -\frac{\partial \mathbf{R}_{\mathbf{A}}}{\partial \hat{\mathbf{A}}} = \int_{\Omega} \mathbf{N}_{\mathbf{A}}^T \boldsymbol{\xi} \mathbf{N}_{\mathbf{A}} \, dV. \tag{2.34}
\end{aligned}$$

The material tensors depend again on the phase. We calculate the mechanical stiffness tangent matrix \mathbf{C}_{tang} by introducing a time discretization as:

$$\mathbf{C}_{\text{tang}} = \frac{\partial \boldsymbol{\sigma}_{n+1}}{\partial \boldsymbol{\varepsilon}_{n+1}} = \begin{cases} \mathbf{C}_{\text{b}} & \text{in } \Omega_{\text{b}} \\ \mathbf{C}_{\text{m}} - \mathbf{C}_{\text{m}} \frac{\partial \boldsymbol{\varepsilon}_{n+1}^i}{\partial \boldsymbol{\varepsilon}_{n+1}} & \text{in } \Omega_{\text{m}} \end{cases} \tag{2.35}$$

For the bone marrow phase, the calculation depends on the inelastic strain $\boldsymbol{\varepsilon}_{n+1}^i$:

$$\frac{\partial \boldsymbol{\varepsilon}_{n+1}^i}{\partial \boldsymbol{\varepsilon}_{n+1}} = \mu_{\text{v}} \frac{\partial \boldsymbol{\sigma}_{\text{dev}}}{\partial \boldsymbol{\sigma}} \underbrace{\frac{\partial \boldsymbol{\sigma}}{\partial \boldsymbol{\varepsilon}_{n+1}}}_{\mathbf{C}_{\text{m}}}, \tag{2.36}$$

with

$$\mathbf{D}_{\text{devd}} := \frac{\partial \boldsymbol{\sigma}_{\text{dev}}}{\partial \boldsymbol{\sigma}} = \mathbf{I} - \frac{1}{3} \begin{pmatrix} 1 & 1 & 1 & 0 & 0 & 0 \\ 1 & 1 & 1 & 0 & 0 & 0 \\ 1 & 1 & 1 & 0 & 0 & 0 \\ 0 & 0 & 0 & 0 & 0 & 0 \\ 0 & 0 & 0 & 0 & 0 & 0 \\ 0 & 0 & 0 & 0 & 0 & 0 \end{pmatrix} = \frac{1}{3} \begin{pmatrix} 2 & -1 & -1 & 0 & 0 & 0 \\ -1 & 2 & -1 & 0 & 0 & 0 \\ -1 & -1 & 2 & 0 & 0 & 0 \\ 0 & 0 & 0 & 3 & 0 & 0 \\ 0 & 0 & 0 & 0 & 3 & 0 \\ 0 & 0 & 0 & 0 & 0 & 3 \end{pmatrix}. \quad (2.37)$$

The mechanical stiffness tangent matrix for the bone marrow phase is then

$$\mathbb{C}_{\text{tang}} = \mathbb{C}_m - \mathbb{C}_m (\mu_v \mathbf{D}_{\text{devd}} \mathbb{C}_m) \quad \text{in } \Omega_m. \quad (2.38)$$

In order to solve the resulting second-order differential equation system, a suitable time integration scheme is necessary. Here we use a JWH- α -scheme introduced in Kadapa et al. (2017), where also details regarding advantages and implementation of this method can be found. For the time integration, the time increment Δt and the additional numerical parameter ρ_∞ are needed. By combining the method with a regular Newton-Raphson scheme, we transform the matrix system of Eq. (2.32) to

$$\mathbf{R}^{i+1} := \mathbf{R}^i(d_{n+\alpha_f}, v_{n+\alpha_f}, \dot{v}_{n+\alpha_m}) - \mathbf{S} \Delta \mathbf{d} \stackrel{!}{=} \mathbf{0}, \quad (2.39)$$

with the index denoting the iteration and the generalized tangent matrix

$$\mathbf{S} = \frac{\alpha_m^2}{\alpha_f \gamma_a^2 \Delta t^2} \mathbf{M} + \frac{\alpha_m}{\gamma_a \Delta t} \mathbf{C} + \alpha_f \mathbf{K}, \quad (2.40)$$

which is the Jacobian of the system. Here $\Delta \mathbf{d}$ is the increment of the solution vector and α_f , α_m and γ_a are numerical parameters depending on ρ_∞ [Kadapa et al. (2017)]. The residual $\mathbf{R}^i(d_{n+\alpha_f}, v_{n+\alpha_f}, \dot{v}_{n+\alpha_m})$ is calculated from either initial conditions for the first iteration of the first time step or else from the previous increment [Kadapa et al. (2017)]. The resulting tangent matrix \mathbf{S} is neither symmetric nor positive definite, limiting the choices for a suitable solver of the linear system.

2.4.2 Transition between the scales

To connect the macro- and microscale in FE², it is important to discuss the transition between the scales. The Hill-Mandel conditions [Hill (1963), Hill (1972), Schröder (2009), Schröder et al. (2016), Labusch et al. (2019); Karimi et al. (2019)] have to be fulfilled, guaranteeing energy conservation during the scale transition. Thus, the virtual work on the macroscale has to be equal to the virtual work on the microscale:

$$\bar{\boldsymbol{\sigma}} \cdot \delta \bar{\boldsymbol{\varepsilon}} = \frac{1}{\Omega} \int_{\Omega} \boldsymbol{\sigma} \cdot \delta \boldsymbol{\varepsilon} dV, \quad \bar{\mathbf{D}} \cdot \delta \bar{\mathbf{E}} = \frac{1}{\Omega} \int_{\Omega} \mathbf{D} \cdot \delta \mathbf{E} dV, \quad \bar{\mathbf{B}} \cdot \delta \bar{\mathbf{H}} = \frac{1}{\Omega} \int_{\Omega} \mathbf{B} \cdot \delta \mathbf{H} dV. \quad (2.41)$$

For the macro-to-micro transition, these conditions can be fulfilled by three different types of boundary conditions on the microscale: Dirichlet, Neumann and periodic boundary conditions [Ilić et al. (2010), Schröder (2000), Schröder and Hackl (2013)]. Here we chose

periodic boundary conditions, as they are the only type of boundary condition, where the results on the microscale are independent from the relative geometry of the RVE [Schröder (2000), Schröder and Hackl (2013)]. Additionally, as the RVE is periodic in space, this type of boundary condition is the most suitable. In the program, the periodic boundary conditions were applied by fixing all degrees of freedom at all corner nodes, preventing rigid body motions, and linking all degrees of freedom at opposite faces of the RVE, ensuring the periodicity. The micro-state variables consist then of two parts: a term resulting from the microscopic main variables (denoted by $\tilde{\cdot}$), whose fluctuations are calculated, and a term contributed by the macroscale:

$$\boldsymbol{\varepsilon} = \tilde{\boldsymbol{\varepsilon}}(\mathbf{y}) + \bar{\boldsymbol{\varepsilon}}(\mathbf{x}), \quad \mathbf{E} = \tilde{\mathbf{E}}(\mathbf{y}) + \bar{\mathbf{E}}(\mathbf{x}), \quad \mathbf{B} = \tilde{\mathbf{B}}(\mathbf{y}) + \bar{\mathbf{B}}(\mathbf{x}). \quad (2.42)$$

This way, we calculate the flux variables on the microscale. For the micro-to-macro transition, the volume average of these flux quantities is sent back to the macroscale:

$$\begin{aligned} \bar{\boldsymbol{\sigma}}(\mathbf{x}) &= \frac{1}{\Omega} \int_{\Omega} \boldsymbol{\sigma}(\mathbf{y}) \, dV, & \bar{\mathbf{D}}(\mathbf{x}) &= \frac{1}{\Omega} \int_{\Omega} \mathbf{D}(\mathbf{y}) \, dV, & \dot{\bar{\mathbf{D}}}(\mathbf{x}) &= \frac{1}{\Omega} \int_{\Omega} \dot{\mathbf{D}}(\mathbf{y}) \, dV, \\ \bar{\mathbf{H}}(\mathbf{x}) &= \frac{1}{\Omega} \int_{\Omega} \mathbf{H}(\mathbf{y}) \, dV, & \bar{\mathbf{J}}(\mathbf{x}) &= \frac{1}{\Omega} \int_{\Omega} \mathbf{J}(\mathbf{y}) \, dV. \end{aligned} \quad (2.43)$$

In this model, energy dissipation is considered in two ways. For the electric current \mathbf{J} , the average is calculated and included in the scale transition, resulting in no energy loss during the scale transition. For the inelastic strain $\boldsymbol{\varepsilon}^i$, the complete state in every point and for every RVE is saved. Thus, the dissipation occurs only on the microscale and the energy conservation is fulfilled², as the virtual work send to the microscale is equal to the virtual work send back added to the energy dissipation on the microscale. With the flux variables available on the macroscale, it is now possible to obtain the macro-residual for the Newton-Raphson method and the calculation of consistent macro-tangent moduli remains, which are needed for the iteration. The definitions of those moduli read

$$\begin{aligned} \bar{\mathbb{C}} &:= \frac{\partial \bar{\boldsymbol{\sigma}}}{\partial \bar{\boldsymbol{\varepsilon}}}, & \bar{\boldsymbol{\xi}} &:= \frac{\partial \bar{\mathbf{D}}}{\partial \bar{\mathbf{E}}}, & \bar{\mathbf{e}} &:= \frac{\partial \bar{\mathbf{D}}}{\partial \bar{\boldsymbol{\varepsilon}}} \\ \bar{\boldsymbol{\mu}}^{-1} &:= \frac{\partial \bar{\mathbf{H}}}{\partial \bar{\mathbf{B}}}, & \bar{\boldsymbol{\kappa}} &:= \frac{\partial \bar{\mathbf{J}}}{\partial \bar{\mathbf{E}}}. \end{aligned} \quad (2.44)$$

The calculation can be done by applying a small numerical perturbation $\Delta_{\text{tol}} = 10^{-8}$ to each entry of the corresponding state variable

$$\bar{\boldsymbol{\varepsilon}}^{p_i} = \bar{\boldsymbol{\varepsilon}} + \Delta_{\text{tol}} e_i, \quad \bar{\mathbf{E}}^{p_i} = \bar{\mathbf{E}} + \Delta_{\text{tol}} e_i, \quad \bar{\mathbf{B}}^{p_i} = \bar{\mathbf{B}} + \Delta_{\text{tol}} e_i, \quad (2.45)$$

with the i -th unit vector e_i , and then calculating each entry of the macroscopic tangent tensors by evaluating the perturbed fluxes $\bar{\boldsymbol{\sigma}}^{p_i}$, $\bar{\mathbf{D}}^{p_i}$, $\bar{\mathbf{H}}^{p_i}$, $\bar{\mathbf{J}}^{p_i}$ by means of the RVE as

$$\begin{aligned} \bar{\mathbb{C}}_{ji} &= \frac{\bar{\sigma}_j^{p_i} - \bar{\sigma}_j}{\bar{\varepsilon}_j^{p_i} - \bar{\varepsilon}_j}, & \bar{\boldsymbol{\xi}}_{ji} &= \frac{\bar{D}_j^{p_i} - \bar{D}_j}{\bar{E}_j^{p_i} - \bar{E}_j}, & \bar{\mathbf{e}}_{ji} &= \frac{\bar{D}_j^{p_i} - \bar{D}_j}{\bar{\varepsilon}_j^{p_i} - \bar{\varepsilon}_j}, \\ \bar{\boldsymbol{\mu}}_{ji}^{-1} &= \frac{\bar{H}_j^{p_i} - \bar{H}_j}{\bar{B}_j^{p_i} - \bar{B}_j}, & \bar{\boldsymbol{\kappa}}_{ji} &= \frac{\bar{J}_j^{p_i} - \bar{J}_j}{\bar{E}_j^{p_i} - \bar{E}_j}. \end{aligned} \quad (2.46)$$

Since for our model the same RVE is used everywhere and the non-linearity from the inelastic strain is very small, this calculation has to be done only once for all RVEs and all time steps, making this approach very efficient. Together with the calculated macrostate variables, this allows to solve the macroscopic FE problem.

²Corrected spelling, cf. Błaszczak and Hackl (2022)

2.4.3 Implementation

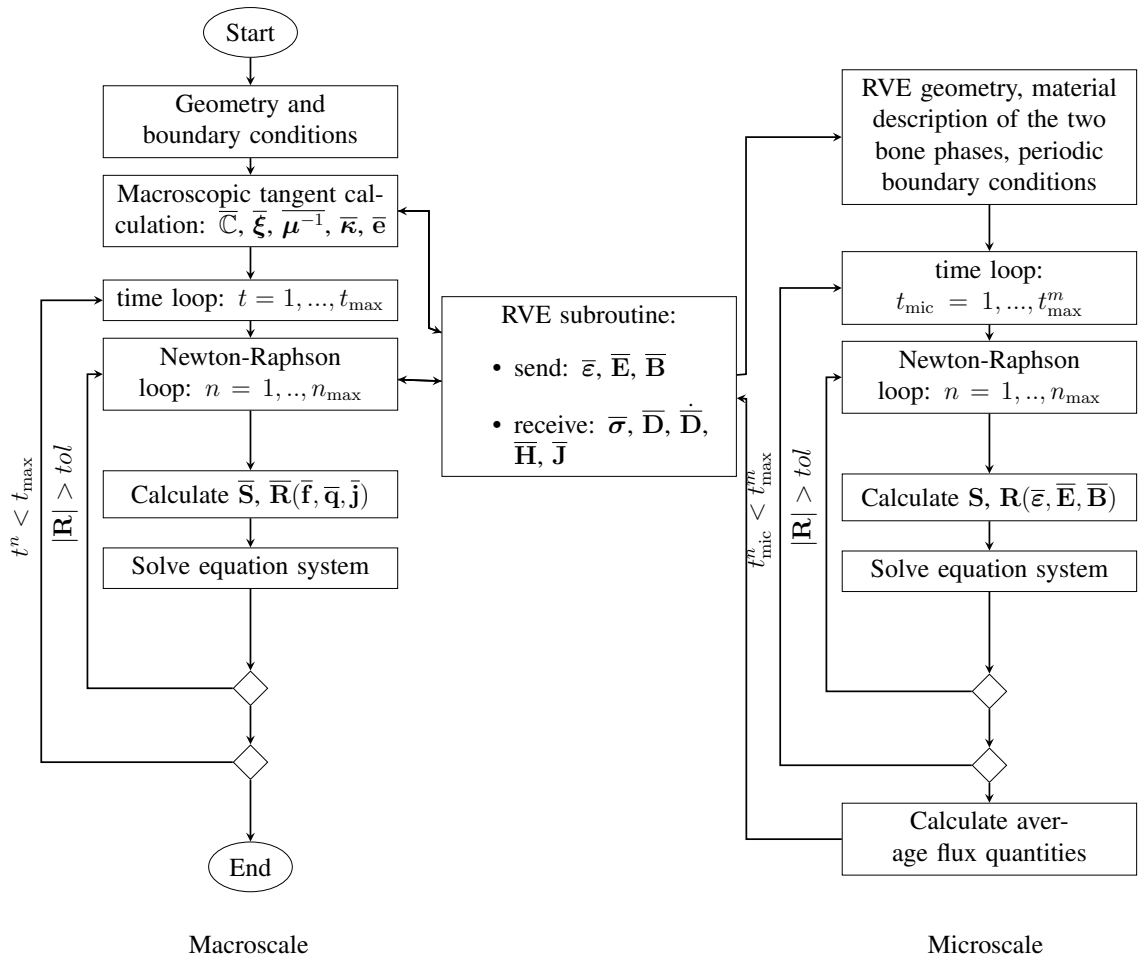


Figure 2.3: Program flow of the multiscale simulations.

For the simulations, we implemented a computer program in the language JULIA [Bezanson et al. (2022)], using mainly the packages JUAUFEM³ [Carlsson and Ekre (2022)] and COHERENTSTRUCTURES [de Diego et al. (2022)]. As the microscale calculations are not dependent on each other, we have parallelized the macroscale element routine, increasing the speed of the computations drastically. As the inelastic strain $\boldsymbol{\varepsilon}^i$ is only present in the microscale, we used HDF5 files to store the complete state of the inelastic strain for every RVE for the previous and current time step. Thus, for the inelastic strain evolution no information is lost. In order to solve the linear systems, we used the BiCGStab(l) method of the package KRYLOVMETHODS [Ruthotto and Treister (2022)], as it is stable, fast even without preconditioning the problem and can be used for any matrix type. Regarding the structure of the program, Figure 2.3 shows the procedure.

³Since the publication date, the package JuAFEM.jl has been renamed to Ferrite.jl, see citation for details.

2.5 Simulation results

2.5.1 Parameters and material tensors

In this subsection, we discuss the numerical and material parameters employed. Unless explicitly stated⁴ otherwise, the parameters from this subsection are used in all simulations. Regarding the numerical parameters, we use the same parameters for both scales. The time integration parameter is $\rho_\infty = 0.5$, the Newton-Raphson tolerance is $\text{tol}_N = 1 \cdot 10^{-8}$ and the gauge penalty parameter is $\gamma = 1.0 \text{ s}^2 \text{ A}^2 / (\text{kg m})$. The load and numerical time step increment depending on the model are shown in Table 2.1.

Model	Load	Time step
Microscale cube	$\bar{\varepsilon}_{yz} = 1 \cdot 10^{-5}$	$\Delta_t = 1 \cdot 10^{-3} \text{ s}$
Cylinder	$u_{\max} = 2 \cdot 10^{-6} \text{ m}$	$\Delta_t = 1 \cdot 10^{-2} \text{ s}$
Femur bone	$u_{\max} = 2 \cdot 10^{-6} \text{ m}$	$\Delta_t = 1 \cdot 10^{-2} \text{ s}$

Table 2.1: Load and numerical time step increment for the different models.

The used default material parameters are shown in Table 2.2. Young's modulus and Poisson's ratio for both phases can be found in [Steeb (2010)]. The piezoelectric coefficient can be found in [Fukada and Yasuda (1957)]. For the magnetic properties, bone is considered as a nonmagnetizable material, thus having the same permeability as the vacuum [Güzelsu and Saha (1981)]. All other parameters are of rather academical nature and influence the results only marginally. The resulting material tensors read

$$\mathbb{C} = \frac{E}{(1+\nu)(1-2\nu)} \cdot \begin{pmatrix} 1-\nu & \nu & \nu & 0 & 0 & 0 \\ \nu & 1-\nu & \nu & 0 & 0 & 0 \\ \nu & \nu & 1-\nu & 0 & 0 & 0 \\ 0 & 0 & 0 & \frac{1-2\nu}{2} & 0 & 0 \\ 0 & 0 & 0 & 0 & \frac{1-2\nu}{2} & 0 \\ 0 & 0 & 0 & 0 & 0 & \frac{1-2\nu}{2} \end{pmatrix}, \quad (2.47)$$

$$\begin{aligned} \boldsymbol{\xi} &= \begin{pmatrix} \xi_1 & 0 & 0 \\ 0 & \xi_1 & 0 \\ 0 & 0 & \xi_1 \end{pmatrix}, & \mathbf{e} &= \begin{pmatrix} 0 & 0 & 0 & 0 & e_{15} & 0 \\ 0 & 0 & 0 & 0 & 0 & -e_{15} \\ 0 & 0 & 0 & 0 & 0 & 0 \end{pmatrix}, \\ \boldsymbol{\mu}^{-1} &= \begin{pmatrix} \mu_c^{-1} & 0 & 0 \\ 0 & \mu_c^{-1} & 0 \\ 0 & 0 & \mu_c^{-1} \end{pmatrix}, & \boldsymbol{\kappa} &= \begin{pmatrix} \kappa_1 & 0 & 0 \\ 0 & \kappa_1 & 0 \\ 0 & 0 & \kappa_1 \end{pmatrix}. \end{aligned} \quad (2.48)$$

We assume linear isotropic material everywhere, excluding the piezoelectric tensor which is preferential in the z -axis due to the longitudinal orientation of the collagen fibers. It should be noted, that due to the form of the piezoelectric tensor, the material model as a whole is non-isotropic.

For the generation of the meshes, we used the program GMSH [Geuzaine and Remacle (2022)]. We did the visualization of the results with PARAVIEW [Kitware Inc. (2022)] and JULIA [Bezanson et al. (2022)].

⁴Corrected spelling, cf. Błaszczuk and Hackl (2022)

Material parameter		Cortical bone		Bone marrow	
Young's modulus	E	22.0	GPa	2.0	GPa
Poisson's ratio	ν	0.32	-	0.3	-
Permittivity	ξ_1	$8.85 \cdot 10^{-12}$	F/m	$8.85 \cdot 10^{-12}$	F/m
Permeability	μ_c	$1.257 \cdot 10^{-6}$	H/m	$1.257 \cdot 10^{-6}$	H/m
Piezoelectric coefficient	e_{15}	$3.0 \cdot 10^{-3}$	A s/m ²	0	A s/m ²
Electric conductivity	κ_1	0	S/m	$1.0 \cdot 10^4$	S/m
Viscosity parameter	μ_v	0	s/GPa	$0.5 \cdot \Delta_t$	s/GPa

Table 2.2: Default material parameters.

2.5.2 Microscale model

In this subsection, we restrict ourselves to microscale simulations. In order to compare periodic RVEs for different stages of osteoporosis, we introduce the lengths parameters a and b (Figure 2.4), which allow us to control the volume fractions of the phases. By using this convention, the total volume of the RVE is $V_{\text{RVE}} = (2a + b)^3$. We only use RVEs with the same total volume of $V_{\text{RVE}} = 1 \text{ mm}^3$, which is a suitable size for the microscale calculations [Ilić et al. (2010)], making it easy to compare different RVEs. Thus, the choice of a and b is restricted by $2a + b = 1 \text{ mm}$. The volume fraction of cortical bone for our RVE is $\rho_b = (6ab^2 + b^3)/(2a + b)^3$.

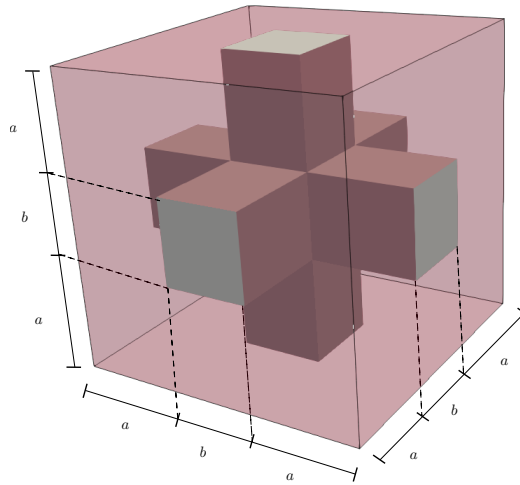


Figure 2.4: Periodic RVE with cortical bone phase (gray) and bone marrow phase (transparent red) and lengths parameters.

In our first example, we use a healthy bone RVE with the parameters $a = 0.32 \text{ mm}$ and $b = 0.36 \text{ mm}$, resulting in $\rho_b = 29.5\%$. We compare different mesh resolutions. The first RVE consists of two elements in each phase block, resulting in six elements for each spatial direction. The second RVE consists of four elements in each block, resulting in twelve elements for each spatial direction. Here, all degrees of freedom for all corner nodes are restricted to zero and all opposite nodes are linked, to guarantee periodicity. Figure 2.5 shows the results of the simulations.

Both simulations show quadratic convergence behavior and periodic results. For all quantities, the results between the two different used meshes look nearly identical confirming mesh independence of the results. This is not only fulfilled on the surface of the model, but

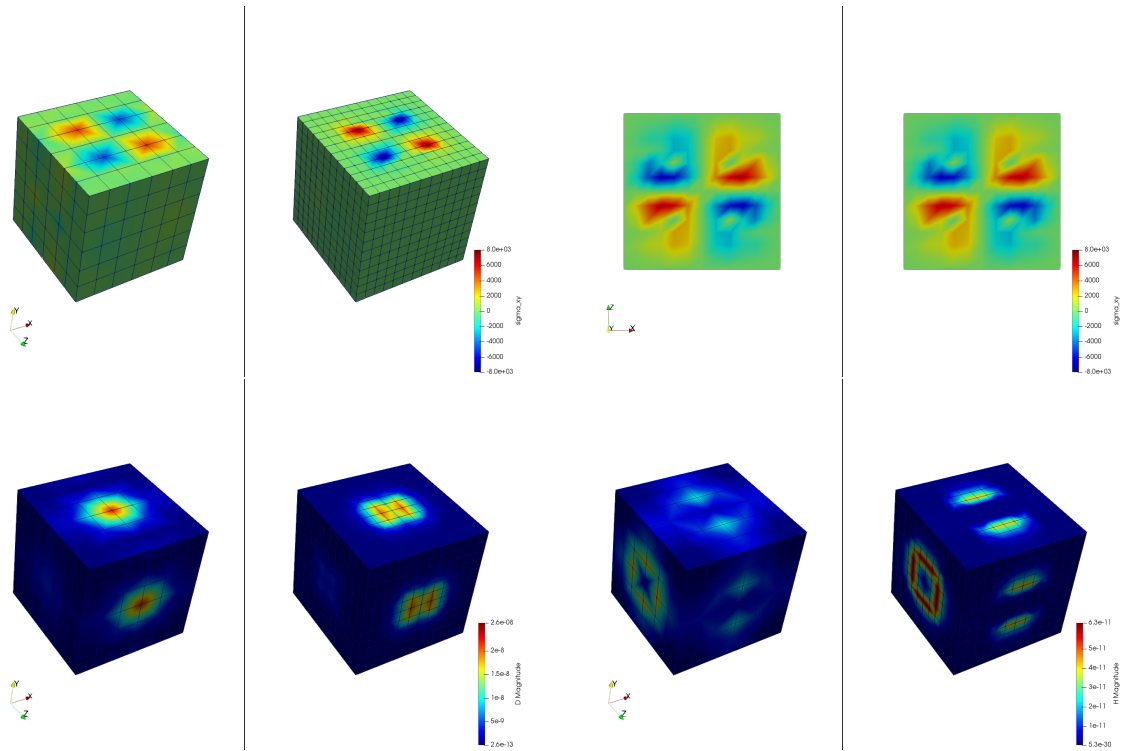


Figure 2.5: Microscale simulation results of a coarse and fine mesh (left and right respectively) for all flux quantities. Top left: mechanical stress σ_{xy} [GPa], top right: mechanical stress σ_{xy} [GPa] in the xz -plane with $y = 0$, bottom left: magnitude of the electric displacement field D [A s/m²], bottom right: magnitude of the magnetic field strength H [A/m].

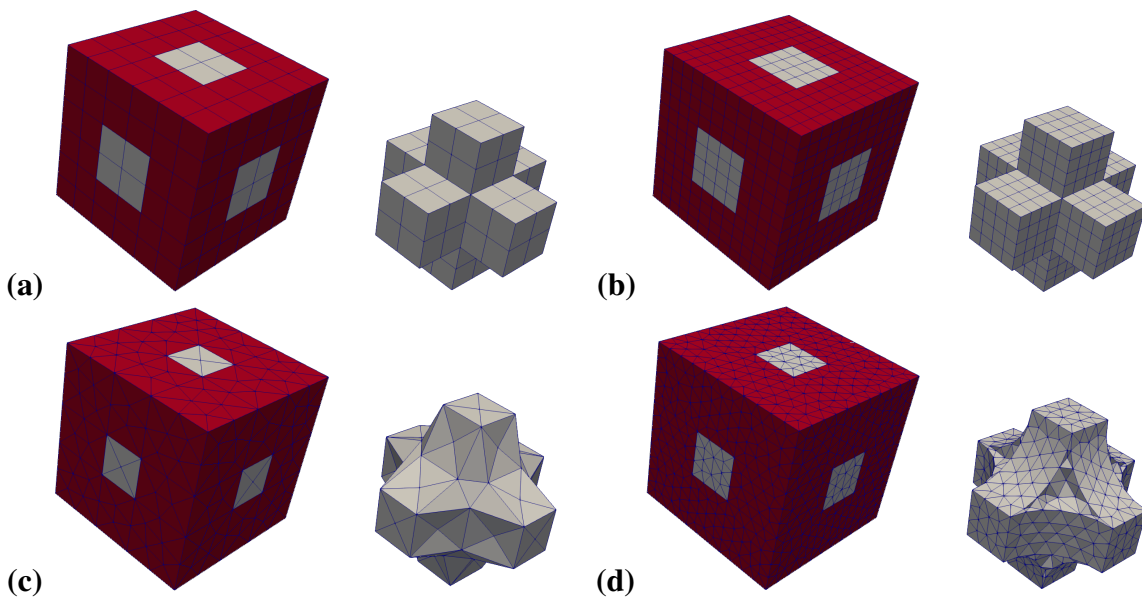


Figure 2.6: Used meshes for the complete RVE (left) and only the cortical bone phase (right). **a** coarse hexahedron mesh, **b** fine hexahedron mesh, **c** coarse tetrahedron mesh, **d** fine tetrahedron mesh.

also in the inner parts, as the slice (top right) shows. It should be noted that since the FE² method uses volume averaging, the coarse mesh with only six elements in each spatial direction is sufficient enough to create accurate results for the multiscale method and is mostly

used in the remaining examples of this paper.

The calculation of the magnetic field strength is susceptible for numerical errors. These errors can occur, when there are sharp edges in the mesh or between the phase transitions, which can amplify the results. To investigate this issue, we constructed smoother RVEs by using tetrahedron elements and different mesh resolutions. Figure 2.6 shows the used meshes. We found that despite the smoother approach, the numerical results of the RVEs with tetrahedron elements are much worse compared to the RVEs with hexahedron elements, showing worse convergence behavior and overestimating the magnetic field strength. One reason for this result could be that through the mesh refinement, many additional corners are introduced, which in total amplify the magnetic field strength more than a low number of very sharp corners. Moreover, smaller element size leads to amplified singularities of the corresponding fields at corners, which otherwise are regularized by the employed shape functions. Similarly, Figure 2.5 shows an increase in the magnetic field strength for the finer mesh resolution of the RVEs with hexahedron elements. In conclusion, the coarse RVE with hexahedron elements shows the best numerical performance despite the low mesh resolution and the included sharp edges.

no.	a [mm]	b [mm]	ρ_b
1	0.43	0.14	5.3%
2	0.40	0.20	10.4%
3	0.38	0.24	14.5%
4	0.36	0.28	19.1%
5	0.34	0.32	24.2%
6	0.32	0.36	29.5%

Table 2.3: Lengths parameter of the different RVEs.

To compare the model behavior for different stages of osteoporosis, we created RVEs with different volume fractions of cortical bone. Table 2.3 shows the choice of the lengths parameters and the resulting volume fractions. The macroscopic mechanical stiffness tensor $\bar{\mathbb{C}} := \frac{\partial \bar{\sigma}}{\partial \bar{\epsilon}}$ was now evaluated for all RVEs by applying a small numerical perturbation as discussed in Section 2.4.2. We then calculate the effective Young's modulus as

$$E_{\text{eff}} = \frac{\bar{\mathbb{C}}_{44}(3\bar{\mathbb{C}}_{12} + 2\bar{\mathbb{C}}_{44})}{(\bar{\mathbb{C}}_{12} + \bar{\mathbb{C}}_{44})}. \quad (2.49)$$

Figure 2.7 shows a plot of the macroscopic Young's modulus against the volume fraction of cortical bone. Here, we observe a drastical reduction of the macroscopic Young's modulus with decreasing cortical bone fraction. Compared to a healthy bone ($\rho_b = 29.5\%$), the effective Young's modulus of the degenerated bone ($\rho_b = 5.3\%$) decreases to 57% (from 3.89 GPa to 2.32 GPa). Similar results can be found in Ilić et al. (2010).

2.5.3 Cylinder model

In this section, we show results for a cylinder model, which has a length of 30 cm and a diameter of $2 r_o = 3$ cm. The mesh and the displacement boundary conditions are shown in Figure 2.8. The mesh consists of 1767 nodes and 1440 hexahedral elements. The left and right face is fixed, resulting in the boundary conditions $\mathbf{u} = \mathbf{0}$ on the faces. Additionally,

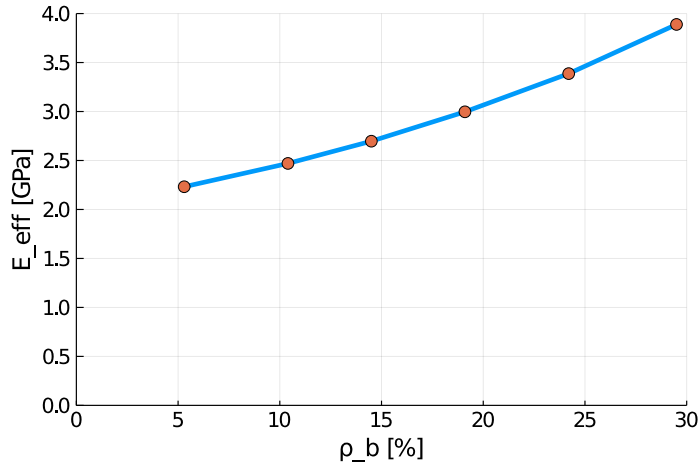


Figure 2.7: Effective Young's modulus E_{eff} against cortical bone volume fraction ρ_b for different RVEs.

in the inner part of the left face ($r < r_i = 0.75$ cm) depicted in Figure 2.9, the cylinder is assumed to be grounded, resulting in $\varphi = 0$ and $\mathbf{A} = \mathbf{0}$. We apply a time-dependent mechanical displacement in x-direction $u_x = u_{\text{max}} \cdot a(t)$ to the middle part of the cylinder and calculate 100 time steps. Figure 2.10 shows the amplitude of the displacement function a versus the time t .

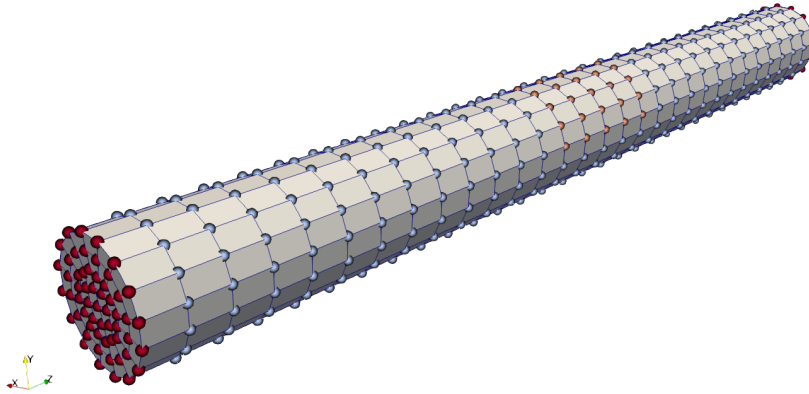


Figure 2.8: Cylinder mesh and displacement boundary conditions (red: all directions restricted, orange: only the x-direction restricted, blue-gray: no directions restricted).

First, we examine the simulation results for the healthy bone (RVE 6, $\rho_b = 29.5\%$). Here, we observe quadratic convergence behavior for the macroscale as well. Figures 2.11 and 2.12 show the magnitude of the average electric displacement field \mathbf{D} and the magnitude of the average magnetic field strength \mathbf{H} , respectively, plotted against time t . The history of the average electric displacement field mimics the displacement boundary condition. Thus, the electric displacement field is caused mainly by the piezoelectric effect of the cortical bone material phase. In contrast, the magnitude of the average magnetic field strength increases until time $t = 50$, where the maximum is reached. Then, the magnitude decreases again and at the end of the simulation, only a small amount of the magnetic field is present. We conclude, that the magnetic field is caused mainly by the time change of the electric displacement field as described by the Maxwell equations.

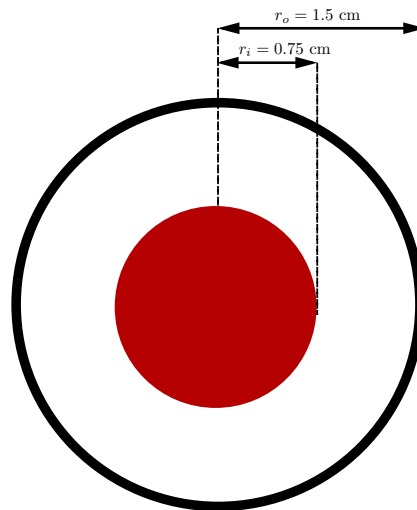


Figure 2.9: Cylinder front in the xy -plane for $z = 0$ with grounded nodes in red.

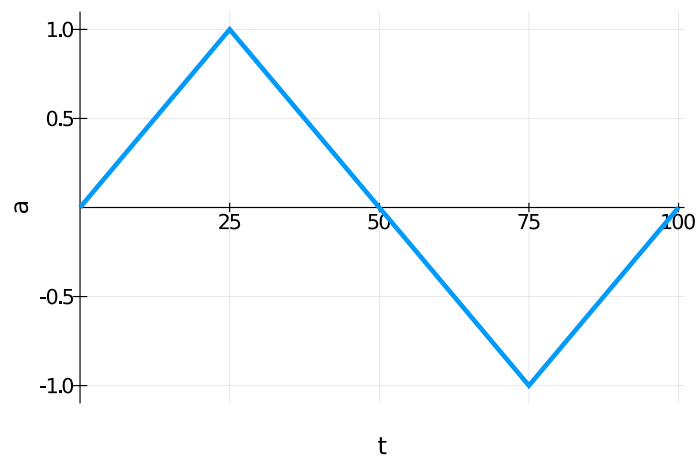


Figure 2.10: Amplitude of the displacement function a against the time step t .

To compare the different stages of osteoporosis, we use different RVEs (Table 2.3). The simulation results are shown in Figures 2.13 to 2.16. Here, the number of the specific RVE increases from top to bottom.

As an additional example for the cylinder model, we performed a parameter study for the electric conductivity parameter κ_1 , aiming to understand the interaction between the time derivative of the electric displacement field and the electric current density in the Maxwell equation. Figures 2.17 and 2.18 show the results for RVE 1 and $\kappa_1 \in \{1 \cdot 10^2 \text{ S/m}, 1 \cdot 10^4 \text{ S/m}, 1 \cdot 10^6 \text{ S/m}\}$.

For all quantities, we observe an increase for RVEs with higher volume fractions of cortical bone. Additionally, the difference between the RVEs is greater, the lower the volume fraction of cortical bone is. While the difference is barely noticeable between RVE 5 and 6, the change of all quantities excluding the stress is distinct between RVEs 1 and 2. Qualitatively, we notice similar results between the different RVEs.

Regarding the parameter study of the electric conductivity, we observe nearly identical results for the magnetic field strength \mathbf{H} for the first two choices of κ_1 , but a significant in-

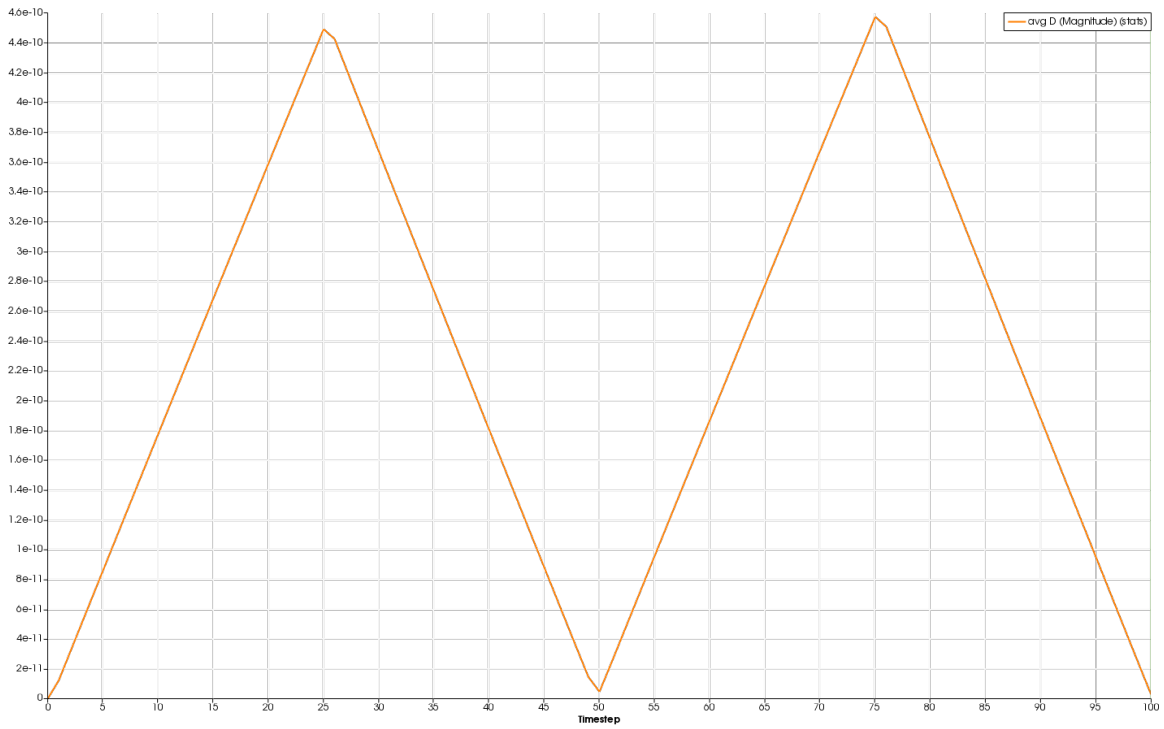


Figure 2.11: Magnitude of the average electric displacement field \mathbf{D} [As/m^2], plotted against the time t .

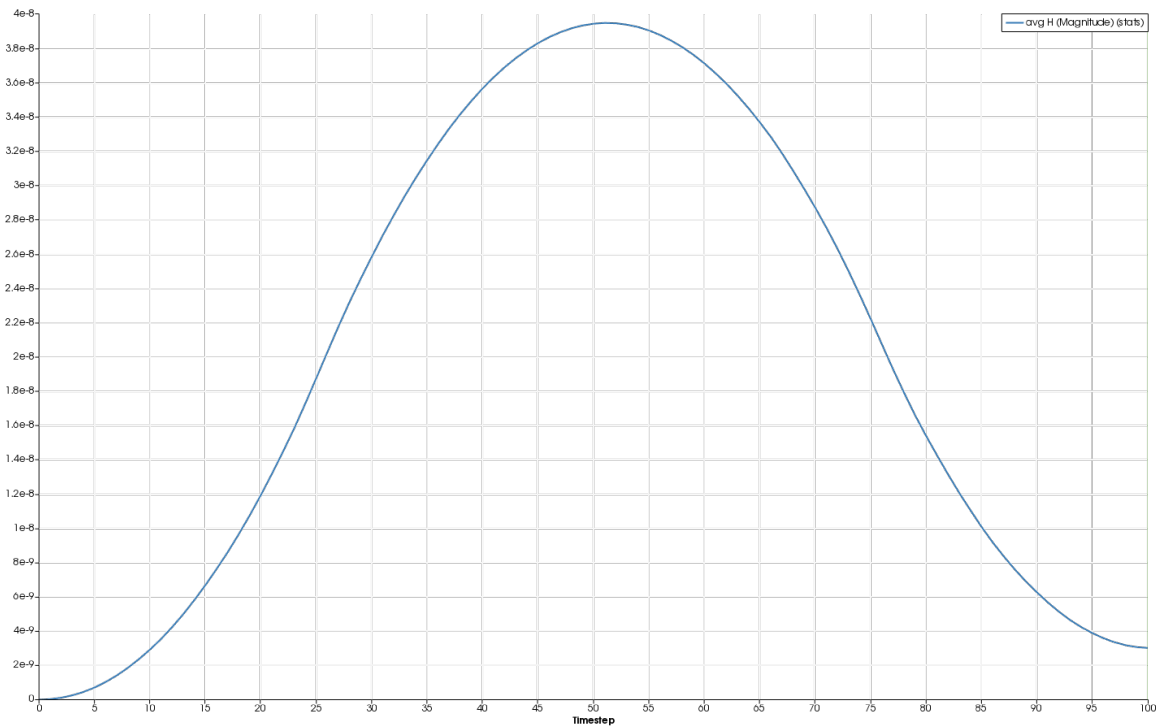


Figure 2.12: Magnitude of the average magnetic field strength \mathbf{H} [A/m], plotted against the time t .

crease for $\kappa_1 = 1 \cdot 10^6 \text{ S}/\text{m}$. Similarly the electric current density \mathbf{J} increases proportionally to the increase of the material parameter. Thus, for the first two choices of κ_1 , nearly no magnetic field and electric current is visible.

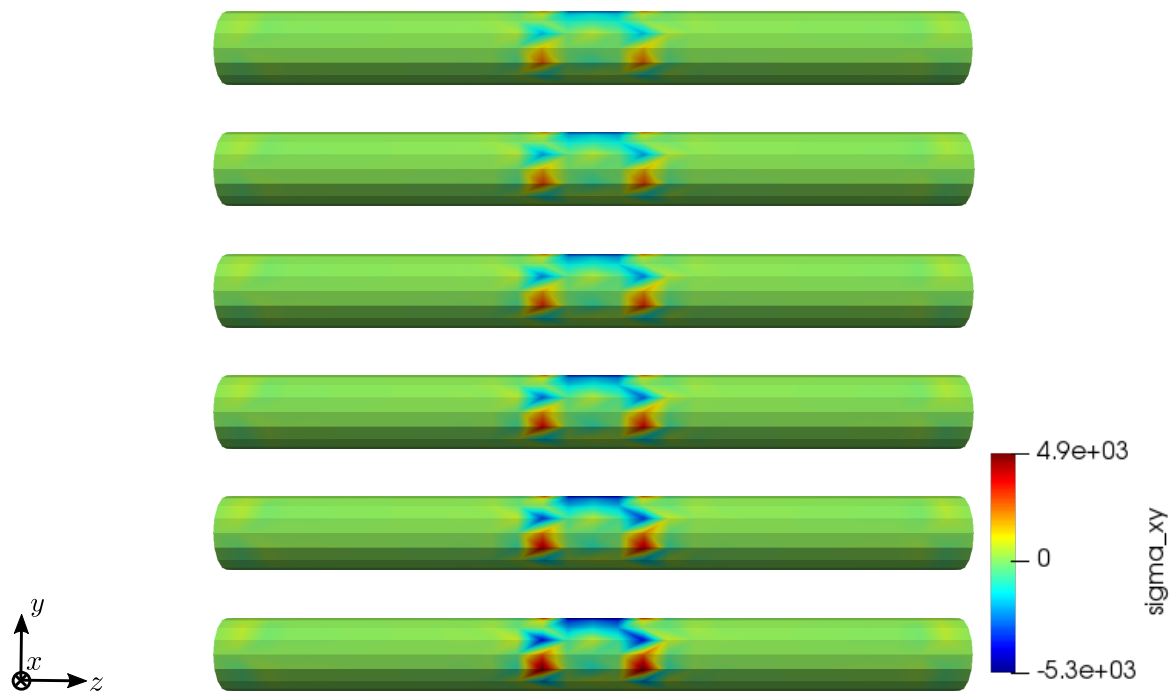


Figure 2.13: Simulation results for RVE 1 (top) to 6 (bottom): stress σ_{xy} [GPa], $t = 25$.

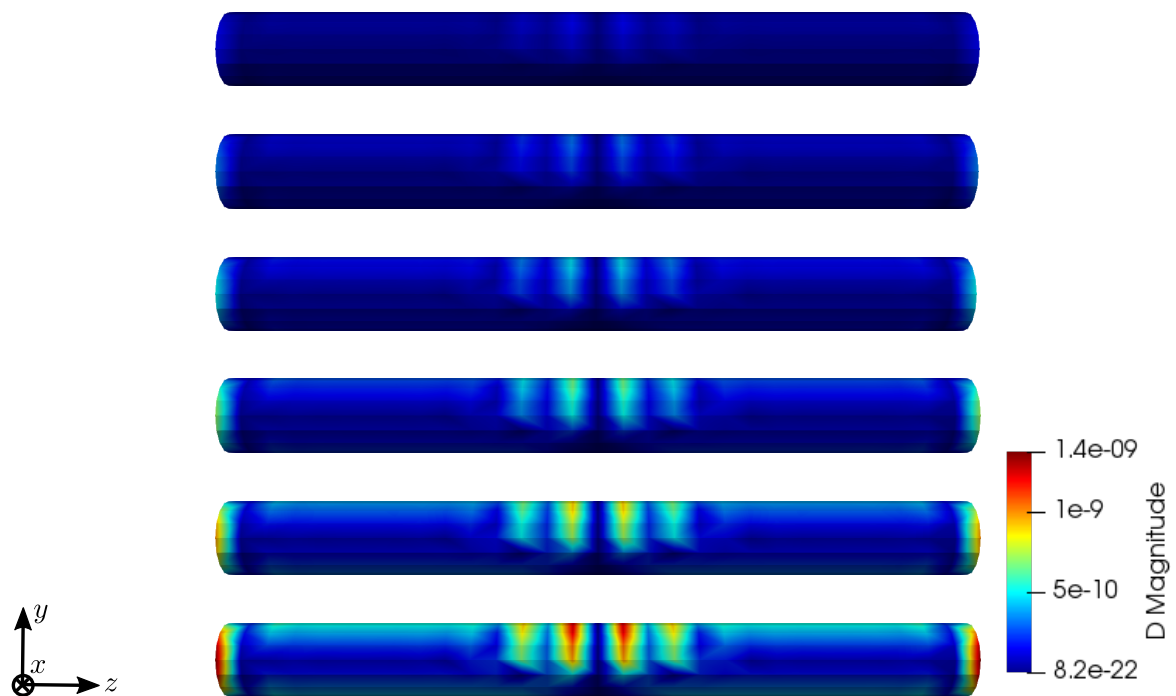


Figure 2.14: Simulation results for RVE 1 (top) to 6 (bottom): magnitude of the electric displacement field D [As/m²], $t = 25$.

Real bones can be highly anisotropic. To investigate possible effects on the simulation results, we constructed an anisotropic RVE, which is longer (Figure 2.19) and therefore also is divided into ten instead of six elements in z -direction. We used the parameters $a = 0.29$ mm and $b = 0.42$ mm, resulting in a total RVE volume $V_{\text{RVE}} = 1.58$ mm³ and a volume fraction of cortical bone $\rho_b = 30.6\%$. We compare our calculations to the isotropic RVE 6, which has a similar volume fraction of cortical bone. The results are shown in Figure

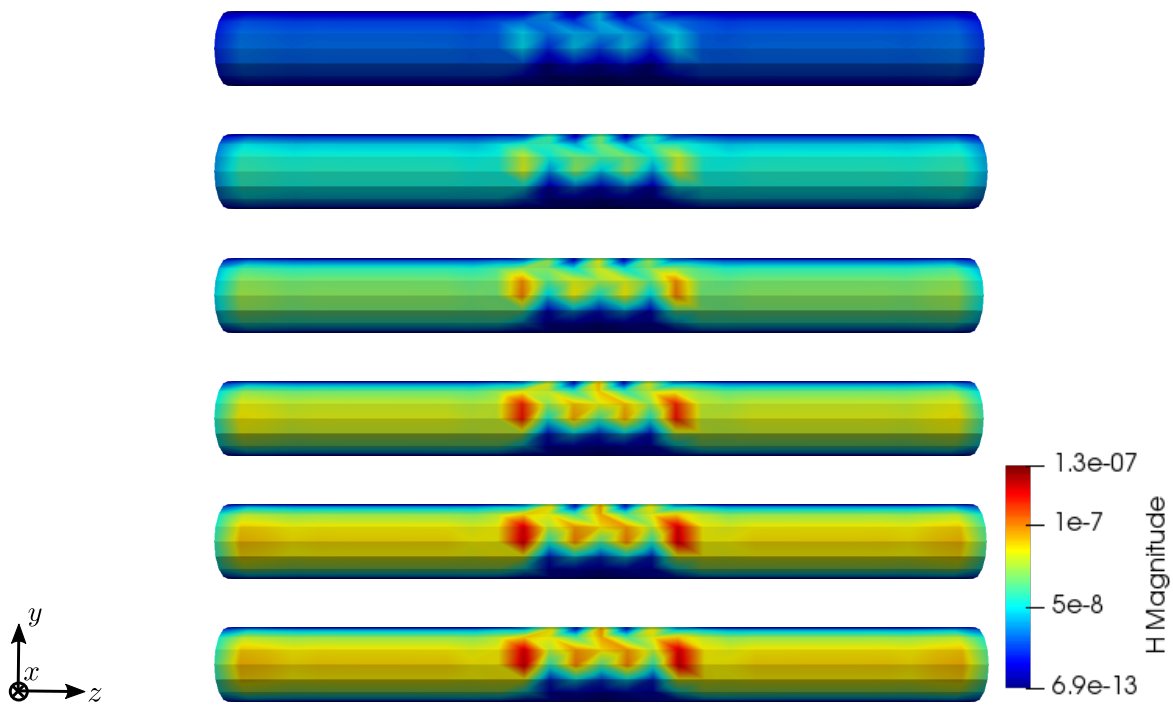


Figure 2.15: Simulation results for RVE 1 (top) to 6 (bottom): magnitude of the magnetic field strength \mathbf{H} [A/m], $t = 50$.

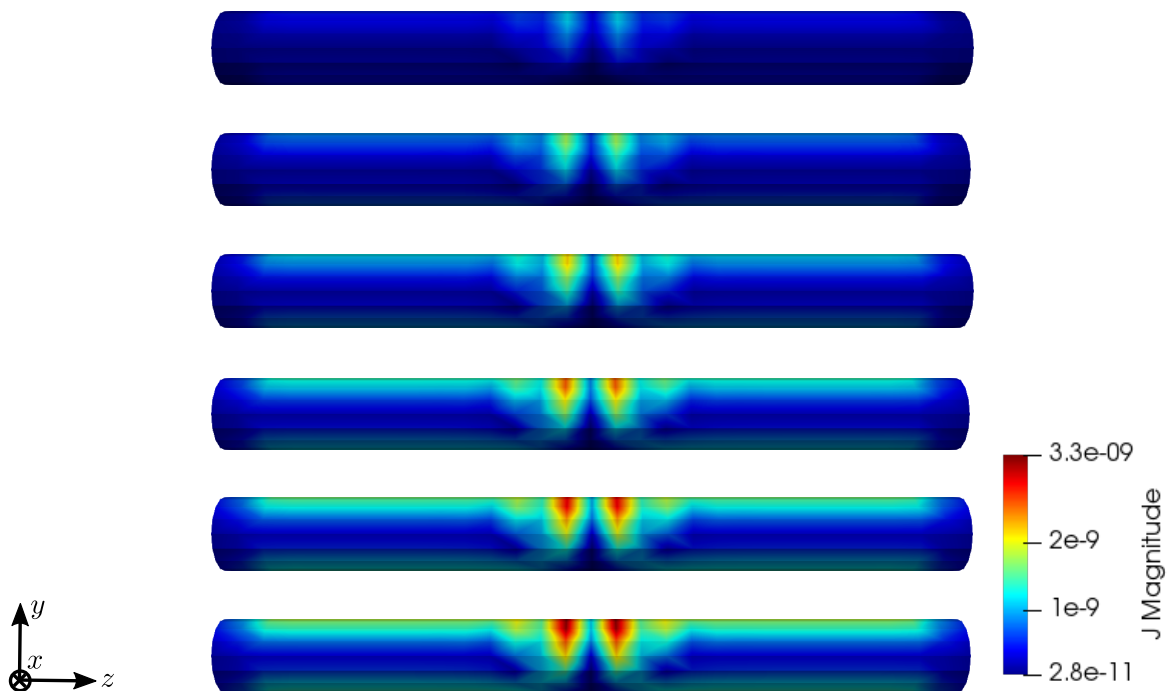


Figure 2.16: Simulation results for RVE 1 (top) to 6 (bottom): magnitude of the electric current density \mathbf{J} [A/m²], $t = 50$.

2.20 and 2.21. We obtain similar results for both RVE geometries. The calculated stress is slightly higher for the anisotropic RVE. The magnetic field strength is about 15% increased for the anisotropic RVE compared to the cubic RVE.

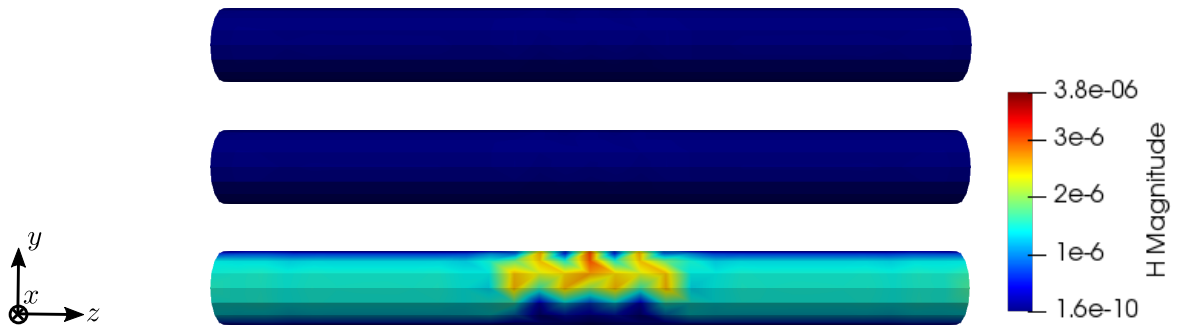


Figure 2.17: Simulation results for RVE 1 for the magnetic field strength \mathbf{H} [A/m] with $\kappa_1 = 1 \cdot 10^2$ S/m (top), $\kappa_1 = 1 \cdot 10^4$ S/m (in the middle) and $\kappa_1 = 1 \cdot 10^6$ S/m (bottom), $t = 50$.



Figure 2.18: Simulation results for RVE 1 for the electric current density \mathbf{J} [A/m²] with $\kappa_1 = 1 \cdot 10^2$ S/m (top), $\kappa_1 = 1 \cdot 10^4$ S/m (in the middle) and $\kappa_1 = 1 \cdot 10^6$ S/m (bottom), $t = 50$.

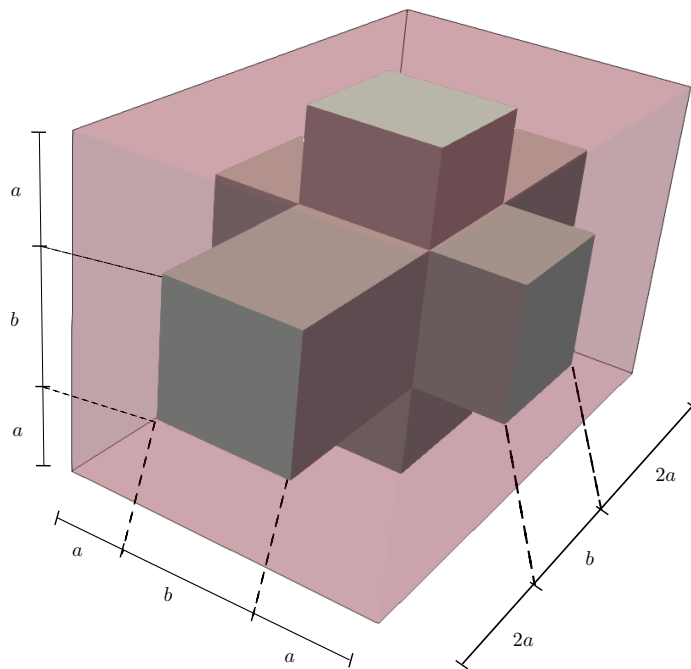


Figure 2.19: Anisotropic RVE with cortical bone phase (gray) and bone marrow phase (transparent red) and lengths parameters.

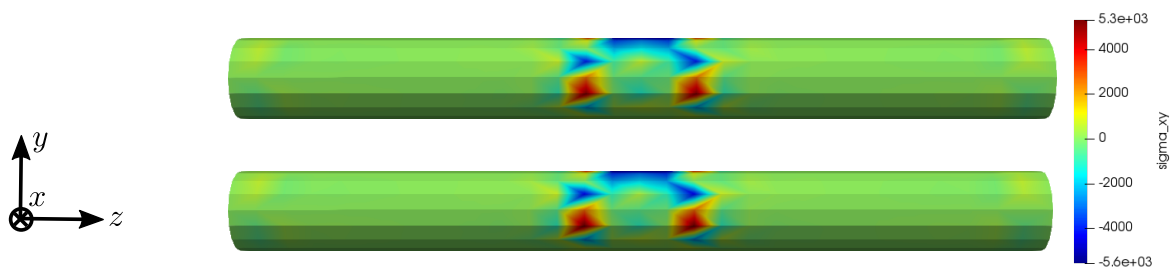


Figure 2.20: Simulation results for RVE 6 (top) and the anisotropic RVE (bottom) for the stress σ_{xy} [GPa], $t = 25$.

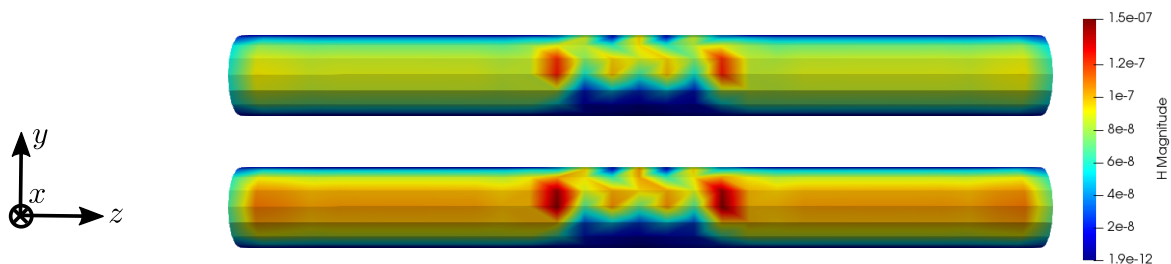


Figure 2.21: Simulation results for RVE 6 (top) and the anisotropic RVE (bottom) for the magnetic field strength \mathbf{H} [A/m], $t = 50$.

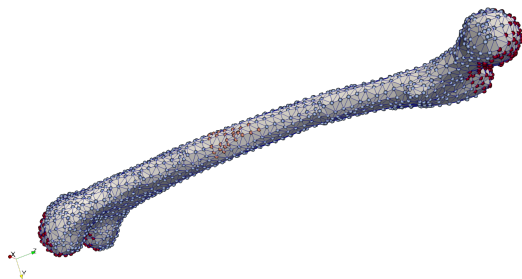


Figure 2.22: Femur bone mesh and displacement boundary conditions (red: all directions restricted, orange: only the x-direction restricted, blue-gray: no directions restricted).

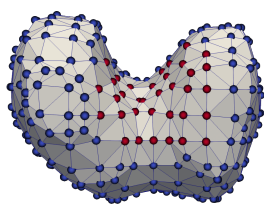


Figure 2.23: Femur bone front with grounded nodes in red.

2.5.4 True to scale bone model

We examine a true to scale model of a human femur bone from Lifescience Database (2022) and slightly modify it by using the software BLENDER [Blender Foundation (2021)], improving the mesh. Again the model has a length of about 30 cm. The mesh and the displacement boundary conditions are shown in Figure 2.22. The mesh consists of 1660 nodes and 4944 tetrahedral elements. The grounded nodes are shown in Figure 2.23. Again, we

apply the mechanical displacement depicted in Figure 2.10 to the middle section and calculate 100 time steps. To compare different stages of osteoporosis, we use again different RVEs (Table 2.3). Figures 2.24 to 2.29 show the results.

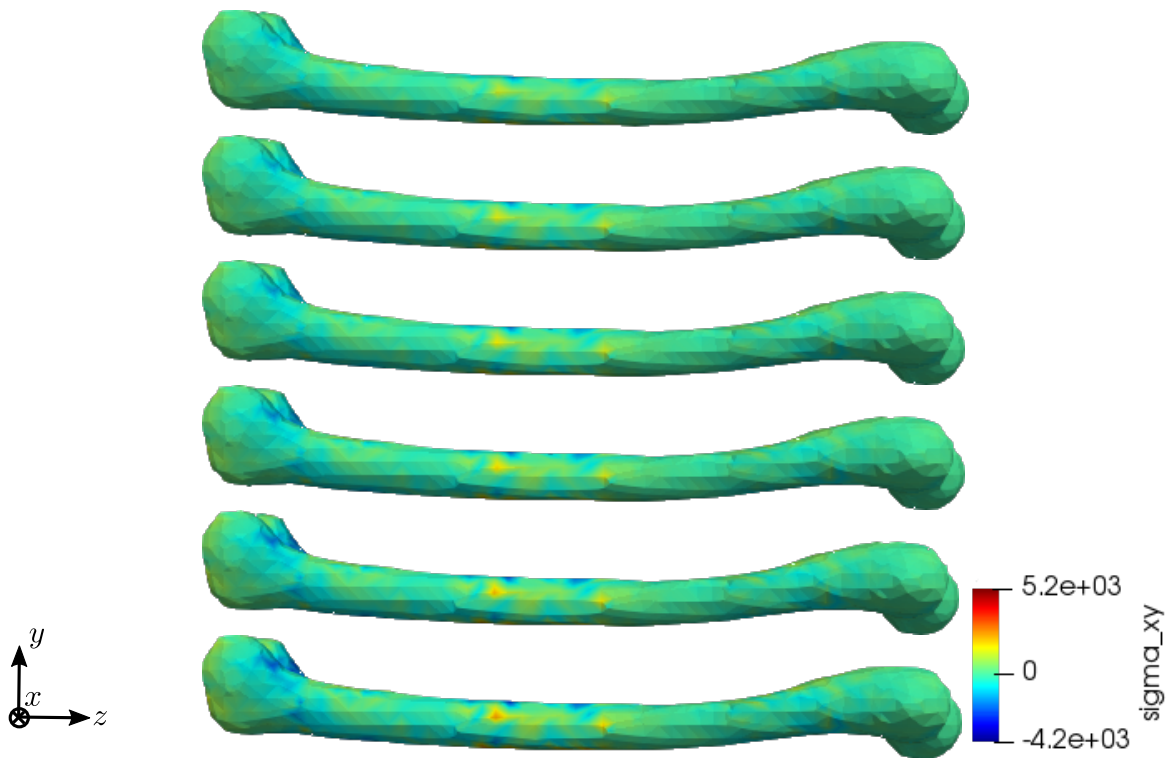


Figure 2.24: Simulation results for RVE 1 (top) to 6 (bottom): stress σ_{xy} [GPa], $t = 25$.

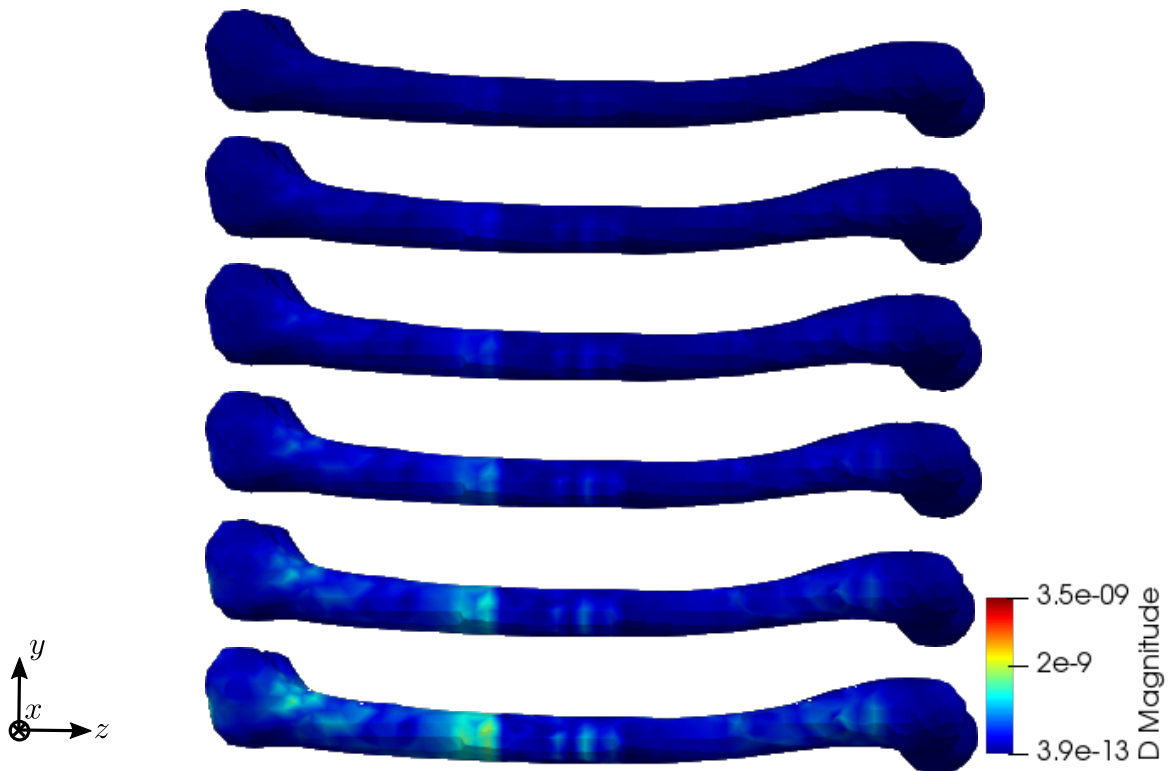


Figure 2.25: Simulation results for RVE 1 (top) to 6 (bottom): magnitude of the electric displacement field D [As/m²], $t = 25$.

Again, the simulations show qualitatively similar results, but a significant increase for all

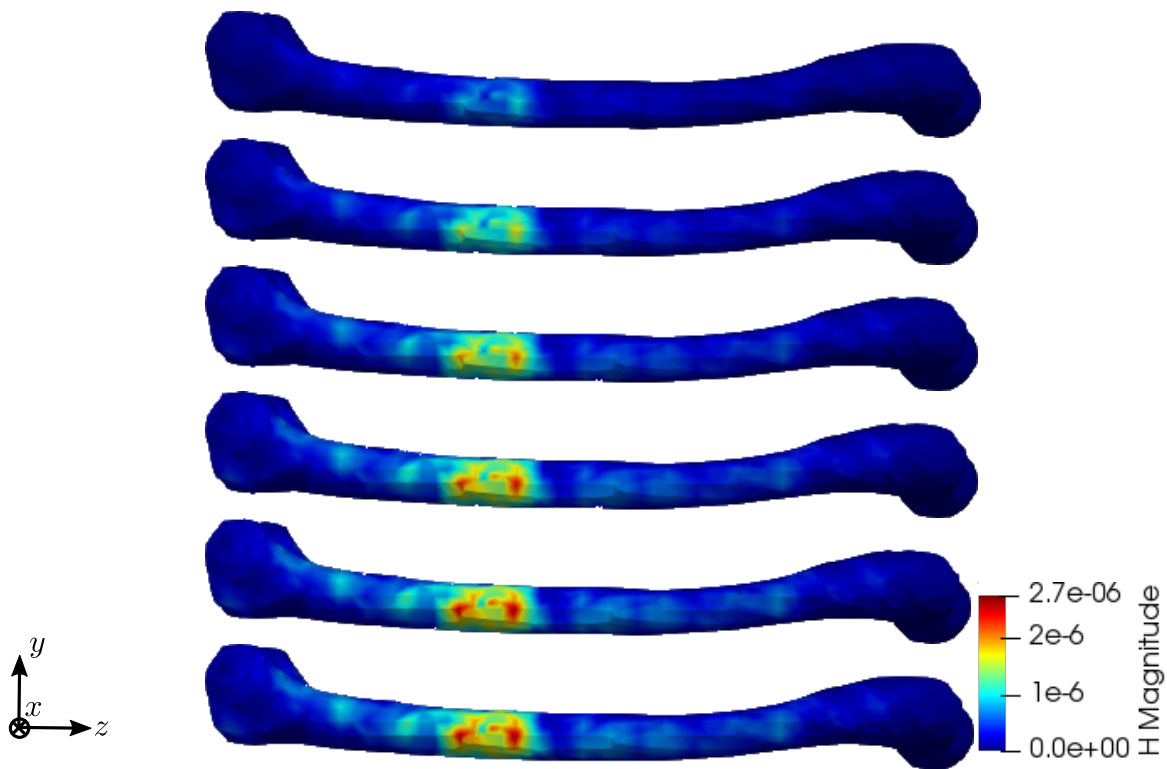


Figure 2.26: Simulation results for RVE 1 (top) to 6 (bottom): magnitude of the magnetic field strength \mathbf{H} [A/m], $t = 50$.

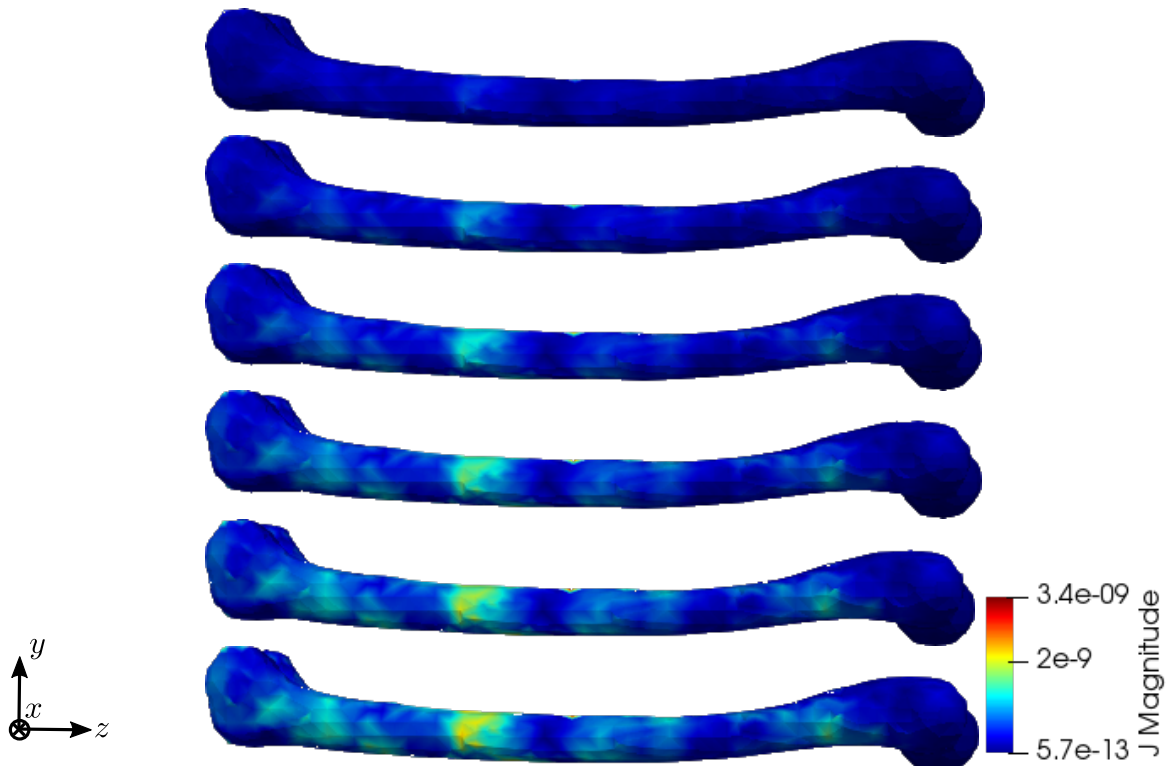


Figure 2.27: Simulation results for RVE 1 (top) to 6 (bottom): magnitude of the electric current density \mathbf{J} [A/m²], $t = 50$.

quantities the higher the cortical bone volume fraction is. Compared to the cylinder model, we receive slightly higher numerical values, which lie in the same magnitudes. The reason

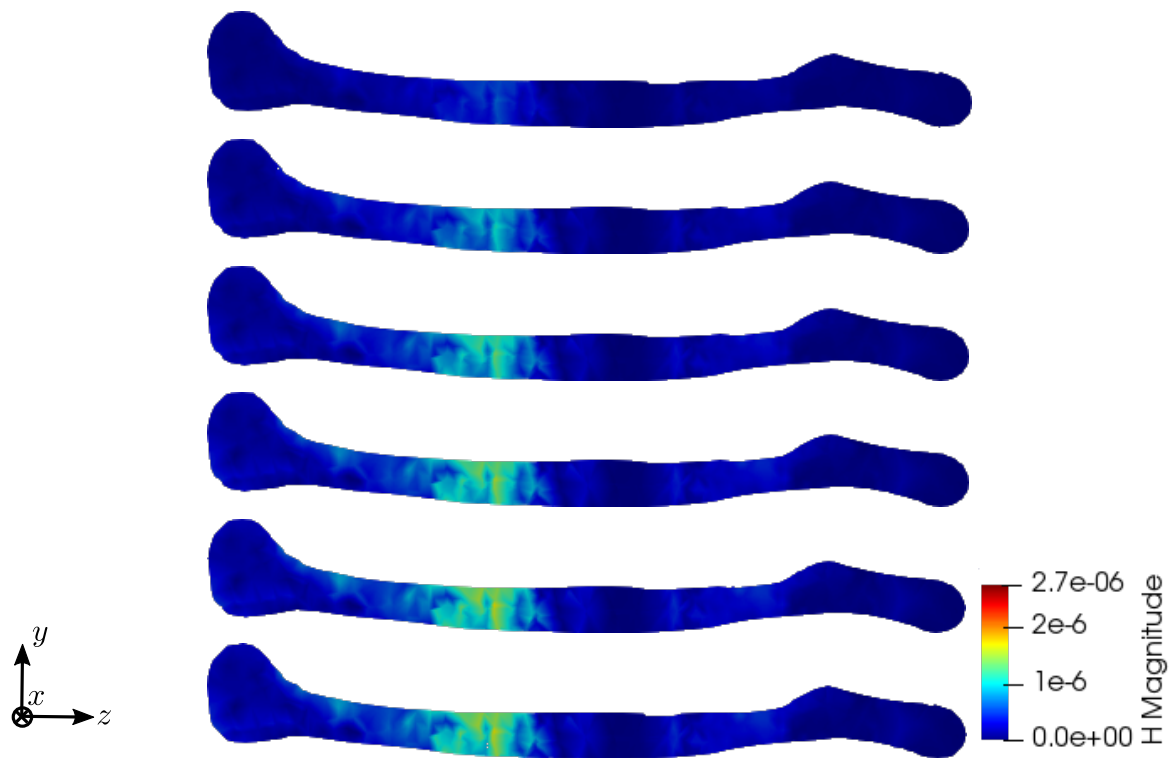


Figure 2.28: Simulation results for RVE 1 (top) to 6 (bottom): magnitude of the magnetic field strength \mathbf{H} [A/m], slice, $t = 50$.

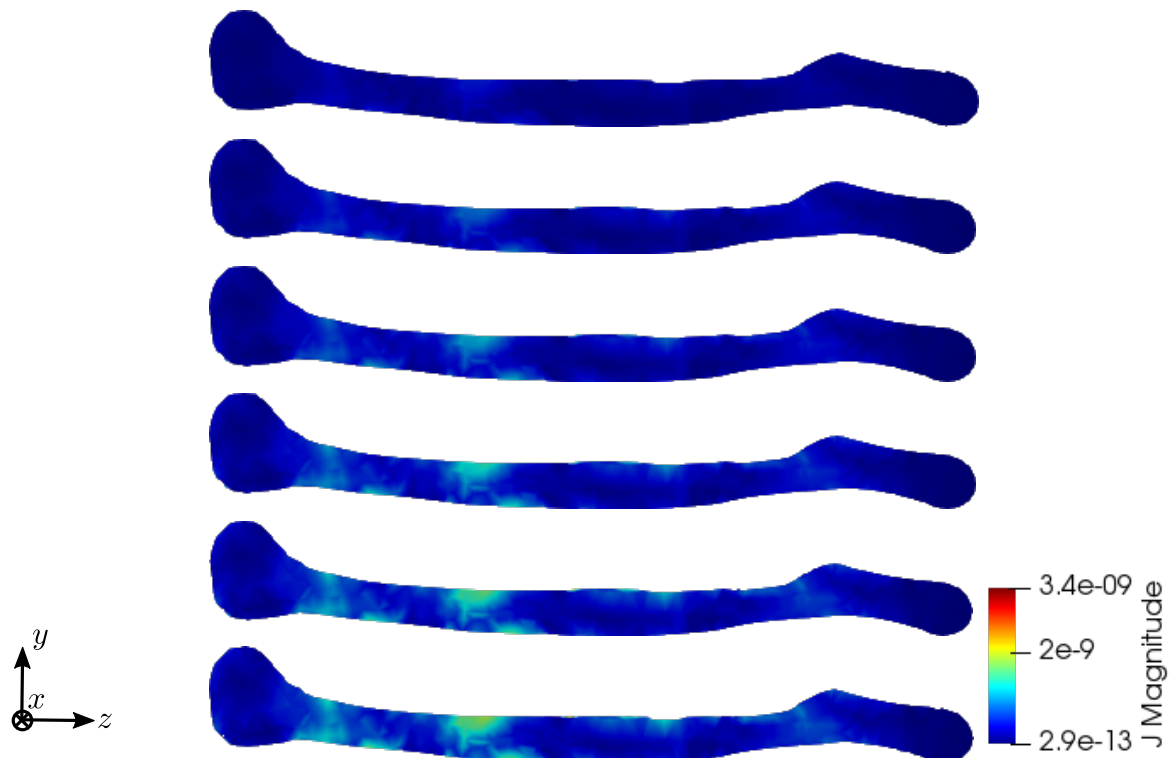


Figure 2.29: Simulation results for RVE 1 (top) to 6 (bottom): magnitude of the electric current density \mathbf{J} [A/m²], slice, $t = 50$.

for this is most likely the used mesh, which has sharper corners due to the geometry of bone. Additionally, tetrahedron elements usually perform worse compared to hexahedron elements. The difference between the RVEs is smaller the higher the volume fraction of

cortical bone is. Thus, both the functionality of the bone and the results of the sonography are only slightly affected at earlier stages of osteoporosis, but significantly at later ones. This confirms the disease as being often imperceptible for many subjects at earlier stages. This is especially important regarding the magnetic field strength \mathbf{H} , as it is the quantity measured at sonography-aided early detection. To further examine the results, we calculate the average and maximum magnetic field strength \mathbf{H} at time step $t = 50$ for the different RVEs. The results are shown in Figures 2.30 and 2.31.

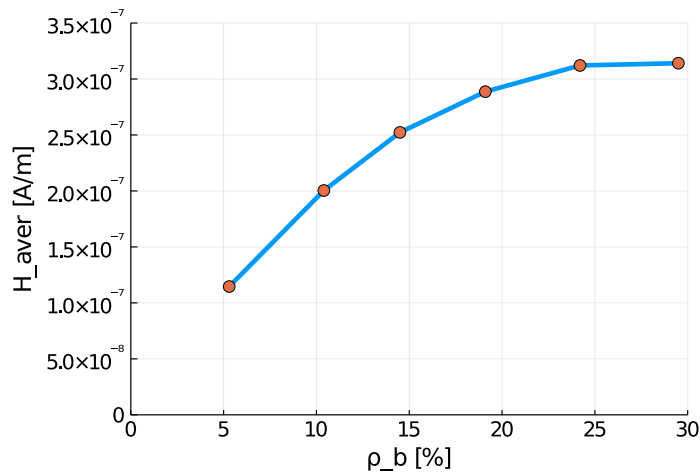


Figure 2.30: Average magnetic field strength for the different RVEs at $t = 50$.

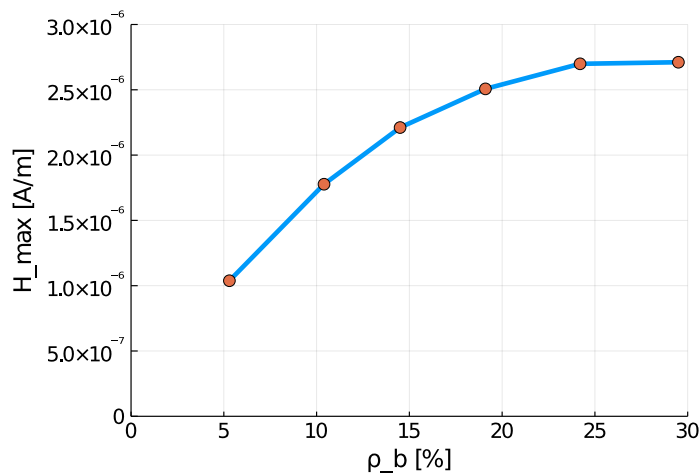


Figure 2.31: Maximum magnetic field strength for the different RVEs at $t = 50$.

Here, for both quantities a similar behavior can be observed. While there is nearly no reduction between the two RVEs with the highest volume fraction of cortical bone, the difference between the single RVEs increases for lower volume fractions of cortical bone. The average magnetic field strength reduces for the ill bone ($\rho_b = 5.3\%$) to 36.5% compared to the healthy bone ($\rho_b = 29.5\%$), from $3.14 \cdot 10^{-7}$ A/m to $1.15 \cdot 10^{-7}$ A/m. The maximum magnetic field strength for the healthy bone is $2.711 \cdot 10^{-6}$ A/m, while the maximum for the degenerated bone is only $1.038 \cdot 10^{-6}$ A/m. This equals a reduction to 38.2%. These results show the order of magnitude to be expected for the results of experimental research. For advanced stages of osteoporosis, sonography should measure a magnetic field strength, whose magnitude is only about one third compared to a healthy bone.

2.6 Conclusion and outlook

In this contribution, we present a fully coupled multiscale model for cancellous bone considering mechanical, electric and magnetic effects. We model bone as a two-phase material with the cortical bone phase assumed as a piezoelectric, insulating solid and the bone marrow phase described as a viscoelastic, conducting solid. Electric and magnetic effects are coupled via the Maxwell equations. Based on energy methods in mechanics, we establish a thermodynamically consistent material model and derive the weak and strong form of the microscale boundary value problem.

In order to solve the macroscale problem, we create an RVE and apply the FEM to solve the problem numerically. For the time integration of the FEM, we use a JWH- α -scheme [Kadapa et al. (2017)]. The numerical simulations on the microscale show mesh independence and quadratic convergence. For finer mesh resolutions or smoother geometries of the phases, the model tends to overestimate the magnetic field strength. Additionally, we show that the effective Young's modulus of the RVE depends strongly on the volume fraction of the different phases. Here, we find a reduction by 43% for the degenerated bone ($\rho_b = 5.3\%$) compared to the healthy bone ($\rho_b = 29.5\%$), achieving similar results as in Ilić et al. (2010).

For the multiscale calculations, we use FE² and apply periodic boundary conditions and volume averaging for the transition between the scales. We apply a time-dependent displacement boundary condition. The macroscopic cylinder model again shows quadratic convergence. To compare different stages of osteoporosis with a healthy bone, we create six different RVEs with different volume fractions of cortical bone phase and run calculations for all RVEs. The simulations show a strong reduction of all quantities with decreasing volume fraction of cortical bone phase. The differences between the healthy bone RVE ($\rho_b = 29.5\%$) and a slightly degenerated bone ($\rho_b = 24.2\%$) are very small, while the differences in the later stages of the illness, ($\rho_b = 10.4\%$ compared to $\rho_b = 5.3\%$), increase drastically. To examine the interaction between the time derivative of the electric displacement field and the electric current density in the Maxwell equation, we perform a parameter study regarding the electric conductivity parameter κ_1 . Here, the results show a significant increase of the electric current density and the magnetic field strength with increasing κ_1 . To investigate the effect of anisotropy on the model, we compared our cubic RVE with an anisotropic cuboid RVE. Depending on the used RVE geometry, the results can vary slightly.

As a final example, we apply our model to a true to scale model of a human femur bone. Here, the results show again a similar behavior for all quantities. Between the two RVEs with the highest volume fraction of cortical bone phase, nearly no reduction of the magnetic field strength can be observed. With decreasing ρ_b , the differences grow increasingly larger. Compared to the healthy bone ($\rho_b = 29.5\%$), the bone with late stage osteoporosis ($\rho_b = 5.3\%$) shows a drastic reduction of the magnetic field strength by nearly two thirds. These results show, in which order of magnitude differences between healthy and degenerated bones can be expected, when performing experimental research and sonography for the purpose of early detection of osteoporosis.

For future research, we aim to solve the inverse problem by using an Artificial Neural Network to predict simulation outputs for random microstructures. Here, the network should recover the distribution of cortical bone phase in the macroscopic model from the magnetic field data, thus diagnosing the state of the bone. Additionally, wave propagation in

cancellous bone will be investigated in more detail. The comparison of experimental with simulation results could provide further insights. Accurate material parameters could be obtained from the experiments, which then could be used for the simulations. To make precise predictions for experimental setups, it is of great importance to address possible numerical problems of the simulations. The used RVEs have a very coarse mesh resolution and contain sharp edges. While our investigations so far show, that the coarse RVE with hexahedron elements performs best, it is still relevant to investigate in detail how the magnetic field strength is affected for different, smoother RVEs, which model the microstructure of bone in a more realistic way. Another important aspect is to investigate the microscale behavior for RVEs which differ in size and structure of the phases. Depending on the geometry of the used RVE, the simulation results can vary. Thus, for the future we plan to investigate this effect in detail. The usage of different function spaces could improve the results. Finally, our macroscopic models could be extended to include a surrounding medium like air or water, allowing proper decay of the magnetic field.

2.7 Appendix A: Calculation of the strong form for the micro problem

To calculate the strong form of the problem, we use the reduced weak form:

$$\int_{\Omega} (\boldsymbol{\sigma} \cdot \delta \boldsymbol{\varepsilon} - \mathbf{D} \cdot \delta \mathbf{E} + \mathbf{H} \cdot \delta \mathbf{B} - \mathbf{J} \cdot \delta \mathbf{A} + \gamma (\nabla \cdot \mathbf{A}) \cdot \delta (\nabla \cdot \mathbf{A})) dV - \delta W_{\text{ext}} = 0 \quad \forall \delta \mathbf{u}, \delta \varphi, \delta \mathbf{A}. \quad (2.50)$$

Now, we apply partial integration to each term followed by the use of a surface-volume integral rule:

$$\begin{aligned} \int_{\Omega} \boldsymbol{\sigma} \cdot \delta \boldsymbol{\varepsilon} dV &= \int_{\Omega} \nabla \cdot (\boldsymbol{\sigma} \cdot \delta \mathbf{u}) dV - \int_{\Omega} (\nabla \cdot \boldsymbol{\sigma}) \cdot \delta \mathbf{u} dV \\ &= \int_{\partial \Omega} \boldsymbol{\sigma} \cdot \mathbf{n} \cdot \delta \mathbf{u} dA - \int_{\Omega} (\nabla \cdot \boldsymbol{\sigma}) \cdot \delta \mathbf{u} dV, \end{aligned} \quad (2.51)$$

$$\begin{aligned} \int_{t_0}^{t_1} \int_{\Omega} -\mathbf{D} \cdot \delta \mathbf{E} dV dt &= \int_{t_0}^{t_1} \int_{\Omega} (\mathbf{D} \cdot \delta (\nabla \varphi) + \mathbf{D} \cdot \delta \dot{\mathbf{A}}) dV dt \\ &= \int_{t_0}^{t_1} \int_{\Omega} \nabla \cdot (\mathbf{D} \delta \varphi) dV dt - \int_{t_0}^{t_1} \int_{\Omega} (\nabla \cdot \mathbf{D}) \delta \varphi dV dt \\ &\quad - \int_{t_0}^{t_1} \int_{\Omega} \dot{\mathbf{D}} \cdot \delta \mathbf{A} dV dt + \underbrace{\int_{\Omega} [\mathbf{D} \cdot \delta \mathbf{A}]_{t_0}^{t_1} dV}_{=0} \\ &= \int_{t_0}^{t_1} \int_{\partial \Omega} \mathbf{D} \cdot \mathbf{n} \delta \varphi dA dt - \int_{t_0}^{t_1} \int_{\Omega} (\nabla \cdot \mathbf{D}) \delta \varphi dV dt - \int_{t_0}^{t_1} \int_{\Omega} \dot{\mathbf{D}} \cdot \delta \mathbf{A} dV dt, \end{aligned} \quad (2.52)$$

$$\begin{aligned}
\int_{\Omega} \mathbf{H} \cdot \delta \mathbf{B} \, dV &= \int_{\Omega} \nabla \cdot (\delta \mathbf{A} \times \mathbf{H}) \, dV + \int_{\Omega} \nabla \times \mathbf{H} \cdot \delta \mathbf{A} \, dV \\
&= \int_{\partial \Omega} \mathbf{H} \times \mathbf{n} \cdot \delta \mathbf{A} \, dA + \int_{\Omega} \nabla \times \mathbf{H} \cdot \delta \mathbf{A} \, dV,
\end{aligned} \tag{2.53}$$

$$\begin{aligned}
&\int_{\Omega} \gamma (\nabla \cdot \mathbf{A}) \cdot \delta (\nabla \cdot \mathbf{A}) \, dV \\
&= \int_{\Omega} \gamma \nabla \cdot ((\nabla \cdot \mathbf{A}) \cdot \delta \mathbf{A}) \, dV - \int_{\Omega} \gamma \nabla (\nabla \cdot \mathbf{A}) \delta \mathbf{A} \, dV \\
&= \int_{\partial \Omega} \gamma (\nabla \cdot \mathbf{A}) \cdot \mathbf{n} \cdot \delta \mathbf{A} \, dA - \int_{\Omega} \gamma \nabla (\nabla \cdot \mathbf{A}) \delta \mathbf{A} \, dV.
\end{aligned} \tag{2.54}$$

Here, \mathbf{n} is the normal vector pointing outwards. It should be noted that the term $\mathbf{D} \cdot \delta \mathbf{A}$ in Eq. (2.52) vanishes, as the test function $\delta \mathbf{A}$ does not change between the time t_0 and t_1 . For the magnetic energy variation Eq. (2.53), the sign is different compared to the other equations because of the cross product rule. Additionally, the resulting triple product in the surface integral allows cyclic permutation without changing the result. Inserting these identities in the reduced weak form Eq. (2.50) yields

$$\begin{aligned}
&\int_{\Omega} (-\nabla \cdot \boldsymbol{\sigma} - \mathbf{f}) \cdot \delta \mathbf{u} \, dV + \int_{\partial \Omega} (\boldsymbol{\sigma} \cdot \mathbf{n} - \mathbf{t}) \cdot \delta \mathbf{u} \, dA \\
&+ \int_{\Omega} (-\nabla \cdot \mathbf{D} + q_v) \cdot \delta \varphi \, dV + \int_{\partial \Omega} (\mathbf{D} \cdot \mathbf{n} + q_s) \cdot \delta \varphi \, dA \\
&\quad + \int_{\Omega} (\nabla \times \mathbf{H} - \dot{\mathbf{D}} - \mathbf{J} - \gamma \nabla (\nabla \cdot \mathbf{A}) - \mathbf{j}_v) \cdot \delta \mathbf{A} \, dV \\
&+ \int_{\partial \Omega} (\mathbf{H} \times \mathbf{n} - \mathbf{j}_s + \gamma (\nabla \cdot \mathbf{A}) \cdot \mathbf{n}) \cdot \delta \mathbf{A} \, dA = 0 \quad \forall \delta \mathbf{u}, \delta \varphi, \delta \mathbf{A}.
\end{aligned} \tag{2.55}$$

Then, we calculate the strong form by using the arbitrariness of the test functions and by splitting the volume and surface of the area, resulting in Eq. (2.21) and the matching conditions Eq. (2.22)⁵.

⁵Corrected the references to match with the correct equations, cf. Blaszczyk and Hackl (2022).

2.8 Appendix B: Derivation of the matrix form for the FEM

Inserting the FEM ansatz into the reduced weak form of the micro problem Eq. (2.50) yields

$$\begin{aligned}
& \int_{\Omega_b} \left((\mathbf{C}_b \mathbf{B}_u \hat{\mathbf{u}} - \mathbf{e}_b^T [-\mathbf{B}_{\text{grad}} \hat{\varphi} - \mathbf{N}_A \dot{\hat{\mathbf{A}}}]) \mathbf{B}_u \delta \hat{\mathbf{u}} - [\mathbf{e}_b \mathbf{B}_u \hat{\mathbf{u}} + \boldsymbol{\xi}_b (-\mathbf{B}_{\text{grad}} \hat{\varphi} - \mathbf{N}_A \dot{\hat{\mathbf{A}}})] \right. \\
& \quad \left. [-\mathbf{B}_{\text{grad}} \delta \hat{\varphi} - \mathbf{N}_A \delta \dot{\hat{\mathbf{A}}}] + \mu_b^{-1} \mathbf{B}_{\text{curl}} \hat{\mathbf{A}} \mathbf{B}_{\text{curl}} \delta \hat{\mathbf{A}} + \gamma \mathbf{B}_{\text{div}} \mathbf{B}_{\text{div}}^T \delta \hat{\mathbf{A}} \right) dV \\
& + \int_{\Omega_m} \left(\boldsymbol{\sigma}_m \mathbf{B}_u \delta \hat{\mathbf{u}} - [\boldsymbol{\xi}_m (-\mathbf{B}_{\text{grad}} \hat{\varphi} - \mathbf{N}_A \dot{\hat{\mathbf{A}}})] [-\mathbf{B}_{\text{grad}} \delta \hat{\varphi} - \mathbf{N}_A \delta \dot{\hat{\mathbf{A}}}] \right. \\
& \quad \left. + \mu_m^{-1} \mathbf{B}_{\text{curl}} \hat{\mathbf{A}} \mathbf{B}_{\text{curl}} \delta \hat{\mathbf{A}} + \gamma \mathbf{B}_{\text{div}} \mathbf{B}_{\text{div}}^T \delta \hat{\mathbf{A}} - \boldsymbol{\kappa}_m [-\mathbf{B}_{\text{grad}} \hat{\varphi} - \mathbf{N}_A \dot{\hat{\mathbf{A}}}] \mathbf{N}_A \delta \hat{\mathbf{A}} \right) dV \\
& - \left(\int_{\Omega} \mathbf{N}_u^T \mathbf{f} dV + \int_{\partial\Omega} \mathbf{N}_u^T \mathbf{t} dA \right) \delta \hat{\mathbf{u}} + \left(\int_{\Omega} \mathbf{N}_{\varphi}^T q_v dV + \int_{\partial\Omega} \mathbf{N}_{\varphi}^T q_s dA \right) \delta \hat{\varphi} \\
& - \left(\int_{\Omega} \mathbf{N}_A^T \mathbf{j}_v dV + \int_{\partial\Omega} \mathbf{N}_A^T \mathbf{j}_s dA \right) \delta \hat{\mathbf{A}} = 0 \quad \forall \delta \hat{\mathbf{u}}, \delta \hat{\varphi}, \delta \hat{\mathbf{A}}. \tag{2.56}
\end{aligned}$$

Here, we use partial integration as follows:

$$\begin{aligned}
& \int_{t_0}^{t_1} \int_{\Omega} \mathbf{N}_A^T \mathbf{e}_b \mathbf{B}_u \hat{\mathbf{u}} \delta \dot{\hat{\mathbf{A}}} dV dt \\
& = \underbrace{\int_{\Omega} [\mathbf{N}_A^T \mathbf{e}_b \mathbf{B}_u \hat{\mathbf{u}} \delta \hat{\mathbf{A}}]_{t_0}^{t_1} dV}_{=0} - \int_{t_0}^{t_1} \int_{\Omega} \mathbf{N}_A^T \mathbf{e}_b \mathbf{B}_u \dot{\hat{\mathbf{u}}} \delta \hat{\mathbf{A}} dV dt \tag{2.57}
\end{aligned}$$

$$\begin{aligned}
& \int_{t_0}^{t_1} \int_{\Omega} \mathbf{N}_A^T \boldsymbol{\xi} \mathbf{B}_{\text{grad}} \hat{\varphi} \delta \dot{\hat{\mathbf{A}}} dV dt \\
& = \underbrace{\int_{\Omega} [\mathbf{N}_A^T \boldsymbol{\xi} \mathbf{B}_{\text{grad}} \hat{\varphi} \delta \hat{\mathbf{A}}]_{t_0}^{t_1} dV}_{=0} - \int_{t_0}^{t_1} \int_{\Omega} \mathbf{N}_A^T \boldsymbol{\xi} \mathbf{B}_{\text{grad}} \dot{\hat{\varphi}} \delta \hat{\mathbf{A}} dV dt \tag{2.58}
\end{aligned}$$

$$\begin{aligned}
& \int_{t_0}^{t_1} \int_{\Omega} \mathbf{N}_A^T \boldsymbol{\xi} \mathbf{N}_A \dot{\hat{\mathbf{A}}} \delta \dot{\hat{\mathbf{A}}} dV dt \\
& = \underbrace{\int_{\Omega} [\mathbf{N}_A^T \boldsymbol{\xi} \mathbf{N}_A \dot{\hat{\mathbf{A}}} \delta \hat{\mathbf{A}}]_{t_0}^{t_1} dV}_{=0} - \int_{t_0}^{t_1} \int_{\Omega} \mathbf{N}_A^T \boldsymbol{\xi} \mathbf{N}_A \ddot{\hat{\mathbf{A}}} \delta \hat{\mathbf{A}} dV dt \tag{2.59}
\end{aligned}$$

Again, the nodal test function $\delta \hat{\mathbf{A}}$ does not change in time, so the corresponding terms vanish. Inserting this into Eq. (2.56) yields

$$\begin{aligned}
& \int_{\Omega_b} ((\mathbf{C}_b \mathbf{B}_u \hat{\mathbf{u}} - \mathbf{e}_b^T [-\mathbf{B}_{\text{grad}} \hat{\varphi} - \mathbf{N}_A \dot{\hat{\mathbf{A}}}]) \mathbf{B}_u \delta \hat{\mathbf{u}} - [\mathbf{e}_b \mathbf{B}_u \hat{\mathbf{u}} + \boldsymbol{\xi}_b (-\mathbf{B}_{\text{grad}} \hat{\varphi} - \mathbf{N}_A \dot{\hat{\mathbf{A}}})] \\
& \quad [-\mathbf{B}_{\text{grad}} \delta \hat{\varphi}] + [\mathbf{e}_b \mathbf{B}_u \dot{\hat{\mathbf{u}}} + \boldsymbol{\xi}_b (-\mathbf{B}_{\text{grad}} \dot{\hat{\varphi}} - \mathbf{N}_A \ddot{\hat{\mathbf{A}}})] [-\mathbf{N}_A \delta \hat{\mathbf{A}}] + \mu_b^{-1} \mathbf{B}_{\text{curl}} \hat{\mathbf{A}} \mathbf{B}_{\text{curl}} \delta \hat{\mathbf{A}} \\
& + \gamma \mathbf{B}_{\text{div}} \mathbf{B}_{\text{div}}^T \delta \hat{\mathbf{A}}) dV + \int_{\Omega_m} (\mathbf{B}_u^T \mathbf{C}_{\text{tang}} \mathbf{B}_u \delta \hat{\mathbf{u}} - [\boldsymbol{\xi}_m (-\mathbf{B}_{\text{grad}} \hat{\varphi} - \mathbf{N}_A \dot{\hat{\mathbf{A}}})] [-\mathbf{B}_{\text{grad}} \delta \hat{\varphi}] \\
& + [\boldsymbol{\xi}_m (-\mathbf{B}_{\text{grad}} \dot{\hat{\varphi}} - \mathbf{N}_A \ddot{\hat{\mathbf{A}}})] [-\mathbf{N}_A \delta \hat{\mathbf{A}}] + \mu_m^{-1} \mathbf{B}_{\text{curl}} \hat{\mathbf{A}} \mathbf{B}_{\text{curl}} \delta \hat{\mathbf{A}} \\
& + \gamma \mathbf{B}_{\text{div}} \mathbf{B}_{\text{div}}^T \delta \hat{\mathbf{A}} - \boldsymbol{\kappa}_m [-\mathbf{B}_{\text{grad}} \hat{\varphi} - \mathbf{N}_A \dot{\hat{\mathbf{A}}}] \mathbf{N}_A \delta \hat{\mathbf{A}}) dV \\
& - \left(\int_{\Omega} \mathbf{N}_u^T \mathbf{f} dV + \int_{\partial\Omega} \mathbf{N}_u^T \mathbf{t} dA \right) \delta \hat{\mathbf{u}} + \left(\int_{\Omega} \mathbf{N}_{\varphi}^T q_v dV + \int_{\partial\Omega} \mathbf{N}_{\varphi}^T q_s dA \right) \delta \hat{\varphi} \\
& - \left(\int_{\Omega} \mathbf{N}_A^T \mathbf{j}_v dV + \int_{\partial\Omega} \mathbf{N}_A^T \mathbf{j}_s dA \right) \delta \hat{\mathbf{A}} = 0 \quad \forall \delta \hat{\mathbf{u}}, \delta \hat{\varphi}, \delta \hat{\mathbf{A}}. \tag{2.60}
\end{aligned}$$

This equation can be split by the variations. By using the arbitrariness of the test functions and introducing the generalized nodal forces as

$$\begin{pmatrix} \hat{\mathbf{f}} \\ \hat{\mathbf{q}} \\ \hat{\mathbf{j}} \end{pmatrix} := \begin{pmatrix} \int_{\Omega} \mathbf{N}_u^T \mathbf{f} dV + \int_{\partial\Omega} \mathbf{N}_u^T \mathbf{t} dA \\ - \int_{\Omega} \mathbf{N}_{\varphi}^T q_v dV - \int_{\partial\Omega} \mathbf{N}_{\varphi}^T q_s dA \\ \int_{\Omega} \mathbf{N}_A^T \mathbf{j}_v dV + \int_{\partial\Omega} \mathbf{N}_A^T \mathbf{j}_s dA \end{pmatrix}, \tag{2.61}$$

the residual is then $\mathbf{R} = (\mathbf{R}_u \quad \mathbf{R}_{\varphi} \quad \mathbf{R}_A)^T =$

$$\begin{pmatrix} \hat{\mathbf{f}} + \int_{\Omega} -\mathbf{B}_u^T \hat{\sigma} dV \\ \hat{\mathbf{q}} + \int_{\Omega} -\mathbf{B}_{\text{grad}}^T \hat{\mathbf{D}} dV \\ \hat{\mathbf{j}} + \int_{\Omega} (-\mathbf{B}_{\text{curl}}^T \hat{\mathbf{H}} + \mathbf{N}_A^T (\dot{\hat{\mathbf{D}}} + \hat{\mathbf{J}}) - \gamma \mathbf{B}_{\text{div}} \mathbf{B}_{\text{div}}^T \hat{\mathbf{A}}) dV \end{pmatrix} \tag{2.62}$$

By writing this equation in matrix form, we recover the equation system Eq. (2.32).

3 Article 2: Inverse modeling of cancellous bone using artificial neural networks

This article was published as:

Stieve V., Blaszczyk M. and Hackl K. (2022). Inverse modeling of cancellous bone using artificial neural networks. *ZAMM-Journal of Applied Mathematics and Mechanics/Zeitschrift für Angewandte Mathematik und Mechanik* 102(6), e202100541.

3.1 Abstract

Artificial neural networks are used to solve different tasks of daily life, engineering and medicine. In this work, we investigate its suitability for the examination of simulation results of cancellous bone with the aim to evaluate whether the bone is affected by osteoporosis. This bone disease is characterised by a reduction of the cortical bone phase, one of the two main components of the bone. The neural network predicts the simulated volume fraction in different parts of a cylinder, which models the bone. As a basis for its calculations, the neural network gets the information about the magnetic field inside the cylinder from finite element simulations. Examinations show that it is possible to train neural networks on solving that task with very high accuracies.

3.2 Introduction

Osteoporosis is one of the most common bone diseases in the world. It is characterised by a decrease of the mass density of the bone, making it thinner and weaker, which can eventually lead to fractures. Currently, it is diagnosed by dual-energy X-ray absorptiometry as standard which gives an information about the bone mineral density. However, it is desirable to find a radiation-free and cheaper method to make it available in all countries [Wani and Arora (2020), Yamamoto et al. (2020)].

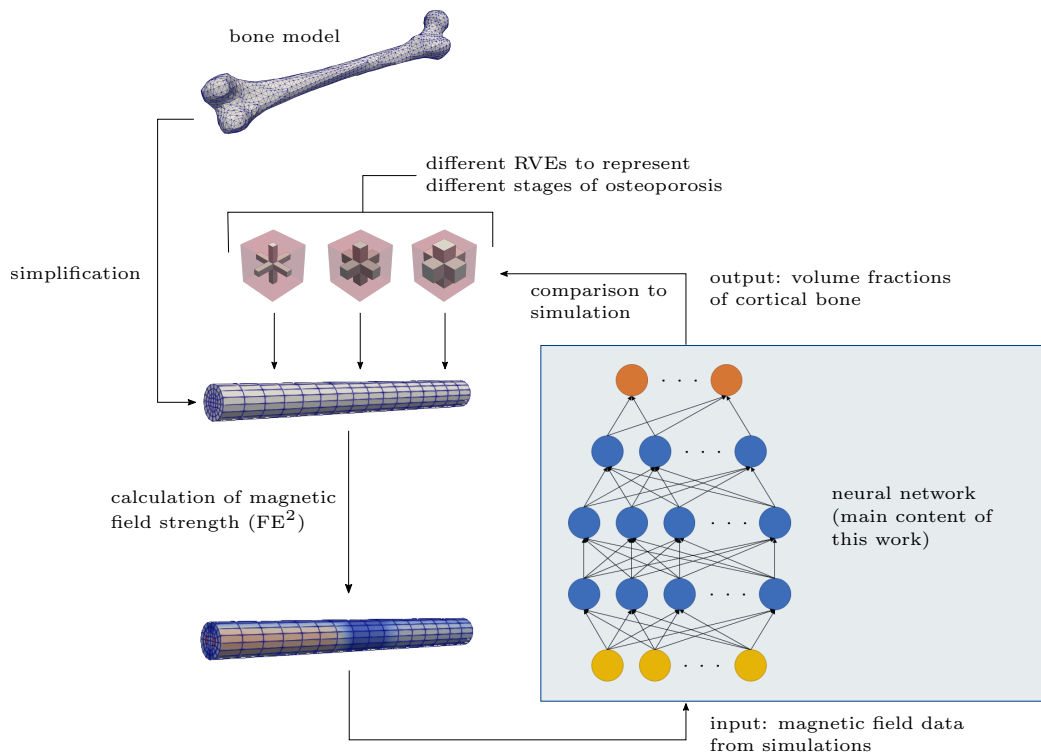


Figure 3.1: Overview and schematic flow of the task.

Due to the ability of mapping and adapting non-linear functions (artificial) neural networks have become a popular method for solving difficult tasks in many different areas of appli-

cation, for example, in engineering and science, medicine, finance and games. An overview about the method and its applications can be found in literature Abiodun et al. (2018), Goodfellow et al. (2016). While introduced first in 1943 [McCulloch and Pitts (1943)], especially during the last decade, miscellaneous research has been made for example in designing neural networks, that are helpful for diagnosis. More specifically, for the diagnosis of osteoporosis, there are two main inputs from which the neural networks are supposed to find a solution: questionnaires giving information about the patients and images of the bone recorded by different imaging methods [Wani and Arora (2020)]. In Ref. Mohamed et al. (2003), a prediction about the bone mineral density is made from sex and age as well as anthropometric measurements like weight, height and waist-to-hip ratio. While Chiu et al. (2006) just adds postmenopausal status and coffee consumption to the anthropometric measurements, Iliou et al. (2017) uses many additional risk factors like coffee, alcohol and nicotine consumption as well as earlier relevant diseases, occupation and sports of the patients.

The first possibility to record images is radiography. Vishnu et al. (2015) and Singh et al. (2017) created classification networks from X-ray images. Singh et al. (2017) additionally compared the results to other machine learning algorithms like support vector machines. Yu et al. (2016) combines the use of radiographic images with facts like drug and fracture history, pain, age and gender as well as serum specimens, but requires the extraction of features from the images by orthopedists or radiologists before applying the neural network. As a second image recording method, an MRI is suggested in literature Deniz et al. (2018) to train a convolutional neural network. A last possibility is used in literature Fang et al. (2021), where a convolutional neural network is developed to determine the bone mineral density from a CT scan.

While these approaches yield promising results, one main disadvantage is the necessity to obtain images by X-ray or CT scan, which can be expensive and might not be available in every part of the world. An alternative for the early detection of osteoporosis is the application of sonography, which can be modeled by a suitable material model and numerical methods, that are well known in the field of engineering. The inclusion of neural networks in the workflow of these tasks is also a common strategy to improve simulations. For example, neural networks can be used instead of a constitutive relation to model the material behavior from experimental stress-strain data [Ghaboussi et al. (2012)]. Another approach is training the neural network using numerical simulation results, obtained e.g. via the finite element method (FEM), to eventually replace the necessity to perform those simulations by using the considerably faster trained neural network instead for new test cases. In Ref. Chamekh et al. (2008), a neural network for the identification of anisotropic plasticity parameters important e.g. in deep drawing, is trained by finite element simulations. The trained network can then be used instead of the finite element simulations for parameter identification. An application to predicting the volume fractions of functionally graded materials using data from both experiments and simulations is presented in literature Han et al. (2003). For multiscale simulations, a neural network can be trained with the objective of replacing expensive microscale simulations by the trained neural network [Zheng et al. (2021)]. In Ref. Kumar et al. (2020), two neural networks are used to first find a metamaterial topology from a given stiffness and then to calculate the stiffness of the found topology, comparing it to the queried stiffness.

In this work, we focus on the evaluation of simulation results and create neural networks to solve the inverse task of detecting the bone structure, which has been used to perform the simulation. We use our model of a two-phase bone material to simulate the application of ul-

trasound to a bone [Blaszczyk and Hackl (2022), Schlick et al. (2021), Blaszczyk and Hackl (2021a), Blaszczyk and Hackl (2021b)]. Oftentimes, in modeling only mechanical effects were considered. Recent research set the basis to include electric and magnetic effects as well [Dorfmann and Ogden (2014), Gilbert et al. (2021)]. Because of the piezoelectric character of bone and the coupling of electric and magnetic effects by the Maxwell equations, ultrasonic waves cause a magnetic field in the bone. In Ref. Blaszczyk and Hackl (2022), we introduced a multiscale material model capturing these effects and obtained simulation results by applying the finite element square method (FE²). To model different stages of osteoporosis, we constructed representative volume elements (RVEs) with different volume fraction of cortical bone ρ_b , which is one of the two main components of the bone besides bone marrow. In a healthy bone, its fraction is approximately 30%, but it may be reduced up to 5% in a degenerated bone [Steeb (2010), Ilić et al. (2010)]. We showed in the numerical simulations, that the magnetic field strength is reduced for RVEs with lower volume fraction of cortical bone [Blaszczyk and Hackl (2022), Schlick et al. (2021), Blaszczyk and Hackl (2021b)]. In this contribution, we randomize the used RVEs along the length of the bone model and calculate the magnetic field strength for different timesteps, which is the input of the neural network model. The neural network should then output the correct volume fractions of cortical bone, which were used for that simulation. An overview about the task is given in Figure 3.1.

This article is structured as follows. Following the introduction, in Section 3.3 we shortly summarize our material model for the forward problem. In Section 3.4 we introduce our test case for the inverse problem and describe the creation of our training, validation and test data. In Section 3.5 we explain how our neural networks are designed and which optimizers and activation functions yield the best results. In Section 3.6 we present and discuss our results for different neural network designs. Finally, in Section 3.7 we draw conclusions about our work and give an outlook for future research.

3.3 Material model of the forward problem

For a better understanding we shortly introduce our material model used for the forward problem and data generation. A detailed derivation can be found in literature Blaszczyk and Hackl (2022). To model the microscale, we employ the following thermodynamic energy functional in the domain Ω_y

$$\begin{aligned} \Pi = & \int_{\Omega_b} \Psi_b(\boldsymbol{\varepsilon}, \mathbf{E}, \mathbf{B}) dV + \int_{\Omega_m} \Psi_m(\boldsymbol{\varepsilon}, \boldsymbol{\varepsilon}^i, \mathbf{E}, \mathbf{B}) + \mathcal{C} dV \\ & + \int_{\Omega_m} \int_t \Delta(\dot{\boldsymbol{\varepsilon}}^i, \dot{\mathbf{A}}) dt dV + \int_{\Omega} \Psi_g(\nabla \cdot \mathbf{A}) dV - W_{\text{ext}}, \end{aligned} \quad (3.1)$$

which contains the energy densities Ψ_b and Ψ_m of both phases, a volume constraint \mathcal{C} , dissipation and gauge functionals (Δ and Ψ_g) and the potential of the generalized external forces W_{ext} . The main variables of the problem are then the mechanical displacements \mathbf{u} , the electric scalar potential φ and the magnetic vector potential \mathbf{A} . The state variables are the mechanical strain $\boldsymbol{\varepsilon}$, the electric field \mathbf{E} and the magnetic flux density \mathbf{B} , calculated as

$$\boldsymbol{\varepsilon} = \frac{1}{2} (\nabla \mathbf{u} + \nabla^T \mathbf{u}), \quad \mathbf{E} = -\nabla \varphi - \dot{\mathbf{A}} \quad \text{and} \quad \mathbf{B} = \nabla \times \mathbf{A}. \quad (3.2)$$

From the Nabla product rules, it follows that two of the four Maxwell equations are satisfied this way. The energy densities for both phases are

$$\begin{aligned}\Psi_b &= \frac{1}{2}(\boldsymbol{\varepsilon} \cdot \mathbb{C}_b \cdot \boldsymbol{\varepsilon} - \mathbf{E} \cdot \boldsymbol{\xi}_b \cdot \mathbf{E} + \mathbf{B} \cdot \boldsymbol{\mu}_b^{-1} \cdot \mathbf{B}) - \mathbf{e}_b \cdot \boldsymbol{\varepsilon} \cdot \mathbf{E} \quad \text{and} \\ \Psi_m &= \frac{1}{2}((\boldsymbol{\varepsilon} - \boldsymbol{\varepsilon}^i) \cdot \mathbb{C}_m \cdot (\boldsymbol{\varepsilon} - \boldsymbol{\varepsilon}^i) - \mathbf{E} \cdot \boldsymbol{\xi}_m \cdot \mathbf{E} + \mathbf{B} \cdot \boldsymbol{\mu}_m^{-1} \cdot \mathbf{B}),\end{aligned}\quad (3.3)$$

consisting of quadratic energies for mechanical, electric and magnetic effects, resulting in a linear problem. We include a piezoelectric energy term for the cortical bone phase. For the bone marrow phase, an inelastic strain $\boldsymbol{\varepsilon}^i$ is introduced.

From the first and second derivatives of the energy densities with respect to the state variables, the flux quantities and material tensors can be derived. We obtain the fluxes mechanical stress $\boldsymbol{\sigma}$, electric displacement \mathbf{D} and magnetic field strength \mathbf{H} . In Eq. (3.3), \mathbb{C} is the mechanical stiffness tensor, $\boldsymbol{\xi}$ is the permittivity tensor, $\boldsymbol{\mu}^{-1}$ is the inverse permeability tensor and \mathbf{e}_b is the piezoelectric tensor. The constraint function is

$$C = \lambda \operatorname{tr}(\boldsymbol{\varepsilon}^i), \quad (3.4)$$

enforcing volume conservation of the inelastic deformation. Here, λ is a Lagrange multiplier. The dissipation function reads

$$\Delta = \frac{1}{2}(\mu_v^{-1}|\dot{\boldsymbol{\varepsilon}}^i|^2 - \boldsymbol{\kappa} \mathbf{E}^2), \quad \text{with} \quad \mathbf{J} = \boldsymbol{\kappa} \mathbf{E}. \quad (3.5)$$

Thus, Δ governs the evolution of the inelastic strain and the energy loss due to conduction. The latter satisfies Ohm's law (Eq. (3.5), right). Both parts of the dissipation only occur in the bone marrow phase. Here, the viscosity parameter $\mu_v^{-1} > 0$, the electric conductivity tensor $\boldsymbol{\kappa} = \kappa_1 \mathbf{I}$, with the identity tensor \mathbf{I} , the electric conductivity $\kappa_1 > 0$ and the electric current density \mathbf{J} are introduced. The gauge function is

$$\Psi_g = \frac{\gamma}{2}(\nabla \cdot \mathbf{A})^2 \quad (3.6)$$

and ensures, that a unique solution for the magnetic vector potential \mathbf{A} is obtained, with the numerical parameter γ . Finally, the potential of generalized external forces is

$$W_{\text{ext}} = \int_{\Omega} (\mathbf{f} \cdot \mathbf{u} - q_v \cdot \varphi + \mathbf{j}_v \cdot \mathbf{A}) dV + \int_{\partial\Omega} (\mathbf{t} \cdot \mathbf{u} - q_s \cdot \varphi + \mathbf{j}_s \cdot \mathbf{A}) dA. \quad (3.7)$$

Here, \mathbf{f} and \mathbf{t} are the mechanical volume and surface forces, q_v and q_s are the electric volume and surface charges and \mathbf{j}_v and \mathbf{j}_s are the volume and surface currents. To calculate the weak and strong form of the problem, the energy functional has to become stationary with respect to the main variables and internal variables. For the inelastic strain, we derive the evolution equation

$$\dot{\boldsymbol{\varepsilon}}^i = \mu_v \boldsymbol{\sigma}_{\text{dev}}, \quad (3.8)$$

with $\boldsymbol{\sigma}_{\text{dev}} = \boldsymbol{\sigma} - \frac{1}{3} \operatorname{tr}(\boldsymbol{\sigma}) \mathbf{I}$ denoting the deviatoric part of the mechanical stress $\boldsymbol{\sigma}$. Then, the weak form of the remaining variational equation is

$$\begin{aligned}\int_{\Omega} (\boldsymbol{\sigma} \cdot \delta \boldsymbol{\varepsilon} - \mathbf{D} \cdot \delta \mathbf{E} + \mathbf{H} \cdot \delta \mathbf{B} - \mathbf{J} \cdot \delta \mathbf{A} \\ + \gamma(\nabla \cdot \mathbf{A}) \cdot \delta(\nabla \cdot \mathbf{A})) dV - \delta W_{\text{ext}} = 0 \quad \forall \delta \mathbf{u}, \delta \varphi, \delta \mathbf{A}.\end{aligned}\quad (3.9)$$

This form is used to insert a FEM ansatz. We apply partial integration to each term to obtain the strong form of the problem as

$$\begin{aligned}
\nabla \cdot \boldsymbol{\sigma} + \mathbf{f} &= \mathbf{0} \text{ in } \Omega & \boldsymbol{\sigma} \cdot \mathbf{n} &= \mathbf{t} \text{ on } \partial\Omega \\
\nabla \cdot \mathbf{D} &= q_v \text{ in } \Omega & \mathbf{D} \cdot \mathbf{n} &= -q_s \text{ on } \partial\Omega \\
\nabla \times \mathbf{H} = \dot{\mathbf{D}} + \mathbf{J} + \gamma \nabla(\nabla \cdot \mathbf{A}) + \mathbf{j}_v & \text{ in } \Omega & \mathbf{H} \times \mathbf{n} &= \mathbf{j}_s - \gamma(\nabla \cdot \mathbf{A})\mathbf{n} \text{ on } \partial\Omega
\end{aligned} \tag{3.10}$$

recovering the mechanical equilibrium condition, the two remaining Maxwell equations and boundary conditions, including the gauge. Here, \mathbf{n} is the normal vector pointing outwards. Additionally, we receive the jump conditions between the phases

$$\begin{aligned}
[[\boldsymbol{\sigma}]]_{\text{bm}} \cdot \mathbf{n} &= \mathbf{t} \text{ on } \partial\Omega_{\text{bm}}, & [[\mathbf{D}]]_{\text{bm}} \cdot \mathbf{n} &= -q_s \text{ on } \partial\Omega_{\text{bm}} \text{ and} \\
[[\mathbf{H}]]_{\text{bm}} \times \mathbf{n} &= \mathbf{j}_s - \gamma [[\nabla \cdot \mathbf{A}]]_{\text{bm}} \mathbf{n} \text{ on } \partial\Omega_{\text{bm}}
\end{aligned} \tag{3.11}$$

on the interface $\partial\Omega_{\text{bm}}$ and the evolution equation of the inelastic strain (Eq. (3.8)) in Ω_{m} . Here $[[\cdot]]_{12} := (\cdot)_1 - (\cdot)_2$ denotes the difference between the phases.

For the macroscale, the same weak and strong form (bar the evolution equation of the inelastic strain) can be derived for the domain Ω_{x} and the set of corresponding macroscale quantities $\overline{(\cdot)}$. The key difference here is that instead of using a material model on¹ the macroscale, the calculation of the fluxes now depends on the microscale calculations:

$$(\overline{\boldsymbol{\sigma}}, \overline{\mathbf{D}}, \overline{\dot{\mathbf{D}}}, \overline{\mathbf{H}}, \overline{\mathbf{J}}) = f_{\text{RVE}}(\overline{\boldsymbol{\varepsilon}}, \overline{\mathbf{E}}, \overline{\mathbf{B}}). \tag{3.12}$$

3.4 Data Collection

To model the bone, we use a cylinder mesh, which is separated into 16 elements along its length (Figure 3.2, (a)). Each of these parts is separated into 48 elements (Figure 3.2, (b)).

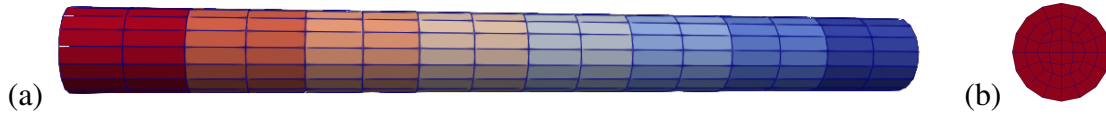


Figure 3.2: Mesh of the cylinder, (a) along the length, (b) in the cross section. The different colors refer to the sections with the same volume fractions of cortical bone.

ID	1	2	3	4	5	6
ρ_{b}	5.3%	10.4%	14.5%	19.1%	24.2%	29.5%

Table 3.1: Possible volume fraction values depending on the ID key (RVE number).

Each two of those parts, meaning all of the 96 elements, will be assigned the same volume fraction of cortical bone ρ_{b} by using only the corresponding RVE in that part. Table 3.1 shows the values of the possible volume fractions. To obtain more realistic distributions,

¹Corrected spelling, cf. Stieve et al. (2022)

their assignment to the elements is based on Haar functions. They are usually used to approximate functions as a linear combination

$$\bar{h}(x) = c_0\phi(x) + \sum_{n=0}^2 \sum_{k=0}^{2^n-1} c_{nk}\psi_{n,k}(x) \quad (3.13)$$

of piecewise constant functions $\phi(x)$ and $\psi_{n,k}(x)$ [Aziz et al. (2014), Struzik and Siebes (1999)]. Here, we need a piecewise constant function on eight pieces, which restricts our choice of the parameter n to $n_{max} = 2$.

$$\phi(x) = \begin{cases} 1 & \text{for } 0 \leq x < 1 \\ 0 & \text{otherwise} \end{cases} \quad (3.14)$$

and

$$\psi(x) = \begin{cases} 1 & \text{for } 0 \leq x < \frac{1}{2} \\ -1 & \text{for } \frac{1}{2} \leq x < 1 \\ 0 & \text{otherwise} \end{cases} \quad (3.15)$$

are the basis functions for the Haar wavelets. Then, we obtain the Haar system as

$$\psi_{n,k}(x) = 2^{n/2}\psi(2^{-n}x - k), \quad n > 0, \quad k = 0, \dots, 2^n. \quad (3.16)$$

By the choice of the parameters c_{nk} , the different functions are constructed [Aziz et al. (2014), Talukder and Harada (2010), Graps (1995)]. To keep the model realistic, we will not use those functions, where a jump of more than two volume fractions between neighboring elements occurs. By applying the correlation

$$h_i(x) = \begin{cases} 6 & \text{for } |\bar{h}_i(x)| \leq 1 \\ 5 & \text{for } 1 < |\bar{h}_i(x)| \leq 2 \\ 4 & \text{for } 2 < |\bar{h}_i(x)| \leq 3 \\ 3 & \text{for } 3 < |\bar{h}_i(x)| \leq 4 \\ 2 & \text{for } 4 < |\bar{h}_i(x)| \leq 5 \\ 1 & \text{otherwise} \end{cases}, \quad i = 1, \dots, 8, \quad (3.17)$$

we map the values of the constant pieces of the function to the IDs corresponding to the volume fraction values. The resulting function assigning one of the six volume fraction values to each of the eight elements of the cylinder describes the expected outputs of the neural network.

This information is also what we entered into the program presented in Blaszczyk and Hackl (2022) to assign the different RVEs to the different parts of the cylinder and calculate the magnetic field via the FE². The displacement applied for that calculation is linearly increasing during four time steps. The resulting magnetic field in the 969 nodes of the cylinder $\mathbf{H} = (H_x \ H_y \ H_z)^T$, with its three directional components, is the input to the neural network.

Previously, we analyzed the interrelation between the value of the volume fractions and the mean value of the magnetic field, which shows that the change in the magnetic field decreases with increasing volume fraction. Between the RVEs with the highest two volume fractions, we observed nearly no difference (Figure 3.3) [Blaszczyk and Hackl (2022),

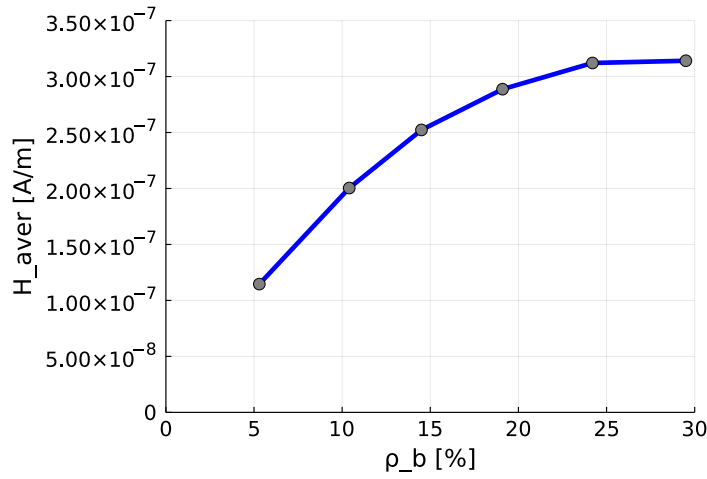


Figure 3.3: Average magnetic field strength for different RVEs (cf.[Blaszczyk and Hackl (2022), Blaszczyk and Hackl (2021b)]).

Blaszczyk and Hackl (2021b)]. Therefore, it seems likely that it is easier for the neural network to correctly determine the smaller volume fraction values. For that reason, we will also examine how the performance of the neural network changes when merging the fifth and the sixth class, which is done by including every occurrence of a volume fraction of $\rho_b = 29.5\%$ in the class of $\rho_b = 24.2\%$.

3.5 Neural Network Design

We used two approaches for the main structure of the neural networks. Firstly, we put the eight values that have to be determined into a vector, which we then use as output. Secondly, we use the finiteness of the number of possible volume fractions to change the problem into eight classification problems, where each of the classes corresponds to one volume fraction. The corresponding vector for the expected output of each problem is the onehot-encoding of the class ID. The network outputs a probability for each class to be the correct one.

We use a feed-forward neural network for the calculation. The input layer needs to be build out of 11628 neurons, because the three-dimensional magnetic field in 969 nodes at four timesteps after reshaping leads to an input vector of that size. As a good compromise between minimizing the number of calculations and maximizing the accuracy, for the first approach we chose two hidden layers of size 200 and two hidden layers of size 100, followed by the output layer consisting of eight neurons. For the second approach, using one hidden layer consisting of 200 neurons and one consisting of 100 neurons is sufficient. In this case the output layer has as many neurons as classes are possible, which means five or six for this task. To calculate the whole volume fraction distribution, eight of those networks are required.

1200 training data instances are sufficient for reaching a good performance. The validation of the network is done by 500 validation data instances and 500 test data instances are used to verify the performance of the network on unknown data. We used a batchsize of 32 in the first approach, while in the second approach we trained the networks by batches of size 64. We chose the activation functions as well as the optimizers individually for each of the

networks. The choices which yielded the best results are shown in Table 3.2.

Network	Five possible classes		Six possible classes	
	Activation function	Optimizer	Activation function	Optimizer
all elements	swish	Radam	relu	AdamW
1	selu	Adam	relu	Radam
2	selu	Radam	selu	AdaMax
3	swish	AmsGrad	selu	Radam
4	relu6	Radam	relu	AdamW
5	swish	Radam	selu	Radam
6	softsign	AdaMax	softsign	AdaMax
7	swish	AmsGrad	relu6	Radam
8	selu	AdaMax	relu	Radam

Table 3.2: Used activation functions and optimizers for both approaches.

In both cases we used the pocket algorithm based on the number of elements that the networks classified correctly, which means that after each training step we checked on the set of validation data instances whether the number of correct classifications increased. If this was the case, we continued training using the new weights. For the other case, we stored the previous weights and can reload them, such that we can continue the training with them. To prevent overfitting, we used the early stopping method to determine when to stop the training. The method uses the validation data to regularly check during the whole training process whether the number of correct classifications increases. If it had not increased during ten epochs, we stopped the training.

For the implementation, we used the programming language Julia [Bezanson et al. (2022)] and the machine learning libraries Flux.jl [Innes (2018), Innes et al. (2018) and NNlib.jl, which provide implementations for the building blocks of the neural network.

3.6 Results

Besides the number of correct classifications, we constructed an error measure to rate the quality of the different networks. For the first approach, the error ϵ is determined by

$$\epsilon(\hat{y}, y) = \sum_{i=1}^8 \sum_{j=1}^q \frac{|\hat{y}_{ij} - y_{ij}|}{q \cdot 8 \cdot \max(\rho_{b,\max} - y_{ij}, y_{ij} - 0.053)}. \quad (3.18)$$

Analogously, we calculate the error of the classification networks as

$$\epsilon(\hat{y}, y) = \sum_{j=1}^q \frac{|\text{oc}(\hat{y}_j) - \text{oc}(y_j)|}{q \cdot \max(\text{ID}_{\max} - \text{oc}(y_j), \text{oc}(y_j) - 1)}, \quad (3.19)$$

where oc is the onecold function. For both error measures, q is the size of the test or validation set, respectively, which is 500 for both. y describes the expected output of the network, while \hat{y} is the output of the network. Both include all output values for all the elements of the dataset. The onecold function determines the ID of the element of the output vector

which has the highest value. By this construction, the error is a mean value of the distance of the expected and the actual output divided by the maximum possible distance from the expected output when staying inside the range of the possible expected outputs.

The described error as well as the number of correct classifications for each of the explained networks is given in Table 3.3. There are 500 test data instances for each of which eight values have to be predicted, such that the maximum reachable number of correct classifications is 4000. By having an accuracy $\geq 96\%$ and an error ≤ 0.05 , all the considered networks

Number of Classes	Classification networks?	Error	Correctly classified	
			Absolute	Relative
5	no	0.048	3953	98.83%
5	yes	0.004	3945	98.63%
6	no	0.047	3854	96.35%
6	yes	0.004	3934	98.35%

Table 3.3: Quality of the different networks (maximum = 4000).

lead to very good results. Comparing the different networks, the classification networks' performance is better than the one of the single network which considers all elements of the cylinder. In addition, merging the fifth and the sixth class increases the quality of the network. The difficulties the network has in distinguishing the fifth and the sixth class can also be seen in Table 3.4. While for the other classes an accuracy of more than 97% is reached, for the fifth and especially for the sixth class, the quality is much lower. When using a single network, less than 70% of the elements that should be classified to the sixth class are classified to the sixth class. For the classification networks, the corresponding value is 90% and therefore also much worse than for the other classes. For that reason, it can be useful to accept both classes as healthy bone and not to distinguish between them.

For a similar reason, it is not just important how many classifications are done correctly, but also how far away the predicted classes of the wrongly classified elements are from the correct classes: If they are close to each other, it is still a good information about the health of the bone. Table 3.5 shows that this is the case for the designed network. A distance of one means that e.g. an element of class four is classified as class three or class five. In each of the four cases all elements are classified to the correct or to the neighbouring class, such that for all elements a useful information is given about the health of the bone in the corresponding part of the cylinder modeling the bone. On these grounds it can be said that

Class	1	2	3	4	5	
should be in this class	302	674	1109	1025	890	-
is in this class - one single network	302	674	1108	1013	856	-
is in this class - 8 classification networks	302	664	1095	1015	869	-
Class	1	2	3	4	5	6
should be in this class	302	674	1109	1025	655	235
is in this class - one single network	299	672	1104	997	626	156
is in this class - 8 classification networks	301	666	1106	1017	632	212

Table 3.4: Comparison of the network types with respect to the different classes.

Element	Distance for five classes		Distance for six classes	
	0	1	0	1
1	493	7	494	6
2	495	5	490	10
3	489	11	492	8
4	499	1	498	2
5	497	3	499	1
6	492	8	492	8
7	487	12	480	20
8	493	7	489	11
\sum	3945	54	3934	66
all	3953	47	3854	146

Table 3.5: Distances from the expected outputs.

the neural networks do nearly all classifications sufficiently well to rate the quality of the different parts of the bone.

To reach the given results, it is important to wisely choose the adjustable parameters of the neural networks. For this task, using bigger networks or more training data than it was done does not lead to better results. However, using less training data or smaller networks results in less accuracy.

The most important choices to make are the activation function and the optimizer. In Table 3.6 and Table 3.7, the number of correct classifications is shown for different choices of the activation function as well as different choices of the optimizer for the one-single network approach using five classes. In both cases, the maximum possible number would

Activation function		swish	relu	relu6	softsign	selu
correctly classified	absolute	3962	3885	3808	3736	3395
	relative	99.05%	97.13%	95.20%	93.40%	84.88%

Table 3.6: Influence of the activation function to the number of correct classifications (maximum = 4000).

Optimizer		Radam	AdamW	Adam	AMSGrad
correctly classified	absolute	3962	3918	3899	3857
	relative	99.05%	97.95%	97.48%	96.43%
Optimizer		AdaMax	ADADelta	RMSProp	
correctly classified	absolute	3833	3528	3257	
	relative	95.83%	88.20%	81.43%	

Table 3.7: Influence of the optimizer to the number of correct classifications (maximum = 4000).

be 4000, because there are eight elements in each of the 500 validation data instances. Both tables together show that already changing one of those parameters results in a degradation worth mentioning of the quality of the network. Using other choices for both parameters

leads to even worse results: As an example, using `selu` as activation function and `RMSProp` as optimizer in the one-single network approach, only 303 classifications are done correctly and the error of 0.936 is close to one, which would be the maximum possible error if all outputs would be inside the bounds of the expected outputs.

A last important point besides the quality of the results of the calculations is the calculation time. With our approach, collecting sufficient data takes about three days using a computer cluster. Training a single network can be done in less than 1 h. Once the training is finished, the network which calculates the volume fraction values for all the elements of the cylinder needs approximately $1/100$ s to find the solution. Each of the classification networks also has a calculation time of $1/100$ s, when doing all those calculations in a row $1/10$ s is required. Because of their independence, they can be done in parallel. Therefore, for both approaches just approximately $1/100$ s is required to calculate the distribution of volume fractions of the cortical bone phase from a given magnetic field when using the trained neural network.

3.7 Conclusion

We used a cylinder to model the bone. Based on that, we developed neural networks which get the magnetic field in the cylinder as input and calculate the volume fractions of cortical bone in different parts of the cylinder. We used two approaches for the neural networks: a regression approach to approximate the volume fractions in different parts of the cylinder and a classification approach where we use one network for each part of the cylinder to choose the class corresponding to the volume fraction value for that part. The second approach can be used because the possible volume fractions are restricted to six different values. Both approaches reached high accuracies of $> 96\%$ and have small calculation times. While the quality of the classification approach is even a little higher than the one of the regression approach, an advantage of the regression approach is its extensibility to e.g. more RVE numbers, which is not easily possible for the classification networks. Another improvement can be made by joining the two classes for high volume fractions both corresponding to healthy bone. These results show that a neural network is able to predict the distribution of the volume fraction of cortical bone simulations when knowing the magnetic field in the bone with a high accuracy.

With further development, it could therefore be a suitable part of a diagnosis method for osteoporosis. To reach that, a more detailed model of the bone could be used and the surrounding of the bone in the body could be modeled. Additionally, precise material parameters are necessary. For our simulations, we assumed, that the magnetic field data is known to the neural network at every node of the finite element mesh. In contrast, depending on the used measurement technology, the spacial resolution of this data might be significantly less in real-world applications like data generated from experimental setups or patients. Thus, for future research, it could be examined whether such neural networks can predict reliable results even when given less accurate input. This not only refers to the resolution of the input data, but also its accuracy. Deviations from measurement errors could be simulated by including synthetic noise in the data. Finally, it might be useful to allow additional volume fraction values or to separate the bone into more parts.

4 Article 3: On the effects of a surrounding medium and phase split in coupled bone simulations

This article was published as:

Blaszczyk M. and Hackl K. (2024). On the effects of a surrounding medium and phase split in coupled bone simulations. *ZAMM-Journal of Applied Mathematics and Mechanics/Zeitschrift für Angewandte Mathematik und Mechanik* 104(5), e202200595.

4.1 Abstract

In our previous contributions we established a multiscale, multiphase material model for the simulation of cancellous bone with the novel idea of including the full coupling of mechanical, electric and magnetic effects, which could be used for example, for the early detection of osteoporosis. While our calculations have already shown promising results, our previous approach lacks very important aspects, strongly limiting the applicability of our findings. In this paper we extend our base model by considering the effect of a surrounding medium on our bone specimen, using improved boundary conditions and differentiating between cortical bone, bone marrow and spongy bone to better reflect the physiological properties of bone. We show numerical results and compare our calculations to our previous modeling.

4.2 Introduction

Bone is a biological organ, which as a material has interesting properties. Composed of the phases cortical bone and bone marrow, it is very stiff and strong, while maintaining a light weight [Hamed et al. (2010)]. The most widespread bone disease in elderly population is osteoporosis [Reginster and Burlet (2006); Wade et al. (2014)], characterized by the degeneration of bone tissue [Clynes et al. (2020)]. By reducing the mass density of bone, this disease makes the bone thinner and weaker, thus increasing the likelihood of fractures [Peck (1993); Tsukutani et al. (2015)]. In a healthy bone, the volume fraction of cortical bone is approximately 30%, but it may be reduced up to 5% in a degenerated bone [McKelvie and Palmer (1991); Steeb (2010)]. Current diagnosis of osteoporosis is usually done by dual-energy x-ray absorptiometry to receive information about the bone mineral density [Blake and Fogelman (2007)]. However, it is desirable to find less invasive and cheaper tools for the early detection of this disease. A possible alternative may be the use of sonography [Güzelsu and Saha (1981); Kaufman et al. (2008); Mano et al. (2007)]. Numerical simulations can support the development of finding and enabling medical diagnostic based on this method.

In material modeling of bone, previously oftentimes only mechanical effects were considered. Examples include Refs. Ilić et al. (2010); Chen et al. (2018); Gardner et al. (2000). Recent research set the basis to include electric and magnetic effects as well [Dorfmann and Ogden (2014); Gilbert et al. (2021)]. In a series of previous contributions [Blaszczyk and Hackl (2022); Schlick et al. (2021); Blaszczyk and Hackl (2021a,b); Stieve et al. (2022)], we presented a novel multiscale model of a two-phase bone material to simulate the application of ultrasound to a bone and to investigate the resulting magnetic field strength depending on the health of the bone. As the cortical bone material is piezoelectric, small mechanical deformations from for example ultrasonic waves cause an electric field in the bone. A time-dependent electric field then creates a magnetic field due to the coupling by the Maxwell equations. To capture these effects, we differentiated between the bone phases cortical bone (modeled as a piezoelectric and insulating solid) and bone marrow (modeled as a viscoelastic and conducting solid), where we indicate the affiliation to the phases by $(\cdot)_b$ and $(\cdot)_m$, respectively. Then, we obtained simulation results by applying the finite element square method (FE²). To model different stages of osteoporosis, we constructed representative volume elements (RVEs) with different volume fraction of cortical bone ρ_b . We showed in the

numerical simulations, that the magnetic field strength is reduced for RVEs with lower volume fraction of cortical bone [Blaszczyk and Hackl (2022); Schlick et al. (2021); Blaszczyk and Hackl (2021b)].

While these results were already promising, some limitations occur, which strongly limit the applicability of our investigations. Our macroscopic models did not contain a boundary box to include the influence of a surrounding medium, for example, air or water. Such an approach is fine for purely mechanical modeling, but electromagnetic fields exist both within the body and in the outside domain [Yang and Dayal (2011)]. Therefore, to allow proper decay of the fields, the inclusion of a surrounding medium in the model may be necessary. However, constructing such meshes can be difficult [Smajic et al. (2015)] and depending on its size may increase the computation time significantly. Examples of coupled modeling with the inclusion of an outside domain can be found in Refs. Bartel et al. (2018); Buckmann et al. (2019) for magnetomechanical coupling. In Ref. Yvonnet and Liu (2017), an electromechanical numerical framework also including flexoelectricity is introduced, which covers cases like modeling a soft dielectric in a surrounding medium in detail. Alternatively, boundary methods, for example, perfectly matched layers [Berenger (1994)] or the Galerkin boundary element method [Buffa and Hiptmair (2003)], could be used, but they require additional effort regarding implementation.

Another aspect of dividing the macroscopic model is the differentiation not only between bone and outside, but also between different domains within the bone part of our model. Real human bones are built complicated and consist of different types of bone structure. A detailed physiological analysis can be found in Ref. Locke (2004). Therefore, distinguishing between different macroscopic bone phases may be necessary to obtain realistic results.

In this contribution, we extend our previous model by dividing the macroscopic model into different domains, with the aim of improving the applicability and realism of the model. For this purpose we constructed a boundary box around our previous used cylinder model to capture the effects of a surrounding medium and investigate, to what extent the inclusion of the boundary box influences the whole results. Additionally, this way we were able to apply suitable boundary conditions, making the model more realistic. Finally, we also show new results by applying a phase split within the cylinder to reflect the physiological properties of long human bones.

This article is structured as follows. Subsequent to the introduction, in Section 4.3 we shortly summarize our material model and introduce the extension to a surrounding medium. Additionally, we cover the differentiation between different macroscopic bone phases. In Section 4.4, we discuss the numerical implementation of the model. In Section 4.5, we show new simulation results and compare these to our previous findings. Finally, in Section 4.6 we draw a short conclusion and present an outlook for future research.

4.3 Material model

4.3.1 Two-phase coupled model of bone

In this subsection, we shortly repeat our material model used in our previous publications, as we did before in Ref. Stieve et al. (2022). The detailed derivation and explanation of all equations can be found in Ref. Blaszczyk and Hackl (2022). To model the spongy bone, we employ the following thermodynamic energy functional in the microscale domain Ω_{γ}

$$\begin{aligned} \Pi = & \int_{\Omega_b} \Psi_b(\boldsymbol{\varepsilon}, \mathbf{E}, \mathbf{B}) dV + \int_{\Omega_m} \Psi_m(\boldsymbol{\varepsilon}, \boldsymbol{\varepsilon}^i, \mathbf{E}, \mathbf{B}) + \mathcal{C} dV \\ & + \int_{\Omega_m} \int_t \Delta(\dot{\boldsymbol{\varepsilon}}^i, \dot{\mathbf{A}}) dt dV + \int_{\Omega} \Psi_g(\nabla \cdot \mathbf{A}) dV - W_{\text{ext}}. \end{aligned} \quad (4.1)$$

It consists of the energy densities Ψ_b and Ψ_m of both phases, a volume constraint \mathcal{C} , dissipation and gauge functionals (Δ and Ψ_g) and the potential of the generalized external forces W_{ext} . The main variables of the problem are the mechanical displacements \mathbf{u} , the electric scalar potential φ and the magnetic vector potential \mathbf{A} . Therefore, the three-dimensional problem consists of a total of seven degrees of freedom (DoFs). We then calculate the state variables mechanical strain $\boldsymbol{\varepsilon}$, electric field \mathbf{E} and magnetic flux density \mathbf{B} as

$$\boldsymbol{\varepsilon} = \frac{1}{2} (\nabla \mathbf{u} + \nabla^T \mathbf{u}), \mathbf{E} = -\nabla \varphi - \dot{\mathbf{A}} \text{ and } \mathbf{B} = \nabla \times \mathbf{A}. \quad (4.2)$$

Using this formulation, it follows from the Nabla product rules that two of the four Maxwell equations are already satisfied. We choose the following energy densities for the phases

$$\begin{aligned} \Psi_b &= \frac{1}{2} (\boldsymbol{\varepsilon} \cdot \mathbb{C}_b \cdot \boldsymbol{\varepsilon} - \mathbf{E} \cdot \boldsymbol{\xi}_b \cdot \mathbf{E} + \mathbf{B} \cdot \boldsymbol{\mu}_b^{-1} \cdot \mathbf{B}) - \mathbf{e}_b \cdot \boldsymbol{\varepsilon} \cdot \mathbf{E} \quad \text{and} \\ \Psi_m &= \frac{1}{2} ((\boldsymbol{\varepsilon} - \boldsymbol{\varepsilon}^i) \cdot \mathbb{C}_m \cdot (\boldsymbol{\varepsilon} - \boldsymbol{\varepsilon}^i) - \mathbf{E} \cdot \boldsymbol{\xi}_m \cdot \mathbf{E} + \mathbf{B} \cdot \boldsymbol{\mu}_m^{-1} \cdot \mathbf{B}). \end{aligned} \quad (4.3)$$

Both phases consist of quadratic energy terms for mechanical, electric and magnetic effects, resulting in a linear problem. We include a piezoelectric energy term for the cortical bone phase. In contrast, for the bone marrow phase we introduce an inelastic (i.e. viscous) strain $\boldsymbol{\varepsilon}^i$. The material tensors introduced in Equation (4.3) are the mechanical stiffness tensor \mathbb{C} , the permittivity tensor $\boldsymbol{\xi}$, the inverse permeability tensor $\boldsymbol{\mu}^{-1}$ and the piezoelectric tensor \mathbf{e}_b . In general, it is possible to use a different potential formulation by performing a Legendre transformation, switching between state and flux variables (and thus using e.g., the magnetic scalar potential instead). A detailed tabular list can be found in Ref. Lupascu et al. (2017). However, for our model, the present formulation is the most suitable, as it allows an easy inclusion of the electric dissipation and the full coupling of the Maxwell equations. The constraint function

$$\mathcal{C} = \lambda \text{tr}(\boldsymbol{\varepsilon}^i) \quad (4.4)$$

enforces volume conservation of the inelastic deformation, with the Lagrange multiplier λ . The dissipation function

$$\Delta = \frac{1}{2} (\boldsymbol{\mu}_v^{-1} |\dot{\boldsymbol{\varepsilon}}^i|^2 - \boldsymbol{\kappa} \mathbf{E}^2) \quad (4.5)$$

governs the evolution of the inelastic strain and the energy loss due to conduction. The latter satisfies Ohm's law $\mathbf{J} = \kappa \mathbf{E}$. Both parts of the dissipation only occur in the bone marrow phase. Here, we introduce the viscosity parameter $\mu_v^{-1} > 0$, the electric conductivity tensor $\kappa = \kappa_1 \mathbf{I}$, with the identity tensor \mathbf{I} , the electric conductivity $\kappa_1 > 0$ and the electric current density \mathbf{J} . The gauge function

$$\Psi_g = \frac{\gamma}{2} (\nabla \cdot \mathbf{A})^2 \quad (4.6)$$

introduces the numerical parameter γ and ensures, that we obtain a unique solution for the magnetic vector potential \mathbf{A} . Lastly, the potential of generalized external forces is

$$W_{\text{ext}} = \int_{\Omega} (\mathbf{f} \cdot \mathbf{u} - q_v \cdot \varphi + \mathbf{j}_v \cdot \mathbf{A}) dV + \int_{\partial\Omega} (\mathbf{t} \cdot \mathbf{u} - q_s \cdot \varphi + \mathbf{j}_s \cdot \mathbf{A}) dA. \quad (4.7)$$

Here, \mathbf{f} and \mathbf{t} are the mechanical volume and surface forces, q_v and q_s are the electric volume and surface charges and \mathbf{j}_v and \mathbf{j}_s are the volume and surface currents. In order to obtain the weak and strong form of the problem, the energy functional has to become stationary with respect to the main variables and internal variables. First, we calculate the evolution equation for the inelastic strain

$$\dot{\boldsymbol{\varepsilon}}^i = \mu_v \boldsymbol{\sigma}_{\text{dev}}, \quad (4.8)$$

with $\boldsymbol{\sigma}_{\text{dev}} = \boldsymbol{\sigma} - \frac{1}{3} \text{tr}(\boldsymbol{\sigma}) \mathbf{I}$ denoting the deviatoric part of the mechanical stress $\boldsymbol{\sigma}$. The remaining variational equation in the weak form reads

$$\int_{\Omega} (\boldsymbol{\sigma} \cdot \delta \boldsymbol{\varepsilon} - \mathbf{D} \cdot \delta \mathbf{E} + \mathbf{H} \cdot \delta \mathbf{B} - \mathbf{J} \cdot \delta \mathbf{A} + \gamma (\nabla \cdot \mathbf{A}) \cdot \delta (\nabla \cdot \mathbf{A})) dV - \delta W_{\text{ext}} = 0 \quad \forall \delta \mathbf{u}, \delta \varphi, \delta \mathbf{A}, \quad (4.9)$$

allowing us to obtain the flux quantities of our problem, which are the mechanical stress $\boldsymbol{\sigma}$, the electric displacement \mathbf{D} and the magnetic field strength \mathbf{H} . We note that it is also possible to derive the material tensors and the flux quantities by calculating the first and second derivatives of the energy densities with respect to the state variables. To obtain the strong form of the problem, we apply partial integration to each term, thus receiving

$$\begin{aligned} \nabla \cdot \boldsymbol{\sigma} + \mathbf{f} &= \mathbf{0} \text{ in } \Omega & \boldsymbol{\sigma} \cdot \mathbf{n} &= \mathbf{t} \text{ on } \partial\Omega \\ \nabla \cdot \mathbf{D} &= q_v \text{ in } \Omega & \mathbf{D} \cdot \mathbf{n} &= -q_s \text{ on } \partial\Omega \\ \nabla \times \mathbf{H} &= \dot{\mathbf{D}} + \mathbf{J} + \gamma \nabla (\nabla \cdot \mathbf{A}) + \mathbf{j}_v \text{ in } \Omega & \mathbf{H} \times \mathbf{n} &= \mathbf{j}_s - \gamma (\nabla \cdot \mathbf{A}) \mathbf{n} \text{ on } \partial\Omega \end{aligned} \quad (4.10)$$

where we recover the mechanical equilibrium condition, the two remaining Maxwell equations and boundary conditions, including the gauge. The normal vector pointing outwards is denoted as \mathbf{n} . We obtain equations containing the flux quantities and the external influences, which were introduced in Equation (4.7). The evolution equation of the inelastic strain (cf. Equation (4.8)) in Ω_m is part of the strong form as well. As a consequence from considering two phases, the strong form also includes the jump conditions

$$\begin{aligned} [[\boldsymbol{\sigma}]]_{\text{bm}} \cdot \mathbf{n} &= \mathbf{t}_{\text{bm}} \text{ on } \partial\Omega_{\text{bm}}, \\ [[\mathbf{D}]]_{\text{bm}} \cdot \mathbf{n} &= -q_{s,\text{bm}} \text{ on } \partial\Omega_{\text{bm}} \text{ and} \\ [[\mathbf{H}]]_{\text{bm}} \times \mathbf{n} &= \mathbf{j}_{s,\text{bm}} - \gamma [[\nabla \cdot \mathbf{A}]]_{\text{bm}} \mathbf{n} \text{ on } \partial\Omega_{\text{bm}} \end{aligned} \quad (4.11)$$

on the interface between the phases $\partial\Omega_{\text{bm}}$. The difference between the phases is denoted as $[[\cdot]]_{12} := (\cdot)_1 - (\cdot)_2$. The jump conditions describe the behavior of the flux quantities at the phase boundary, where a sudden change in material parameters may result in a sudden, discontinuous change of some components of the flux quantities. This can also be interpreted as the corresponding surface quantity at the phase boundary, in contrast to the external contributions in Equation (4.10).

Next, we discuss the formulation for the macroscopic problem. For the multiscale parts of the macroscopic model, we use the same equations (besides the evolution equation of the inelastic strain) derived for the microscale. The macroscale domain is $\Omega_{\mathbf{x}}$. In contrast to the microscale model, the main difference for these macroscale calculations is that instead of using material tensors as introduced in Equation (4.3), the flux quantities are now computed by using the microscopic RVE:

$$(\overline{\boldsymbol{\sigma}}, \overline{\mathbf{D}}, \overline{\dot{\mathbf{D}}}, \overline{\mathbf{H}}, \overline{\mathbf{J}}) = f_{\text{RVE}}(\overline{\boldsymbol{\varepsilon}}, \overline{\mathbf{E}}, \overline{\mathbf{B}}). \quad (4.12)$$

Here, we replace all microscale quantities by the corresponding macroscale quantities, denoted as $\overline{(\cdot)}$.

It remains the discussion of the scale transition. The Hill-Mandel conditions have to be fulfilled, guaranteeing energy conservation between the scales [Hill (1963, 1972); Labusch et al. (2019)]. We ensure that for the localization (macro-to-micro transition) by using periodic boundary conditions, as these are the most suitable for our problem and the results are independent of the relative geometry of the used RVE [Schröder (2000)]. For that purpose, in the implementation of the problem, all DoFs of nodes on opposite faces are linked and all corner nodes are fixed to prevent rigid body motions. The microscopic state variables consist of two parts, microscopic fluctuations (denoted as $\tilde{(\cdot)}$) and macroscopic contributions, which act as a load on the microscopic problem:

$$\tilde{(\cdot)}(\mathbf{x}, \mathbf{y}) = \tilde{(\cdot)}(\mathbf{y}) + \overline{(\cdot)}(\mathbf{x}), \text{ with } (\cdot) \in \{\boldsymbol{\varepsilon}, \mathbf{E}, \mathbf{B}\}. \quad (4.13)$$

To fulfill the Hill-Mandel conditions for the homogenization (micro-to-macro transition), we send back the volume averages of the flux quantities to the macroscopic scale, after solving the microscopic problem:

$$\overline{(\cdot)}(\mathbf{x}) = \frac{1}{\Omega} \int_{\Omega} \tilde{(\cdot)}(\mathbf{x}, \mathbf{y}) \, dV, \text{ with } (\cdot) \in \{\boldsymbol{\sigma}, \mathbf{D}, \dot{\mathbf{D}}, \mathbf{H}, \mathbf{J}\}. \quad (4.14)$$

4.3.2 Inclusion of a surrounding medium

In our previous contributions, we did our calculations of the bone model without any surroundings. While this is sufficient for purely mechanical modeling of specimen, in electromagnetism depending on the application the surrounding medium may have to be considered in the model as well, as the electromagnetic fields also exist outside the modeled body [Yang and Dayal (2011)]. The importance of including the surrounding medium strongly depends on the problem the model tries to solve. For example, when modeling a MEMS (micro-electro-mechanical system) beam, it is usually required to model the surrounding medium as well as the specimen. The reasons for this are that, first, the electric field is applied from the outside and second, when the beam deforms due to the electric field, the field

itself strongly changes, which can contribute even more to the deformation. The problem is therefore strongly coupled and non-linear [Hannot (2010); Pustan et al. (2014)]. Thus, for such applications, the surrounding medium cannot be neglected. In contrast, for some problems the outside medium only has a minor effect on the fields inside the modeled body.

In this contribution, we investigate to what extent the overall simulation results are influenced by the inclusion of a surrounding medium in the model. While the formulation is valid for all space, only the region near the specimen is of interest [Yang and Dayal (2011)]. Furthermore, in computational modeling, the limitation of a finite domain occurs. We address this in the result section by performing a convergence study using boundary boxes which differ in size. We assume the bone specimen to be surrounded by air, with the subscript $(\cdot)_o$ denoting the affiliation to the outside medium. Then, in the outside domain Ω_o all mechanical DoFs vanish and we reduce our energy functional to the following form

$$\Pi = \int_{\Omega_o} \Psi_o(\mathbf{E}, \mathbf{B}) dV + \int_{\Omega_o} \Psi_g(\nabla \cdot \mathbf{A}) dV - W_{\text{ext}}. \quad (4.15)$$

The energy density Ψ_o is given as

$$\Psi_o = \frac{1}{2}(-\mathbf{E} \cdot \boldsymbol{\xi}_o \cdot \mathbf{E} + \mathbf{B} \cdot \boldsymbol{\mu}_o^{-1} \cdot \mathbf{B}). \quad (4.16)$$

It should be noted here, that in general it is possible to adjust the model to describe another surrounding medium as well, however this then also may require a different energy formulation. Other than air (cf. Ref. Güzelsu and Saha (1981)), in practice, experiments with bone specimen are also often done in a water tank (cf. Ref. Hosokawa and Otani (1997)), which in return can be included by considering for example, the Helmholtz equation for fluid pressure. Examples are given in Refs. Gilbert et al. (2021); Blaszczyk et al. (2021a,b). From Equation (4.16), we calculate the weak form of the problem as

$$\int_{\Omega_o} (-\mathbf{D} \cdot \delta \mathbf{E} + \mathbf{H} \cdot \delta \mathbf{B} + \gamma(\nabla \cdot \mathbf{A}) \cdot \delta(\nabla \cdot \mathbf{A})) dV - \delta W_{\text{ext}} = 0 \quad \forall \delta \varphi, \delta \mathbf{A}. \quad (4.17)$$

Again using integration by parts, we obtain the strong form of the problem

$$\begin{aligned} \nabla \cdot \mathbf{D} &= q_v \text{ in } \Omega_o & \mathbf{D} \cdot \mathbf{n} &= -q_s \text{ on } \partial\Omega_o \\ \nabla \times \mathbf{H} &= \dot{\mathbf{D}} + \mathbf{J} + \gamma \nabla(\nabla \cdot \mathbf{A}) + \mathbf{j}_v \text{ in } \Omega_o & \mathbf{H} \times \mathbf{n} &= \mathbf{j}_s - \gamma(\nabla \cdot \mathbf{A})\mathbf{n} \text{ on } \partial\Omega_o, \end{aligned} \quad (4.18)$$

consisting of the two remaining Maxwell equations and boundary conditions, including the gauge. The jump conditions between the outside domain and the interior of the model (denoted by i) are

$$[[\mathbf{D}]]_{oi} \cdot \mathbf{n} = -q_{s,oi} \text{ on } \partial\Omega_{oi} \text{ and } [[\mathbf{H}]]_{oi} \times \mathbf{n} = \mathbf{j}_{s,oi} - \gamma [[\nabla \cdot \mathbf{A}]]_{oi} \mathbf{n} \text{ on } \partial\Omega_{oi}. \quad (4.19)$$

4.3.3 Differentiation of macroscale phases

Previously, we used our two-phase model to describe the microscale at any macroscopic point. However, real human bones are more complicated (cf. Ref. Locke (2004)). Figure

4.1 shows the cross section of a human bone. Our two-phase model aims to capture the structure of trabecular (spongy) bone, which is a mixture of cortical bone and bone marrow and mostly found at the ends of long bones. However, as can be seen in the image, the boundary of bone consists of cortical bone. Additionally, in the middle region of the long axis, bone marrow is surrounded by a layer of spongy bone, with cortical bone forming the closure.

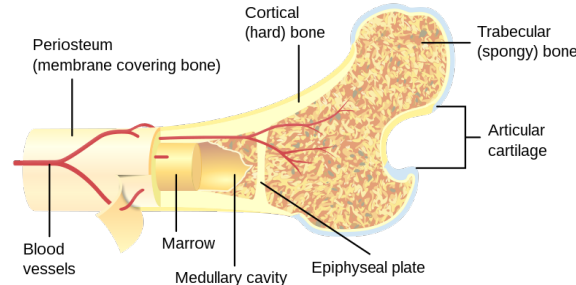


Figure 4.1: Cross section of human bone, from Ref. Pbrks/Wikimedia (2022).

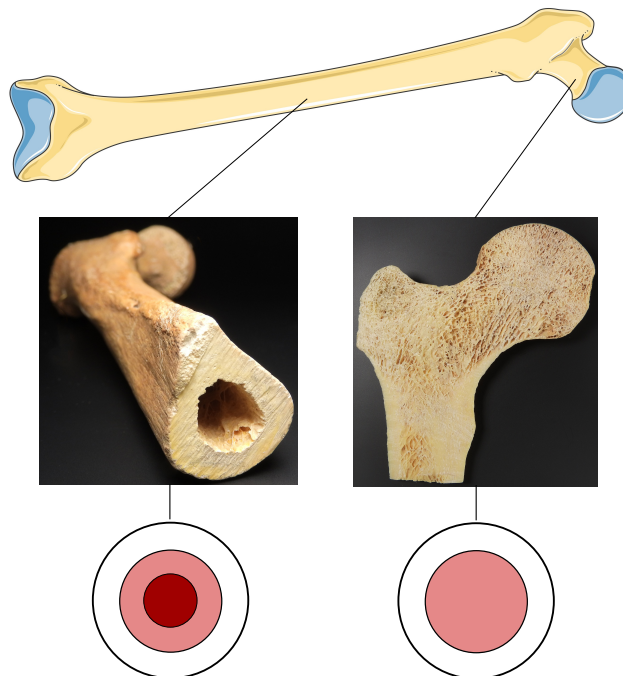


Figure 4.2: Schematic comparison of the structure of long human bones in the center and at its endings with corresponding cross section models (white: cortical bone, light red: spongy bone (phase mixture), dark red: bone marrow), image composed from Refs. Laboratoires Servier (2022); Klimešová (2022a,b).

For these reasons, we decided to also perform simulations where we split the radial part of our macroscopic model into different parts and apply the corresponding material model depending on the model part, therefore increasing the applicability of our simulations. Figure 4.2 compares the structure of long human bones, for example, the femur bone, in the center and at the endings of bone and shows possible radial distributions of the material model phases. It should be noted here that in this work, we focus on the center section of bone by using our cylinder model. Therefore we chose the split of phases as shown in the left side of the image. For future work, an even finer differentiation would be possible, by for example, also splitting the model in axial direction as shown in the image, however this may require more complicated meshes of both the femur bone and the outside domain.

4.4 Numerical implementation

To solve the previous derived equations numerically, we applied a standard FE ansatz to Eq. (4.9) and Eq. (4.17), respective. Details regarding the resulting matrix system can be found in Ref. Blaszczyk and Hackl (2022). For the time integration, we use the JWH- α -scheme from Ref. Kadapa et al. (2017) with the numerical parameter $\rho_\infty = 0.5$. For our programm, each node has seven DoFs.

We use a cylinder (length: 30 cm, diameter: 3 cm) to model the bone. To include the outside medium, we created a boundary box around it with an extra length of 3 cm in each direction (i.e. the total length of the model in longitudinal direction is 36 cm). We set the mechanical displacement to zero at nodes whose elements are only affiliated to the surrounding medium. Additionally, we set all nodes of the cylinder bases to have no mechanical displacement. For the electric scalar potential, it is sufficient to set a single node at the corner of the boundary box to zero. In contrast, the magnetic vector potential needs additional restrictions to prevent the equivalent of "rigid body motions". For this reason, we set the magnetic vector potential to zero at three different corner nodes. Further details and different example configurations to prevent these issues can be found in Ref. Semenov et al. (2006). Figure 4.3 shows a schematic representation of our model, the used boundary conditions and the cylinder part, where the load is applied. The mechanical displacement is applied on the surface in the middle section of the cylinder within a length of 4 cm and an angle of 90° .

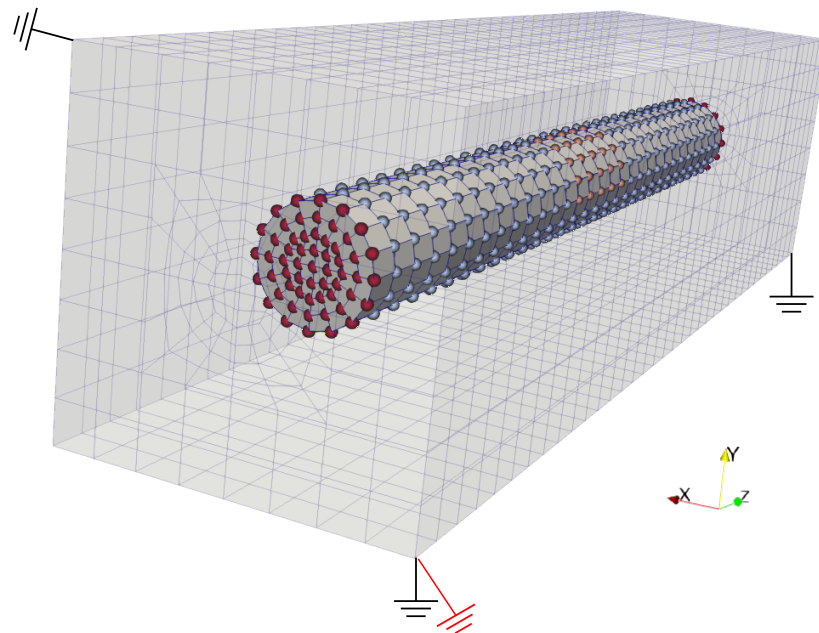


Figure 4.3: Boundary conditions of the model. For the cylinder model nodes, red: $\mathbf{u} = \mathbf{0}$, light orange: mechanical displacement in x -direction applied, blue-gray: no directions restricted. For the outside box corner nodes, black grounding: $\mathbf{A} = \mathbf{0}$, red grounding: $\varphi = 0$.

Besides the applied mechanical displacement, no external contributions affect the model, that is the external contributions in Eq. (4.7) are set to zero. Furthermore, the surface quantities on the right-hand sides in Eq. (4.11) and Eq. (4.19) are set to zero. Therefore, the jump conditions are fulfilled automatically, similarly to homogenous Neumann boundary condition and no additional implementation effort was required compared to standard FEM.

For the implementation, we wrote a computer program in the programming language Julia [Bezanson et al. (2022)], using the FE toolbox FERRITE [Carlsson and Ekre (2022)] and the package COHERENTSTRUCTURES [de Diego et al. (2022)]. We used the software GMSH [Geuzaine and Remacle (2022)] to create our meshes. For the postprocessing and the creation of the result images, we used the software PARAVIEW [Kitware Inc. (2022)].

4.5 Simulation results

In this section we show numerical results for different simulation cases. Table 4.1 shows the used material parameters for the different phases and the literature, where the numerical values can be found. Other parameters are of rather academic nature and influence the results only marginally. The gauge penalty parameter is $\gamma = 1.0 \text{ s}^2 \text{ A}^2/(\text{kg m})$. We set up the boundary conditions as shown in Figure 4.3 and apply the mechanical displacement $u_x = u_{\max} \cdot a(t)$ in x -direction, with $u_{\max} = 2 \cdot 10^{-6} \text{ m}$ and the time increment $\Delta_t = 1 \cdot 10^{-2} \text{ s}$. We calculate 100 time steps by changing the amplitude over time as shown in Figure 4.4. Additional details can be found in Ref. Blaszczyk and Hackl (2022).

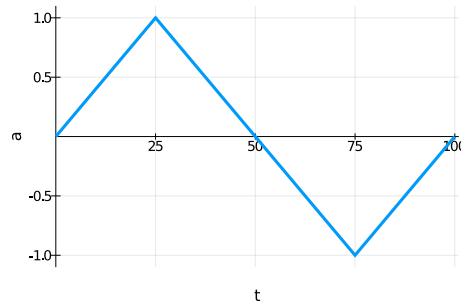


Figure 4.4: Amplitude of the displacement function a against the time step t .

4.5.1 Influence of the surrounding medium air compared to previous results

To examine the influence of the introduced improvements, we created the four models (i) previously used cylinder mesh, (ii) cylinder mesh with air, (iii) finer cylinder mesh with air and (iv) cylinder mesh with air and wider boundary box (6 cm instead of 3 cm in each direction) and compare the results of the magnetic field strength. Table 4.2 shows the four used meshes and provides the number of nodes and elements in each mesh. We note that the first, second and fourth model have the same mesh resolution for the cylinder, the difference is only the inclusion of a surrounding medium, the size of the boundary box and the improved boundary conditions. For all models, we assume that the whole cylinder domain is filled with the spongy bone phase mixture, where we use a RVE with $\rho_b = 29.5\%$. Figure 4.5 shows the resulting magnetic field strength \mathbf{H} after 50 time steps for the four different cases. Figure 4.6 instead shows only a comparison between the first two meshes with an adjusted color scale to highlight the differences of the results between these two models. To increase the visibility and comparability of the results, in these two images we show only the cylinder part of the models without the boundary box.

Material parameter	Cortical bone	Bone marrow	Air	
Young's modulus [Steeb (2010)]	E	22.0 GPa	2.0 GPa	0 GPa
Poisson's ratio [Steeb (2010)]	ν	0.32	-	0
Permittivity [Güzelsu and Saha (1981)]	ξ_1	$8.85 \cdot 10^{-12}$ F/m	$8.85 \cdot 10^{-12}$ F/m	$8.85 \cdot 10^{-12}$ F/m
Permeability [Güzelsu and Saha (1981)]	μ_c	$1.257 \cdot 10^{-6}$ H/m	$1.257 \cdot 10^{-6}$ H/m	$1.257 \cdot 10^{-6}$ H/m
Piezoelectric coefficient [Fukada and Yasuda (1957)]	e_{15}	$3.0 \cdot 10^{-3}$ A s/m ²	0 A s/m ²	0 A s/m ²
Electric conductivity	κ_1	0 S/m	$1.0 \cdot 10^4$ S/m	0 S/m
Viscosity parameter	μ_v	0 s/GPa	$0.5 \cdot \Delta_t$ s/GPa	0 s/GPa

Table 4.1: Default material parameters.

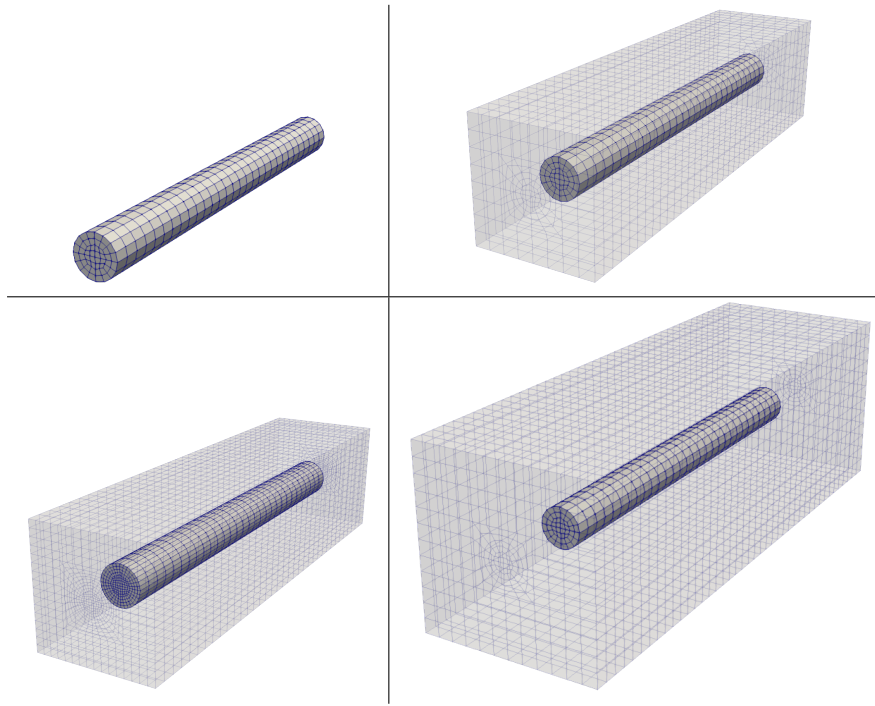


Table 4.2: Comparison of finite element meshes used for calculating simulation results. Top left: previously used cylinder mesh (1767 nodes, 1440 elements), top right: cylinder mesh with air (5365 nodes, 4608 elements), bottom left: finer cylinder mesh with air (20165 nodes, 18432 elements), bottom right: cylinder mesh with air and wider boundary box (10019 nodes, 8736 elements).

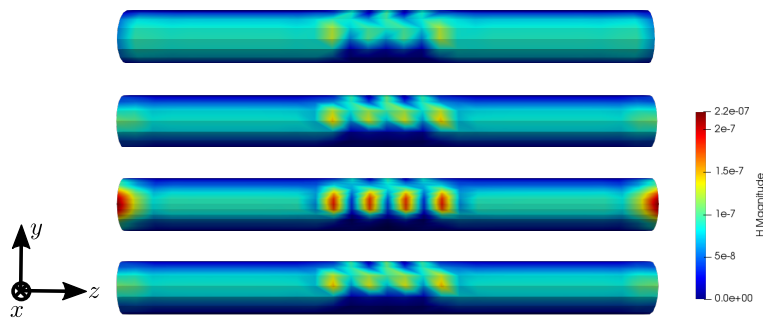


Figure 4.5: Simulation results for the four used meshes (only cylinder part shown): magnetic field strength \mathbf{H} [A/m], at $t = 50$. From top to bottom: previous used cylinder mesh, cylinder mesh with air, finer cylinder mesh with air, cylinder mesh with air and wider boundary box.

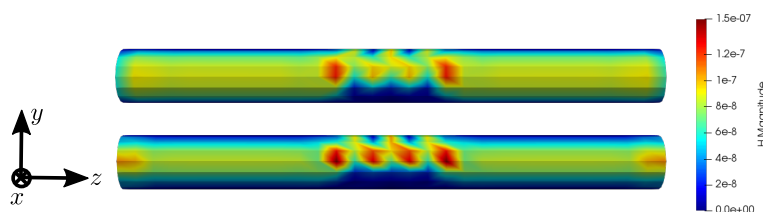


Figure 4.6: Simulation results with adjusted color scale for the previous used cylinder mesh (top) and cylinder mesh with air (bottom, only cylinder part shown): magnetic field strength \mathbf{H} [A/m], at $t = 50$.

Comparing the first two models, the magnetic field strength \mathbf{H} is increased by about 15% in the middle section of the cylinder. The finer mesh shows a slight additional increase of \mathbf{H} especially in the middle section and at the cylinder boundary, but the qualitative distribution is very similar. The results for the mesh with the wider boundary box (fourth model) are nearly identical to the mesh with the same resolution but smaller boundary box (second model).

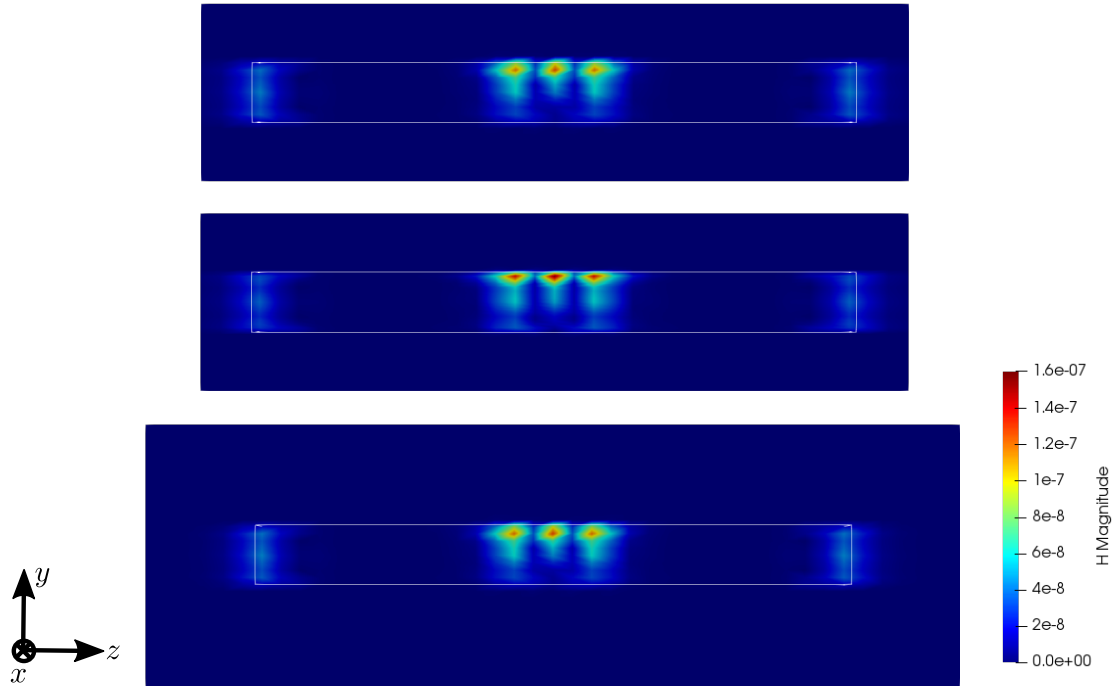


Figure 4.7: Simulation results for model two to four: magnetic field strength \mathbf{H} [A/m], at $t = 50$. Slice of plane with x -normal vector in the middle of the cylinder. The white line shows the boundary of the cylinder.

To further investigate the effect of the boundary box on the results, we created slices through the planes in normal x -direction (Figure 4.7) and z -direction (Figure 4.8) in the middle of the cylinder. The magnetic field strength is significantly reduced at the edges of the boundary box both for the usual and fine mesh. Both images show no visible differences between model two and four, while the magnetic field strength is slightly increased for the finer mesh (shown in the middle). The magnetic field decays rapidly at the cylinder boundary over the length of one to two elements. Therefore, for the shown simulation setup, the small boundary box with three elements in each direction allows the proper decay of the electromagnetic fields and is already sufficient to capture the effects of a surrounding medium, which has a noticeable impact of about 15% on the final results.

Finally, we investigate the results of the first two models at the cylinder bases to compare the used boundary conditions, as shown in Figure 4.9. At the endings of the cylinder, the differences between the models are greater compared to the middle section. On the left side, the old model shows results, which are up to one magnitude higher than the new solution, whereas the resulting magnetic field strength is reduced on the right side. In contrast, our new model shows a symmetric behavior. The reason for this is likely due to the magnetic boundary conditions used in the previous simulations (restricting the vector potential at the cylinder base, cf. Ref. Blaszczyk and Hackl (2022)). Thus, the magnetic field strength at the left ending of the cylinder model was likely overestimated in our past calculations. However, the overall results were only marginally influenced. Moving inwards only one

element in longitudinal direction, we received nearly identical results on both ends of the cylinder.

The calculation for the first two models took about 8 h, making the inclusion of the boundary box neglectable regarding computation time, as in that part FE^2 is not used. The fine mesh needed about 5 days of computation time, a big trade-off for slightly more accurate results. Finally, the mesh with a wider boundary box required one and a half days of computation time. All these simulations were done on a computer cluster using parallelization.

4.5.2 Results for the three-way split cylinder model

As a second example, we now combine the previous improvements of including the surrounding medium with the altered boundary conditions and the differentiation of macroscale phases within the cylinder. To differentiate between the different bone phases, we divided the radius of the cylinder base into three equally long parts and apply the phases bone marrow, cancellous bone, that is, mixed phase (FE^2 model) and cortical bone, respectively, from the center to the cylinder boundary (Figure 4.10). The split only depends on the distance from the center but not the number of elements in between. Additionally, we ensured that the phase boundary does not lie within an element. This way, we prevent the introduction of a mesh dependence (i.e. increasing the number of elements in the mesh does not cause a change in volume fraction for one of the phases). We note, that in this model only in the part, where we assume cancellous bone, the FE^2 is applied, whereas the calculations reduce to single scale FEM in all other parts.

To investigate the effect of osteoporosis on the results, we created six RVEs with different volume percentage of cortical bone ρ_b , which we use for the spongy bone phase in the model. These range from $\rho_b = 5.3\%$ (RVE 1, very degenerated bone) to $\rho_b = 29.5\%$ (RVE 6, healthy bone), with about 5% intervals in between (cf. Ref. Blaszczyk and Hackl (2022)). Figure 4.11 shows the resulting magnetic field strength at timestep $t = 50$ of the simulations by plotting the transition between cortical and spongy bone phases, which is the area where we receive the highest magnitudes of the field.

Similarly to our previous results in Ref. Blaszczyk and Hackl (2022), the magnetic field strength is decreasing for lower volume percentages of cortical bone. While the difference between RVE 5 and 6 is small, the field drastically decreases for lower values of ρ_b . In Figure 4.11, we show the magnetic field strength at the interface between cancellous and cortical bone, as the magnitude is the highest in this area. We note that the absolute values of the resulting field is decreased compared to the previous results. One possible reason for this effect could be the insulating properties of the outer shell modeled as cortical bone phase, that is, no current density is present to contribute to the resulting magnetic field.

4.6 Conclusion

We improved important aspects of the bone model. After shortly reintroducing the used material model, we derived the formulation for the inclusion of air as a surrounding medium.

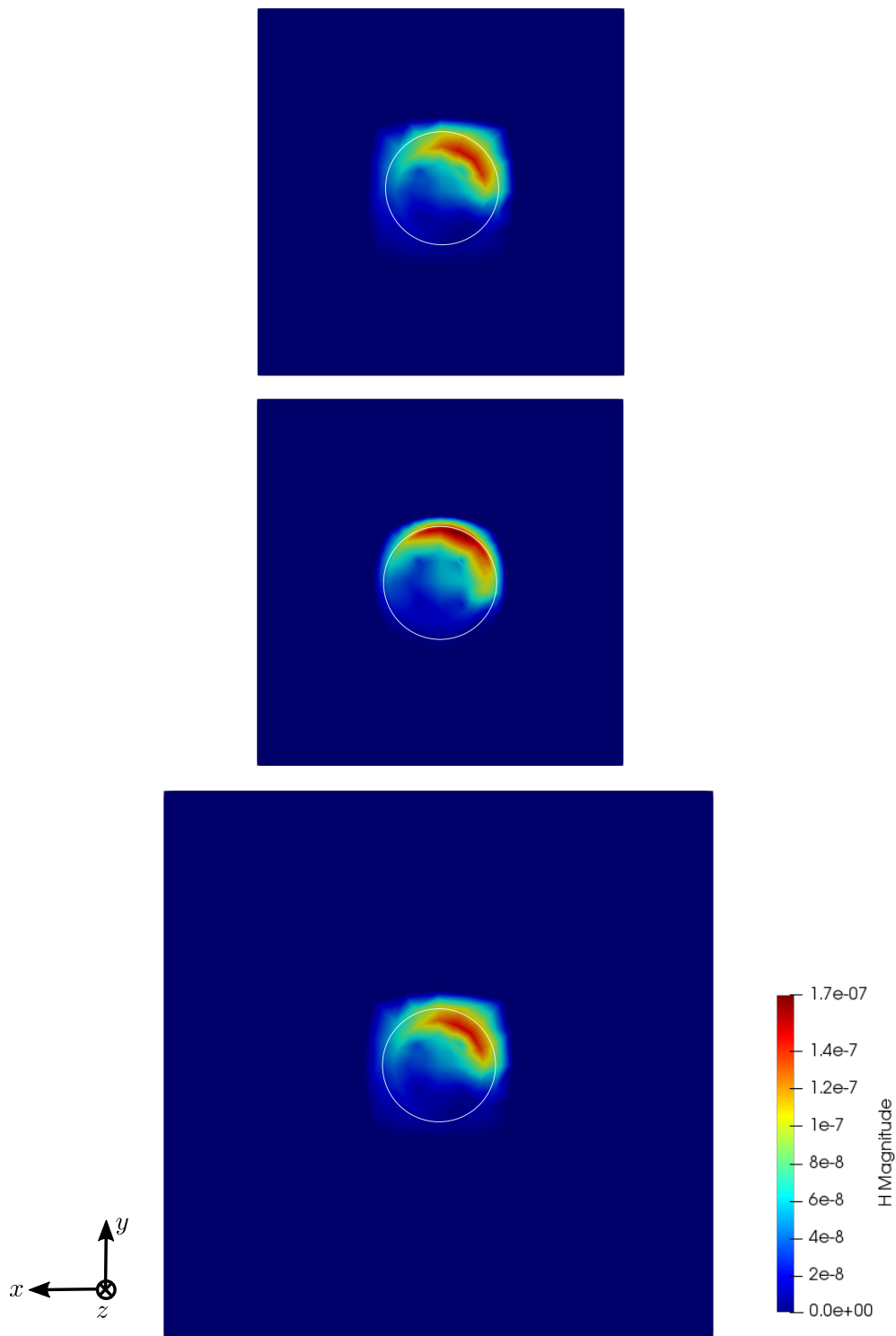


Figure 4.8: Simulation results for model two to four: magnetic field strength \mathbf{H} [A/m], at $t = 50$. Slice of plane with z -normal vector in the middle of the cylinder. The white line shows the boundary of the cylinder.

Additionally, we explained the physiological reasons for the split into different regions. We discussed the numerical methods and implementation, before showing simulation results.

We used the cylinder model to compare our new results to previous ones. The coarser model with a boundary box shows a magnetic field strength increase of 15% in the middle section of the cylinder, where the magnitude of the field is the highest. While even finer meshes leads

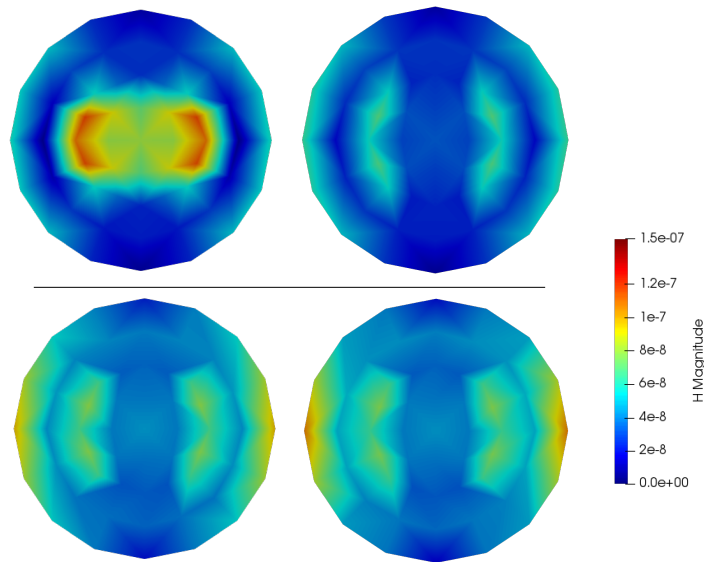


Figure 4.9: Simulation results: magnetic field strength H [A/m], at $t = 50$. Left and right cylinder base of previous model (top) and model including surrounding medium (bottom).

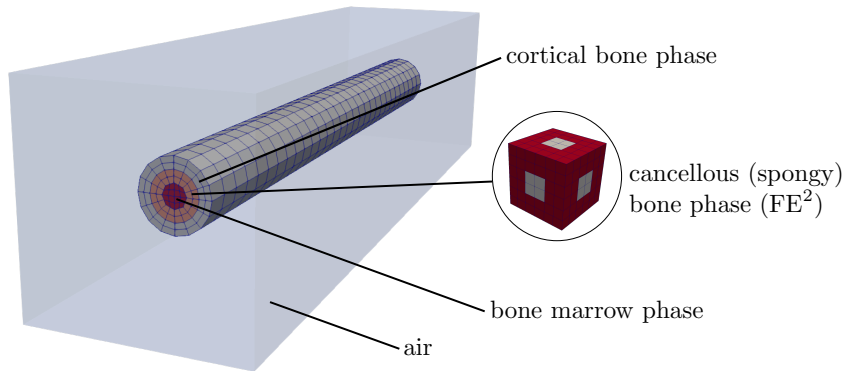


Figure 4.10: Cylinder model with surrounding medium and differentiation between the macroscale phases bone marrow, cancellous (spongy) bone and cortical bone (from the center to the cylinder boundary).

to a further increase of magnetic field strength, the calculation time increases drastically. Balancing accuracy and computation speed, the coarser mesh with a small boundary box containing three elements in each direction yields adequate results. Increasing the size of the boundary box shows no visible differences in the results. Thus, using a small boundary box is likely sufficient to capture the desired effects and is therefore necessary to obtain precise results, but can be neglected if an error of about 15% is acceptable. Furthermore, we improved the used boundary conditions. Our new results are more symmetric and realistic compared to the previous model. In addition, we have shown how the macroscopic model can be split into different parts representing different phases of the bone. Compared to our previous findings, the simulation results show a similar qualitative behavior of RVEs with different volume percentages of cortical bone phase.

For further development of the model, different RVEs could be used to investigate the effect of the chosen RVE geometry and mesh resolution on the simulation results. Additionally, the orientation of the used RVEs could be varied to account for anisotropies in real bones. A different surrounding medium, for example, water, could be included in the model.

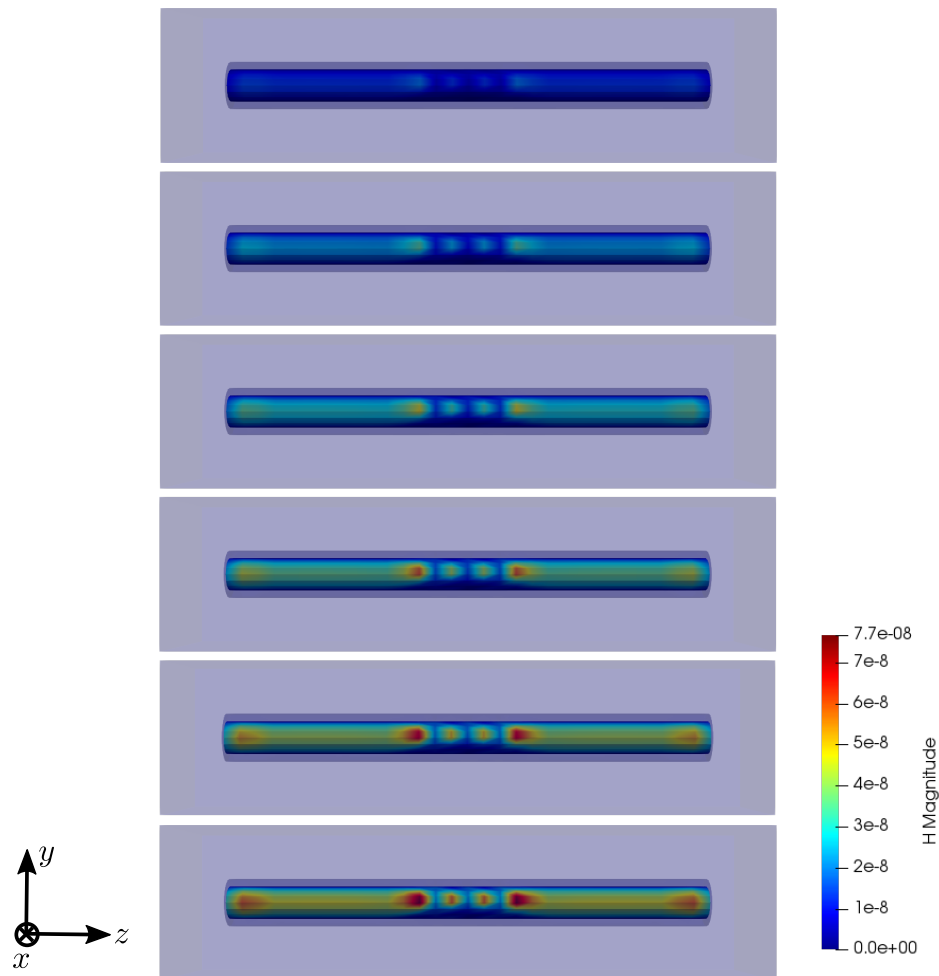


Figure 4.11: Simulation results for the RVEs 1 (top) to 6 (bottom) for three-way split cylinder macroscopic model: magnetic field strength \mathbf{H} [A/m], at $t = 50$.

Nédélec functions could be used to resolve discontinuities along surfaces and therefore improve the numerical performance of the model. Combined with that, the discontinuous Galerkin method could be used to perform simulations on unstructured meshes with very good computation times. Here, the bone geometry could easily be inserted into a box modeling the surrounding medium, without the need to fit the mesh resolutions of the different parts. This is an important advantage for practical usage of very complex real bone geometries from, for example, CT scans. Wave propagation in bone could be investigated and the model could be extended to soft tissues, using a finite strain formulation. Finally, the long term ambition of our research is the comparison of our results to experimental data obtained from real bones.

Code Availability

The program used to produce simulation results is mainly written in Julia, using the Open-Source Ferrite.jl toolbox. Code samples from the author were made public and can be found at Github: <https://github.com/blaszm>.

Bibliography

- [Abiodun et al. 2018] ABIODUN, O. I. ; JANTAN, A. ; OMOLARA, A. E. ; DADA, K. V. ; MOHAMED, N. A. ; ARSHAD, H.: State-of-the-art in artificial neural network applications: A survey. In: *Heliyon* 4 (2018), no. 11, pp. e00938
- [Amato et al. 2013] AMATO, F. ; LÓPEZ, A. ; PEÑA-MÉNDEZ, E. M. ; VAÑHARA, P. ; HAMPL, A. ; HAVEL, J.: Artificial neural networks in medical diagnosis. In: *Journal of applied biomedicine* 11 (2013), no. 2, pp. 47–58
- [Amini et al. 2016] AMINI, Y. ; FATEHI, P. ; HESHMATI, M. ; PARANDVAR, H. J. C. S.: Time domain and frequency domain analysis of functionally graded piezoelectric harvesters subjected to random vibration: Finite element modeling. In: *Composite Structures* 136 (2016), pp. 384–393
- [Aziz et al. 2014] AZIZ, I. ; ISLAM, S. ul ; KHAN, F.: A new method based on Haar wavelet for the numerical solution of two-dimensional nonlinear integral equations. In: *Journal of Computational and Applied Mathematics* 272 (2014), pp. 70–80
- [Bahrammirzaee 2010] BAHRAMMIRZAEI, A.: A comparative survey of artificial intelligence applications in finance: artificial neural networks, expert system and hybrid intelligent systems. In: *Neural Computing and Applications* 19 (2010), no. 8, pp. 1165–1195
- [de Bakker et al. 2017] BAKKER, C. M. J. ; TSENG, W.-J. ; LI, Y. ; ZHAO, H. ; LIU, X. S.: Clinical evaluation of bone strength and fracture risk. In: *Current osteoporosis reports* 15 (2017), pp. 32–42
- [Balzani et al. 2014] BALZANI, D. ; SCHEUNEMANN, L. ; BRANDS, D. .. ; SCHRÖDER, J.: Construction of two-and three-dimensional statistically similar RVEs for coupled micro-macro simulations. In: *Computational Mechanics* 54 (2014), pp. 1269–1284
- [Bao 2005] BAO, M.: *Analysis and design principles of MEMS devices*. Elsevier, 2005
- [Bartel et al. 2018] BARTEL, T. ; KIEFER, B. ; BUCKMANN, K. ; MENZEL, A.: A finite-element framework for the modelling and simulation of phase transforming magnetic solids using energy relaxation concepts. In: *PAMM* 18 (2018), no. 1, pp. e201800415
- [Bassegy and Ramsdale 1994] BASSEY, E. J. ; RAMSDALE, S. J.: Increase in femoral bone density in young women following high-impact exercise. In: *Osteoporosis international* 4 (1994), pp. 72–75
- [Bathe 2006] BATHE, K.-J.: *Finite element procedures*. Klaus-Jürgen Bathe, 2006

- [Berenger 1994] BERENGER, J.-P.: A perfectly matched layer for the absorption of electromagnetic waves. In: *Journal of computational physics* 114 (1994), no. 2, pp. 185–200
- [Betts et al. 2013] BETTS, J.G. ; DESAIX, P. ; JOHNSON, E. ; JOHNSON, J.E. ; KOROL, O. ; KRUSE, D.H. ; POE, B. ; WISE, J.A. ; WOMBLE, M. ; YOUNG, K.A.: *Anatomy and Physiology*. OpenStax, 2013. – ISBN 9781947172807
- [Bezanson et al. 2022] BEZANSON, J. ; EDELMAN, A. ; KARPINSKI, S. ; SHAH, V. B.: *The Julia Programming Language*. <https://julialang.org/>. Version: 2022
- [Biot 1956a] BIOT, M. A.: Theory of Propagation of Elastic Waves in a Fluid-Saturated Porous Solid. I. Low-Frequency Range. In: *The Journal of the Acoustical Society of America* 28 (1956), no. 2, pp. 168–178
- [Biot 1956b] BIOT, M. A.: Theory of Propagation of Elastic Waves in a Fluid-Saturated Porous Solid. II. Higher Frequency Range. In: *The Journal of the Acoustical Society of America* 28 (1956), no. 2, pp. 179–191
- [Blake and Fogelman 2007] BLAKE, G. M. ; FOGELMAN, I.: Role of dual-energy X-ray absorptiometry in the diagnosis and treatment of osteoporosis. In: *Journal of Clinical Densitometry* 10 (2007), no. 1, pp. 102–110
- [Blaszczyk et al. 2021a] BLASZCZYK, M. ; GILBERT, R. P. ; HACKL, K.: The effective equations for the ultrasonic response of wet cortical bone. In: *Mathematical Methods in the Applied Sciences* 44 (2021), no. 11, pp. 9096–9109
- [Blaszczyk et al. 2021b] BLASZCZYK, M. ; GILBERT, R. P. ; HACKL, K.: An effective model for cancellous bone with a viscous interstitial fluid. In: *Applicable Analysis* (2021), pp. 1–12
- [Blaszczyk and Hackl 2021a] BLASZCZYK, M. ; HACKL, K.: A fully coupled two-phase bone material model. In: *PAMM* 20 (2021), no. 1, pp. e202000144
- [Blaszczyk and Hackl 2021b] BLASZCZYK, M. ; HACKL, K.: Simulations of a multiscale bone material model. In: *PAMM* 21 (2021), no. 1, pp. e202100052
- [Blaszczyk and Hackl 2022] BLASZCZYK, M. ; HACKL, K.: Multiscale modeling of cancellous bone considering full coupling of mechanical, electric and magnetic effects. In: *Biomechanics and Modeling in Mechanobiology* 21 (2022), no. 1, pp. 163–187
- [Blender Foundation 2021] BLENDER FOUNDATION: *Blender*. <https://www.blender.org/>. Version: 2021
- [Boccaccio et al. 2011] BOCCACCIO, A. ; BALLINI, A. ; PAPPALETTERE, C. ; TULLO, D. ; CANTORE, S. ; DESIATE, A.: Finite element method (FEM), mechanobiology and biomimetic scaffolds in bone tissue engineering. In: *International journal of biological sciences* 7 (2011), no. 1, pp. 112–132

- [Boettinger et al. 2002] BOETTINGER, W. J. ; WARREN, J. A. ; BECKERMANN, C. ; KARMA, A.: Phase-field simulation of solidification. In: *Annual review of materials research* 32 (2002), no. 1, pp. 163–194
- [Buchanan and Gilbert 2007] BUCHANAN, J. ; GILBERT, R. P.: Determination of the parameters of cancellous bone using high frequency acoustic measurements. In: *Mathematical and Computer Modelling* 45 (2007), pp. 281–308
- [Buckmann et al. 2019] BUCKMANN, K. ; KIEFER, B. ; BARTEL, T. ; MENZEL, A.: Simulation of magnetised microstructure evolution based on a micromagnetics-inspired FE framework: application to magnetic shape memory behaviour. In: *Arch. Appl. Mech.* 89 (2019), no. 6, pp. 1085–1102
- [Buffa and Hiptmair 2003] BUFFA, A. ; HIPTMAIR, R.: Galerkin boundary element methods for electromagnetic scattering. In: *Topics in computational wave propagation*. Berlin, Heidelberg : Springer, 2003, pp. 83–124
- [Busch-Vishniac 1998] BUSCH-VISHNIAC, I. J.: *Electromechanical sensors and actuators*. Springer Science & Business Media, 1998
- [Cahn and Allen 1977] CAHN, J. W. ; ALLEN, S. M.: A microscopic theory for domain wall motion and its experimental verification in Fe-Al alloy domain growth kinetics. In: *Le Journal de Physique Colloques* 38 (1977), no. C7, pp. C7–51
- [Cahn and Hilliard 1958] CAHN, J. W. ; HILLIARD, J. E.: Free energy of a nonuniform system. I. Interfacial free energy. In: *The Journal of chemical physics* 28 (1958), no. 2, pp. 258–267
- [Carlsson and Ekre 2022] CARLSSON, K. ; EKRE, F.: *Ferrite.jl: A simple finite element toolbox written in Julia (previously known as JuAFEM.jl)*. <https://ferrite-fem.github.io/Ferrite.jl/stable/>. Version: 2022
- [Castaneda and Suquet 1997] CASTANEDA, P. P. ; SUQUET, P.: Nonlinear composites. In: *Advances in applied mechanics* 34 (1997), pp. 171–302
- [Chae et al. 2018] CHAE, I. ; JEONG, C. K. ; OUNAIES, Z. ; KIM, S. H.: Review on electromechanical coupling properties of biomaterials. In: *ACS Applied Bio Materials* 1 (2018), no. 4, pp. 936–953
- [Chaffey and Austin 2002] CHAFFEY, J. P. ; AUSTIN, M.: Analytical modeling of the electromechanical coupling of cantilever beams. In: *Smart Structures, Devices, and Systems* Bd. 4935 SPIE, 2002, pp. 86–93
- [Chamekh et al. 2008] CHAMEKH, A. ; BEL HADJ SALAH, H. ; HAMBALI, R.: Inverse technique identification of material parameters using finite element and neural network computation. In: *The International Journal of Advanced Manufacturing Technology* 44 (2008), no. 1, pp. 173

- [Chao et al. 2002] CHAO, T. Y. ; CHOW, W. K. ; KONG, H.: A review on the applications of finite element method to heat transfer and fluid flow. In: *International Journal on Architectural Science* 3 (2002), no. 1, pp. 1–19
- [Chen et al. 2018] CHEN, H. ; GILBERT, R. P. ; GUYENNE, P.: A Biot model for the determination of material parameters of cancellous bone from acoustic measurements. In: *Inverse Problems* 34 (2018), no. 8, pp. 085009
- [Chen 2002] CHEN, L.-Q.: Phase-field models for microstructure evolution. In: *Annual review of materials research* 32 (2002), no. 1, pp. 113–140
- [Chen et al. 2019] CHEN, Y. ; VASIUKOV, D. ; GÉLÉBART, L. ; PARK, C. H.: A FFT solver for variational phase-field modeling of brittle fracture. In: *Computer Methods in Applied Mechanics and Engineering* 349 (2019), pp. 167–190
- [Chiu et al. 2006] CHIU, J.-S. ; LI, Y.C. ; YU, F.C. ; WANG, Y.F.: Applying an artificial neural network to predict osteoporosis in the elderly. In: *Studies in health technology and informatics* 124 (2006), pp. 609–14
- [Christen et al. 2010] CHRISTEN, D. ; WEBSTER, D. J. ; MÜLLER, R.: Multiscale modelling and nonlinear finite element analysis as clinical tools for the assessment of fracture risk. In: *Philosophical Transactions of the Royal Society A: Mathematical, Physical and Engineering Sciences* 368 (2010), no. 1920, pp. 2653–2668
- [Clynes et al. 2020] CLYNES, M. A. ; HARVEY, N. C. ; CURTIS, E. M. ; FUGGLE, N. R. ; DENNISON, E. M. ; COOPER, C.: The epidemiology of osteoporosis. In: *British medical bulletin* (2020)
- [Cockburn 2003] COCKBURN, B.: Discontinuous galerkin methods. In: *ZAMM-Journal of Applied Mathematics and Mechanics/Zeitschrift für Angewandte Mathematik und Mechanik: Applied Mathematics and Mechanics* 83 (2003), no. 11, pp. 731–754
- [Curie and Curie 1880] CURIE, J. ; CURIE, P.: Développement par compression de l'électricité polaire dans les cristaux hémihédres à faces inclinées. In: *Bulletin de minéralogie* 3 (1880), no. 4, pp. 90–93
- [Deniz et al. 2018] DENIZ, C. M. ; XIANG, S. ; HALLYBURTON, R. S. ; WELBECK, A. ; BABB, J. S. ; HONIG, S. ; CHO, K. ; CHANG, G.: Segmentation of the Proximal Femur from MR Images using Deep Convolutional Neural Networks. In: *Scientific Reports* 8 (2018), no. 1, pp. 16485
- [de Diego et al. 2022] DIEGO, A. de ; JUNGE, O. ; KARRASCH, D. ; SCHILLING, N.: *CoherentStructures.jl: Tools for computing Lagrangian Coherent Structures in Julia*. <https://coherentstructures.github.io/CoherentStructures.jl/stable/>. Version: 2022
- [Dorfmann and Ogden 2014] DORFMANN, A.L. ; OGDEN, R.W.: *Nonlinear Theory of Electroelastic and Magnetoelastic Interactions*. Springer US, 2014 <https://books.google.de/books?id=a90DswEACAAJ>. – ISBN 978–1–461–49597–0

- [Evans and Thomas 1973] EVANS, F. G. ; THOMAS, C. C.: Mechanical properties of bone. In: *Springfield, IL 1973* (1973), pp. 241–243
- [Fang et al. 2019] FANG, G. ; WANG, B. ; LIANG, J.: A coupled FE-FFT multiscale method for progressive damage analysis of 3D braided composite beam under bending load. In: *Composites Science and Technology* 181 (2019), pp. 107691
- [Fang et al. 2021] FANG, Y. ; LI, W. ; CHEN, X. ; CHEN, K. ; KANG, H. ; YU, P. ; ZHANG, R. ; LIAO, J. ; HONG, G. ; LI, S.: Opportunistic osteoporosis screening in multi-detector CT images using deep convolutional neural networks. In: *European Radiology* 31 (2021), no. 4, pp. 1831–1842
- [Feyel 1999] FEYEL, F.: Multiscale FE2 elastoviscoplastic analysis of composite structures. In: *Computational Materials Science* 16 (1999), no. 1-4, pp. 344–354
- [Feyel 2003] FEYEL, F.: A multilevel finite element method (FE2) to describe the response of highly non-linear structures using generalized continua. In: *Computer Methods in applied Mechanics and engineering* 192 (2003), no. 28-30, pp. 3233–3244
- [Frost 1990] FROST, H. M.: Skeletal structural adaptations to mechanical usage (SATMU): 1. Redefining Wolff’s law: the bone modeling problem. In: *The Anatomical Record* 226 (1990), no. 4, pp. 403–413
- [Frost and Straatsma 1964] FROST, H. M. ; STRAATSMA, C. R.: *Bone remodelling dynamics*. 1964
- [Fukada and Yasuda 1957] FUKADA, E. ; YASUDA, I.: On the Piezoelectric Effect of Bone. In: *Journal of the Physical Society of Japan* 12 (1957), no. 10, pp. 1158–1162
- [Garcia-Aznar et al. 2005] GARCIA-AZNAR, J. M. ; RÜBERG, T. ; DOBLARE, M.: A bone remodelling model coupling microdamage growth and repair by 3D BMU-activity. In: *Biomechanics and modeling in mechanobiology* 4 (2005), no. 2, pp. 147–167
- [Gardner et al. 2000] GARDNER, T. ; STOLL, T. ; MARKS, L. ; MISHRA, S.: The influence of mechanical stimulus on the pattern of tissue differentiation in a long bone fracture - An FEM study. In: *Journal of biomechanics* 33 (2000), 05, pp. 415–425
- [Geuzaine and Remacle 2022] GEUZAINÉ, C. ; REMACLE, J. F.: *Gmsh – A three-dimensional finite element mesh generator with built-in pre- and post-processing facilities*. <https://gmsh.info/>. Version: 2022
- [Ghaboussi et al. 2012] GHABOUSSI, J. ; WU, X. ; KAKLAUSKAS, G.: Neural network material modelling. In: *Statyba* 5 (2012), pp. 250–257
- [Gierden et al. 2022] GIERDEN, C. ; KOCHMANN, J. ; WAIMANN, J. ; SVENDSEN, B. ; REESE, S.: A review of FE-FFT-based two-scale methods for computational modeling of microstructure evolution and macroscopic material behavior. In: *Archives of Computational Methods in Engineering* 29 (2022), no. 6, pp. 4115–4135

- [Gilbert et al. 2021] GILBERT, R. P. ; VASILIC, A. ; KLINGE, S. ; PANCHENKO, A. ; HACKL, K.: *Applications of Homogenization Theory to the Study of Mineralized Tissue*. Boca Raton : CRC Press, Taylor Francis Group, 2021 <https://books.google.de/books?id=Wq0PEAAAQBAJ>. – ISBN 978-0-429-53324-2
- [Giorgio et al. 2019] GIORGIO, I. ; DELL'ISOLA, F. ; ANDREAUS, U. ; ALZHRANI, F. ; HAYAT, T. ; LEKSZYCKI, T.: On mechanically driven biological stimulus for bone remodeling as a diffusive phenomenon. In: *Biomechanics and modeling in mechanobiology* 18 (2019), pp. 1639–1663
- [Goodfellow et al. 2016] GOODFELLOW, I. ; BENGIO, Y. ; COURVILLE, A.: *Deep learning*. MIT press, 2016
- [Grampp et al. 1997] GRAMPP, S. ; STEINER, E. ; IMHOF, H.: Radiological diagnosis of osteoporosis. In: *European radiology* 7 (1997), pp. S11
- [Graps 1995] GRAPS, A.: "An Introduction to Wavelets". In: *IEEE Comp. Sci. Engi.* 2 (1995), pp. 50–61
- [Güzelsu and Demiray 1979] GÜZELSU, N. ; DEMIRAY, H.: Electromechanical properties and related models of bone tissues: A review. In: *International Journal of Engineering Science* 17 (1979), no. 7, pp. 813–851
- [Güzelsu and Saha 1981] GÜZELSU, N. ; SAHA, S.: Electro-mechanical wave propagation in long bones. In: *Journal of Biomechanics* 14 (1981), no. 1, pp. 19 – 33
- [Hambli et al. 2016] HAMBALI, R. ; BOUGHATTAS, M. H. ; DANIEL, J.-L. ; KOURTA, A.: Prediction of denosumab effects on bone remodeling: a combined pharmacokinetics and finite element modeling. In: *Journal of the mechanical behavior of biomedical materials* 60 (2016), pp. 492–504
- [Hamed et al. 2010] HAMED, E. ; LEE, Y. ; JASIUK, I.: Multiscale modeling of elastic properties of cortical bone. In: *Acta Mechanica* 213 (2010), no. 1, pp. 131–154
- [Han et al. 2003] HAN, X. ; XU, D. ; LIU, G.R.: A computational inverse technique for material characterization of a functionally graded cylinder using a progressive neural network. In: *Neurocomputing* 51 (2003), pp. 341–360
- [Hannot 2010] HANNOT, S. D. A.: *Modeling strategies for electro-mechanical microsystems with uncertainty quantification*, TU Delft, Diss., 2010
- [Hashin and Shtrikman 1963] HASHIN, Z. ; SHTRIKMAN, S.: A variational approach to the theory of the elastic behaviour of multiphase materials. In: *Journal of the Mechanics and Physics of Solids* 11 (1963), no. 2, pp. 127–140
- [Hill 1963] HILL, R.: Elastic properties of reinforced solids: Some theoretical principles. In: *Journal of the Mechanics and Physics of Solids* 11 (1963), no. 5, pp. 357 – 372

- [Hill 1972] HILL, R.: On Constitutive Macro-Variables for Heterogeneous Solids at Finite Strain. In: *Proceedings of the Royal Society of London. Series A, Mathematical and Physical Sciences* 326 (1972), no. 1565, pp. 131–147
- [Hosokawa and Otani 1997] HOSOKAWA, A. ; OTANI, T.: Ultrasonic wave propagation in bovine cancellous bone. In: *J. Acoust. Soc. Am.* 101 (1997), no. 1, pp. 558–562
- [Iliou et al. 2017] ILIOU, T. ; ANAGNOSTOPOULOS, C.N. ; STEPHANAKIS, I. M. ; ANASTASOPOULOS, G.: A novel data preprocessing method for boosting neural network performance: A case study in osteoporosis prediction. In: *Information Sciences* 380 (2017), pp. 92–100
- [Ilić and Hackl 2004] ILIĆ, S. ; HACKL, K.: Homogenisation of random composites via the multiscale finite-element method. In: *PAMM* 4 (2004), no. 1, pp. 326–327
- [Ilić et al. 2010] ILIĆ, S. ; HACKL, K. ; GILBERT, R. P.: Application of the multiscale FEM to the modeling of cancellous bone. In: *Biomechanics and Modeling in Mechanobiology* 9 (2010), no. 1, pp. 87–102
- [Innes 2018] INNES, M.: Flux: Elegant machine learning with Julia. In: *Journal of Open Source Software* 3 (2018), no. 25, pp. 602
- [Innes et al. 2018] INNES, M. ; SABA, E. ; FISCHER, K. ; GANDHI, D. ; RUDILOSSO, M. ; MARIYA JOY, N. ; KARMALI, T. ; PAL, A. ; SHAH, V.: Fashionable Modelling with Flux. In: *CoRR* abs/1811.01457 (2018)
- [Ivakhnenko and Lapa 1965] IVAKHNENKO, A.I. G. ; LAPA, V. G.: *Cybernetic predicting devices*. CCM Information Corporation, 1965
- [Jin 2015] JIN, J.-M.: *The finite element method in electromagnetics*. John Wiley & Sons, 2015
- [Jumper et al. 2021] JUMPER, J. ; EVANS, R. ; PRITZEL, A. ; GREEN, T. ; FIGURNOV, M. ; RONNEBERGER, O. ; TUNYASUVUNAKOOL, K. ; BATES, R. ; ŽÍDEK, A. ; POTAPENKO, A. et al.: Highly accurate protein structure prediction with AlphaFold. In: *Nature* 596 (2021), no. 7873, pp. 583–589
- [Kadapa et al. 2017] KADAPA, C. ; DETTMER, W. ; PERIĆ, D.: On the advantages of using the first-order generalised-alpha scheme for structural dynamic problems. In: *Computers & Structures* 193 (2017), 12, pp. 226–238
- [Karimi et al. 2019] KARIMI, P. ; ZHANG, X. ; YAN, S. ; OSTOJA-STARZEWSKI, M. ; JIN, J. M.: Electrostatic and magnetostatic properties of random materials. In: *Phys. Rev. E* 99 (2019), pp. 022120
- [Kaufman et al. 2008] KAUFMAN, J. J. ; LUO, G. ; SIFFERT, R. S.: Ultrasound simulation in bone. In: *IEEE transactions on ultrasonics, ferroelectrics, and frequency control* 55 (2008), no. 6, pp. 1205–1218

- [Keaveny 2010] KEAVENY, T. M.: Biomechanical computed tomography—noninvasive bone strength analysis using clinical computed tomography scans. In: *Annals of the New York Academy of Sciences* 1192 (2010), no. 1, pp. 57–65
- [Kitware Inc. 2022] KITWARE INC.: *ParaView*. <https://www.paraview.org/>. Version: 2022
- [Klimešová 2019] KLIMEŠOVÁ, Markéta: *Femur (caput femoris)*. *Anthropological collections, Department of Biology and Environmental Studies, Faculty of Education, Charles University (Czech Republic)*. [https://commons.wikimedia.org/wiki/File:Femur_\(caput_femoris\)_-_bone_structure_detail_\(vertical_cut\)_2.jpg](https://commons.wikimedia.org/wiki/File:Femur_(caput_femoris)_-_bone_structure_detail_(vertical_cut)_2.jpg). Version: 2019
- [Klimešová 2022a] KLIMEŠOVÁ, Markéta: *Femur - detail of diaphysis cross section*. *Anthropological collections, Department of Biology and Environmental Studies, Faculty of Education, Charles University (Czech Republic)*. https://commons.wikimedia.org/wiki/File:Femur_-_detail_of_diaphysis_cross_section.jpg. Version: 2022
- [Klimešová 2022b] KLIMEŠOVÁ, Markéta: *Femur (caput femoris) - bone structure detail (vertical cut)*. *Anthropological collections, Department of Biology and Environmental Studies, Faculty of Education, Charles University (Czech Republic)*. [https://commons.wikimedia.org/wiki/File:Femur_\(caput_femoris\)_-_bone_structure_detail_\(vertical_cut\).jpg](https://commons.wikimedia.org/wiki/File:Femur_(caput_femoris)_-_bone_structure_detail_(vertical_cut).jpg). Version: 2022
- [Klinge et al. 2013] KLINGE, S. ; HACKL, K. ; GILBERT, R. P.: Investigation of the influence of reflection on the attenuation of cancellous bone. In: *Biomechanics and modeling in mechanobiology* 12 (2013), no. 1, pp. 185–199
- [Kochmann et al. 2016] KOCHMANN, J. ; WULFINGHOFF, S. ; REESE, S. ; MIANROODI, J. R. ; SVENDSEN, B.: Two-scale FE–FFT-and phase-field-based computational modeling of bulk microstructural evolution and macroscopic material behavior. In: *Computer Methods in Applied Mechanics and Engineering* 305 (2016), pp. 89–110
- [Kristensen et al. 2020] KRISTENSEN, P. K. ; NIORDSON, C. F. ; MARTÍNEZ-PAÑEDA, E.: A phase field model for elastic-gradient-plastic solids undergoing hydrogen embrittlement. In: *Journal of the Mechanics and Physics of Solids* 143 (2020), pp. 104093
- [Kuhn and Müller 2010] KUHN, C. ; MÜLLER, R.: A continuum phase field model for fracture. In: *Engineering Fracture Mechanics* 77 (2010), no. 18, pp. 3625–3634
- [Kumar et al. 2020] KUMAR, S. ; TAN, S. ; ZHENG, L. ; KOCHMANN, D. M.: Inverse-designed spinodoid metamaterials. In: *npj Computational Materials* 6 (2020), no. 1, pp. 73

- [Laboratoires Servier 2019] LABORATOIRES SERVIER: *Osteoporosis - Smart Servier - image composed from SMART - Servier Medical ART* (<https://smart.servier.com/category/anatomy-and-the-human-body/locomotor-system/bones/>) and Flickr: *Images related to Osteoporosis, Bone structure and Bone* (<https://www.flickr.com/photos/serviermedicalart/sets/72157635892724256>). https://commons.wikimedia.org/wiki/File:Osteoporosis_-_Smart-Servier.jpg. Version: 2019
- [Laboratoires Servier 2022] LABORATOIRES SERVIER: *Thigh bone - Femur – Smart-Servier. SMART - Servier Medical ART* (<https://smart.servier.com/category/anatomy-and-the-human-body/locomotor-system/bones/>). https://commons.wikimedia.org/wiki/File:Thigh_bone_-_Femur_-_Smart-Servier.jpg. Version: 2022
- [Labusch et al. 2019] LABUSCH, M. ; SCHRÖDER, J. ; LUPASCU, D. C.: A two-scale homogenization analysis of porous magneto-electric two-phase composites. In: *Archive of Applied Mechanics* 89 (2019), no. 6, pp. 1123–1140
- [Langer 1986] LANGER, J. S.: Models of pattern formation in first-order phase transitions. In: *Directions in condensed matter physics: Memorial volume in honor of shang-keng ma*. World Scientific, 1986, pp. 165–186
- [Lifescience Database 2022] LIFESCIENCE DATABASE: *Lifescience Database*. <https://lifesciencedb.jp/bp3d/>. Version: 2022
- [Locke 2004] LOCKE, M.: Structure of long bones in mammals. In: *Journal of Morphology* 262 (2004), no. 2, pp. 546–565
- [Lucarini and Segurado 2019] LUCARINI, S. ; SEGURADO, J.: On the accuracy of spectral solvers for micromechanics based fatigue modeling. In: *Computational Mechanics* 63 (2019), pp. 365–382
- [Lupascu et al. 2017] LUPASCU, D. C. ; ANUSCA, I. ; ETIER, M. ; GAO, Y. ; LACKNER, G. ; NAZRABI, A. ; SANLIALP, M. ; TRIVEDI, H. ; UL-HAQ, N. ; SCHRÖDER, J.: Semiconductor Effects in Ferroelectrics. In: *Ferroic Functional Materials: Experiment, Modeling and Simulation*. Cham : Springer, 2017, pp. 97–178
- [Mano et al. 2007] MANO, I. ; YAMAMOTO, T. ; HAGINO, H. ; TESHIMA, R. ; TAKADA, M. ; TSUJIMOTO, T. ; OTANI, T.: Ultrasonic transmission characteristics of in vitro human cancellous bone. In: *Japanese Journal of Applied Physics* 46 (2007), no. 7S, pp. 4858
- [Martínez-Cisneros et al. 2020] MARTÍNEZ-CISNEROS, E. ; VELOSA-MONCADA, L. A. ; DEL ANGEL-ARROYO, J. A. ; AGUILERA-CORTÉS, L. A. ; CERÓN-ÁLVAREZ, C. A. ; HERRERA-MAY, A. L.: Electromechanical modeling of MEMS-based piezoelectric energy harvesting devices for applications in domestic washing machines. In: *Energies* 13 (2020), no. 3, pp. 617

- [McCulloch and Pitts 1943] MCCULLOCH, W. S. ; PITTS, W.: A logical calculus of the ideas immanent in nervous activity. In: *The bulletin of mathematical biophysics* 5 (1943), no. 4, pp. 115–133
- [McKelvie and Palmer 1991] MCKELVIE, M. L. ; PALMER, S. B.: The interaction of ultrasound with cancellous bone. In: *Physics in Medicine & Biology* 36 (1991), no. 10, pp. 1331
- [Mehrabadi and Cowin 1990] MEHRABADI, M. M. ; COWIN, S. C.: Eigentensors of linear anisotropic elastic materials. In: *The Quarterly Journal of Mechanics and Applied Mathematics* 43 (1990), no. 1, pp. 15–41
- [Mehta and Rajani 1970] MEHTA, B. V. ; RAJANI, S.: Finite element analysis of the human tibia. In: *WIT Transactions on Biomedicine and Health* 2 (1970)
- [Meng et al. 2013] MENG, L. ; ZHANG, Y. ; LU, Y.: Three-dimensional finite element analysis of mini-external fixation and Kirschner wire internal fixation in Bennett fracture treatment. In: *Orthopaedics & Traumatology: Surgery & Research* 99 (2013), no. 1, pp. 21–29
- [Mi et al. 2007] MI, Z. R. ; SHUIB, S. ; HASSAN, A. Y. ; SHORKI, A. A. ; IBRAHIM, M. M.: Problem of stress shielding and improvement to the hip Implat designs: a review. In: *J. Med. Sci* 7 (2007), no. 3, pp. 460–467
- [Miehe et al. 2002] MIEHE, C. ; SCHOTTE, J. ; LAMBRECHT, M.: Homogenization of inelastic solid materials at finite strains based on incremental minimization principles. Application to the texture analysis of polycrystals. In: *Journal of the Mechanics and Physics of Solids* 50 (2002), no. 10, pp. 2123 – 2167
- [Miehe et al. 1999] MIEHE, C. ; SCHRÖDER, J. ; SCHOTTE, J.: Computational homogenization analysis in finite plasticity simulation of texture development in polycrystalline materials. In: *Computer methods in applied mechanics and engineering* 171 (1999), no. 3-4, pp. 387–418
- [Miehe et al. 2010] MIEHE, C. ; WELSCHINGER, F. ; HOFACKER, M.: Thermodynamically consistent phase-field models of fracture: Variational principles and multi-field FE implementations. In: *International journal for numerical methods in engineering* 83 (2010), no. 10, pp. 1273–1311
- [Miller et al. 2002] MILLER, Z. ; FUCHS, M. ; ARCAN, M.: Trabecular bone adaptation with an orthotropic material model. In: *Journal of biomechanics* 35 (2002), pp. 247–56
- [Mohamed et al. 2003] MOHAMED, E. ; MAIOLO, C. ; LINDER, R. ; PÖPPL, S. ; DE LORENZO, A.: Artificial neural network analysis: A novel application for predicting site-specific bone mineral density. In: *Acta diabetologica* 40 Suppl 1 (2003), pp. S19–22
- [Mohammadkhah et al. 2019] MOHAMMADKHAH, M. ; MARINKOVIC, D. ; ZEHN, M. ; CHECA, S.: A review on computer modeling of bone piezoelectricity and its application to bone adaptation and regeneration. In: *Bone* 127 (2019), pp. 544 – 555

- [Moulinec and Suquet 1995] MOULINEC, H. ; SUQUET, P.: A FFT-based numerical method for computing the mechanical properties of composites from images of their microstructures. In: *IUTAM Symposium on Microstructure-Property Interactions in Composite Materials: Proceedings of the IUTAM Symposium held in Aalborg, Denmark, 22–25 August 1994* Springer Netherlands, 1995, pp. 235–246
- [Mur 1998] MUR, G.: The fallacy of edge elements. In: *IEEE Transactions on Magnetics* 34 (1998), no. 5, pp. 3244–3247
- [Nardinocchi and Teresi 2013] NARDINOCCHI, P. ; TERESI, L.: Electromechanical modeling of anisotropic cardiac tissues. In: *Mathematics and Mechanics of Solids* 18 (2013), no. 6, pp. 576–591
- [Nédélec 1980] NÉDÉLEC, J.-C.: Mixed finite elements in R3. In: *Numerische Mathematik* 35 (1980), no. 3, pp. 315–341
- [Pahr and Zysset 2008] PAHR, D. H. ; ZYSSET, P. K.: Influence of boundary conditions on computed apparent elastic properties of cancellous bone. In: *Biomechanics and Modeling in Mechanobiology* 7 (2008), no. 6, pp. 463–476
- [Pandolfi et al. 2016] PANDOLFI, A. ; GIZZI, A. ; VASTA, M.: Coupled electro-mechanical models of fiber-distributed active tissues. In: *Journal of Biomechanics* 49 (2016), no. 12, pp. 2436–2444
- [Paranjape et al. 2016] PARANJAPE, H. M. ; MANCHIRAJU, S. ; ANDERSON, P. M.: A phase field–Finite element approach to model the interaction between phase transformations and plasticity in shape memory alloys. In: *International Journal of Plasticity* 80 (2016), pp. 1–18
- [Parashar and Sharma 2016] PARASHAR, S. K. ; SHARMA, J. K.: A review on application of finite element modelling in bone biomechanics. In: *Perspectives in Science* 8 (2016), pp. 696–698
- [Pbrks/Wikimedia 2022] PBRKS/WIKIMEDIA: *Bone cross-section*. https://commons.wikimedia.org/wiki/File:Bone_cross-section.svg. Version: 2022
- [Peck 1993] PECK, W.A.: Consensus development conference: diagnosis, prophylaxis, and treatment of osteoporosis. In: *Am J Med* 94 (1993), no. 6, pp. 646–650
- [Podshivalov et al. 2011] PODSHIVALOV, L. ; FISCHER, A. ; BAR-YOSEPH, P.Z.: Multiscale FE method for analysis of bone micro-structures. In: *Journal of the Mechanical Behavior of Biomedical Materials* 4 (2011), no. 6, pp. 888 – 899. – Bone Remodeling
- [Prakash and Lebensohn 2009] PRAKASH, A. ; LEBENSOHN, R. A.: Simulation of micromechanical behavior of polycrystals: finite elements versus fast Fourier transforms. In: *Modelling and Simulation in Materials Science and Engineering* 17 (2009), no. 6, pp. 064010

- [Pugh et al. 1973] PUGH, J. W. ; ROSE, R. M. ; RADIN, E. L.: A structural model for the mechanical behavior of trabecular bone. In: *Journal of Biomechanics* 6 (1973), no. 6, pp. 657–670
- [Pustan et al. 2014] PUSTAN, M. ; BIRLEANU, C. ; DUDESCU, C. ; GOLINVAL, J.-C.: Dynamic behavior of smart MEMS in industrial applications. In: *Smart Sensors and Mems*. Cambridge : Elsevier, 2014, pp. 349–365
- [Reginster and Burlet 2006] REGINSTER, J.-Y. ; BURLET, N.: Osteoporosis: a still increasing prevalence. In: *Bone* 38 (2006), no. 2, pp. 4–9
- [Reuß 1929] REUSS, A.: Berechnung der Fließgrenze von Mischkristallen auf Grund der Plastizitätsbedingung für Einkristalle. In: *ZAMM-Journal of Applied Mathematics and Mechanics/Zeitschrift für Angewandte Mathematik und Mechanik* 9 (1929), no. 1, pp. 49–58
- [Ringe et al. 2019] RINGE, J.D. ; BÜHRING, M. ; DÖREN, M. ; MÜNZENBERG, K.J. ; REINERS, C. ; SCHNEIDER, H.P.G. ; SCHULZ, A.: *Osteoporose: Pathogenese, Diagnostik und Therapiemöglichkeiten*. De Gruyter, 2019. – ISBN 9783110879513
- [Robson Brown et al. 2014] ROBSON BROWN, K. ; TARSUSLUGIL, S. ; WIJAYATHUNGA, V. N. ; WILCOX, R. K.: Comparative finite-element analysis: a single computational modelling method can estimate the mechanical properties of porcine and human vertebrae. In: *Journal of The Royal Society Interface* 11 (2014), no. 95, pp. 20140186
- [Röhrle et al. 2008] RÖHRLE, O. ; DAVIDSON, J. B. ; PULLAN, A. J.: Bridging scales: a three-dimensional electromechanical finite element model of skeletal muscle. In: *SIAM Journal on Scientific Computing* 30 (2008), no. 6, pp. 2882–2904
- [Rosenblatt 1957] ROSENBLATT, F.: *The perceptron, a perceiving and recognizing automaton Project Para*. Cornell Aeronautical Laboratory, 1957
- [Ruthotto and Treister 2022] RUTHOTTO, L. ; TREISTER, E.: *KrylovMethods.jl: Simple and fast Julia implementation of Krylov subspace methods for linear systems*. <https://github.com/JuliaInv/KrylovMethods.jl>. Version: 2022
- [Samarasinghe 2016] SAMARASINGHE, S.: *Neural networks for applied sciences and engineering: from fundamentals to complex pattern recognition*. Auerbach publications, 2016
- [Scheiner et al. 2013] SCHEINER, S. ; PIVONKA, P. ; HELLMICH, C.: Coupling systems biology with multiscale mechanics, for computer simulations of bone remodeling. In: *Computer Methods in Applied Mechanics and Engineering* 254 (2013), pp. 181–196
- [Schlick et al. 2021] SCHLICK, T. ; PORTILLO-LEDESMA, S. ; BLASZCZYK, M. ; DALESSANDRO, L. ; GHOSH, S. ; HACKL, K. ; HARNISH, C. ; KOTHA, S. ; LIVESCU, D. ; MASUD, A. ; MATOUS, K. ; MOYEDA, A. ; OSKAY, C. ; FISH, J.: A multiscale vision - Illustrative applications from biology to engineering. In: *International Journal for Multiscale Computational Engineering* 19 (2021), no. 2, pp. 39–73. – ISSN 1543–1649

- [Schneider 2021] SCHNEIDER, M.: A review of nonlinear FFT-based computational homogenization methods. In: *Acta Mechanica* 232 (2021), Jun, no. 6, pp. 2051–2100
- [Schrade et al. 2007] SCHRADER, D. ; MÜLLER, R. ; XU, B.-X. ; GROSS, D.: Domain evolution in ferroelectric materials: A continuum phase field model and finite element implementation. In: *Computer methods in applied mechanics and engineering* 196 (2007), no. 41-44, pp. 4365–4374
- [Schröder 2000] SCHRÖDER, J.: *Homogenisierungsmethoden der nichtlinearen Kontinuumsmechanik unter Beachtung von Instabilitäten*. Stuttgart : Institut für Mechanik (Bauwesen), Lehrstuhl I, Universität Stuttgart, 2000. – Habilitationsschrift
- [Schröder and Hackl 2013] SCHRÖDER, J. ; HACKL, K.: *Plasticity and Beyond: Microstructures, Crystal-Plasticity and Phase Transitions*. Springer Vienna, 2013 (CISM International Centre for Mechanical Sciences). <https://books.google.de/books?id=hg3HBAAAQBAJ>. – ISBN 978–3–709–11625–8
- [Schröder and Keip 2012] SCHRÖDER, J. ; KEIP, M.-A.: Two-scale homogenization of electromechanically coupled boundary value problems: Consistent linearization and applications. In: *Computational mechanics* 50 (2012), no. 2, pp. 229–244
- [Schröder 2009] SCHRÖDER, J.: Derivation of the localization and homogenization conditions for electro-mechanically coupled problems. In: *Computational Materials Science* 46 (2009), pp. 595–599
- [Schröder et al. 2016] SCHRÖDER, J. ; LABUSCH, M. ; KEIP, M. A.: Algorithmic two-scale transition for magneto-electro-mechanically coupled problems: FE2-scheme: Localization and homogenization. In: *Computer Methods in Applied Mechanics and Engineering* 302 (2016), pp. 253 – 280
- [Semenov et al. 2006] SEMENOV, A. S. ; KESSLER, H. ; LISKOWSKY, A. ; BALKE, H.: On a vector potential formulation for 3D electromechanical finite element analysis. In: *Communications in Numerical Methods in Engineering* 22 (2006), no. 5, pp. 357–375
- [Sengupta et al. 2012] SENGUPTA, A. ; PAPADOPOULOS, P. ; TAYLOR, R. L.: A multiscale finite element method for modeling fully coupled thermomechanical problems in solids. In: *International Journal for Numerical Methods in Engineering* 91 (2012), no. 13, pp. 1386–1405
- [Shahid et al. 2019] SHAHID, N. ; RAPPON, T. ; BERTA, W.: Applications of artificial neural networks in health care organizational decision-making: A scoping review. In: *PloS one* 14 (2019), no. 2, pp. e0212356
- [Shamos et al. 1963] SHAMOS, M. H. ; LAVINE, L. S. ; SHAMOS, M. I.: Piezoelectric Effect in Bone. In: *Nature* 197 (1963), no. 4862, pp. 81–81
- [Silver et al. 2016] SILVER, D. ; HUANG, A. ; MADDISON, C. J. ; GUEZ, A. ; SIFRE, L. ; VAN DEN DRIESSCHE, G. ; SCHRITTWIESER, J. ; ANTONOGLU, I. ; PANNEERSHELVAM, V. ; LANCTOT, M. et al.: Mastering the game of Go with deep neural networks and tree search. In: *nature* 529 (2016), no. 7587, pp. 484–489

- [Silver et al. 2018] SILVER, D. ; HUBERT, T. ; SCHRITTWIESER, J. ; ANTONOGLIOU, I. ; LAI, M. ; GUEZ, A. ; LANCTOT, M. ; SIFRE, L. ; KUMARAN, D. ; GRAEPEL, T. et al.: A general reinforcement learning algorithm that masters chess, shogi, and Go through self-play. In: *Science* 362 (2018), no. 6419, pp. 1140–1144
- [Singh et al. 2017] SINGH, A. ; DUTTA, M. ; JENNANE, R. ; LESPESSAILLES, E.: Classification of the trabecular bone structure of osteoporotic patients using machine vision. In: *Computers in Biology and Medicine* 91 (2017), pp. 148–158
- [Sivapuram et al. 2016] SIVAPURAM, R. ; DUNNING, P. D. ; KIM, H. A.: Simultaneous material and structural optimization by multiscale topology optimization. In: *Structural and multidisciplinary optimization* 54 (2016), pp. 1267–1281
- [Smajic et al. 2015] SMAJIC, J. ; HAFNER, C. ; LEUTHOLD, J.: Coupled FEM-MMP for computational electromagnetics. In: *IEEE Transactions on Magnetics* 52 (2015), no. 3, pp. 1–4
- [Sobotková et al. 1988] SOBOTKOVÁ, E. ; HRUBÁ, A. ; KIEFMAN, J. ; SOBOTKA, Z.: Rheological behaviour of bone marrow. In: *Progress and trends in rheology II*. Springer, 1988, pp. 467–469
- [Spadaro 1997] SPADARO, J. A.: Mechanical and electrical interactions in bone remodeling. In: *Bioelectromagnetics: Journal of the Bioelectromagnetics Society* 18 (1997), no. 3, pp. 193–202
- [Spahn et al. 2014] SPAHN, J. ; ANDRÄ, H. ; KABEL, M. ; MÜLLER, R.: A multiscale approach for modeling progressive damage of composite materials using fast Fourier transforms. In: *Computer Methods in Applied Mechanics and Engineering* 268 (2014), pp. 871–883
- [Steeb 2010] STEEB, H.: Ultrasound propagation in cancellous bone. In: *Archive of Applied Mechanics* 80 (2010), no. 5, pp. 489–502
- [Stieve et al. 2022] STIEVE, V. ; BLASZCZYK, M. ; HACKL, K.: Inverse modeling of cancellous bone using artificial neural networks. In: *ZAMM-Journal of Applied Mathematics and Mechanics/Zeitschrift für Angewandte Mathematik und Mechanik* 102 (2022), no. 6, pp. e202100541
- [Struzik and Siebes 1999] STRUZIĆ, Z. R. ; SIEBES, A.: The Haar Wavelet Transform in the Time Series Similarity Paradigm. In: ŻYTKOW, J. M. (Hrsg.) ; RAUCH, J. (Hrsg.): *Principles of Data Mining and Knowledge Discovery*. Berlin, Heidelberg : Springer Berlin Heidelberg, 1999. – ISBN 978-3-540-48247-5, pp. 12–22
- [Suquet 1987] SUQUET, P. M.: Elements of homogenization for inelastic solid mechanics, homogenization techniques for composite media. In: *Lecture notes in physics* 272 (1987), pp. 193
- [Svendsen et al. 2018] SVENDSEN, B. ; SHANTHRAJ, P. ; RAABE, D.: Finite-deformation phase-field chemomechanics for multiphase, multicomponent solids. In: *Journal of the Mechanics and Physics of Solids* 112 (2018), pp. 619–636

- [Szolc et al. 2014] SZOLC, T. ; KONOWROCKI, R. ; MICHAJŁOW, M. ; PRĘGOWSKA, A.: An investigation of the dynamic electromechanical coupling effects in machine drive systems driven by asynchronous motors. In: *Mechanical Systems and Signal Processing* 49 (2014), no. 1-2, pp. 118–134
- [Talukder and Harada 2010] TALUKDER, K. ; HARADA, K.: Haar Wavelet Based Approach for Image Compression and Quality Assessment of Compressed Image. In: *IAENG Int J Appl Math* 36 (2010)
- [Tamsen and Balzani 2021] TAMSEN, E. ; BALZANI, D.: A general, implicit, finite-strain FE 2 framework for the simulation of dynamic problems on two scales. In: *Computational Mechanics* 67 (2021), no. 5, pp. 1375–1394
- [Tandler 1919] TANDLER, J.: *Lehrbuch der systematischen Anatomie: Knochen-, Gelenk- und Muskellehre*. Verlag von F. C. W. Vogel, 1919 (Bd. 1)
- [Tsukutani et al. 2015] TSUKUTANI, Y. ; HAGINO, H. ; ITO, Y. ; NAGASHIMA, H.: Epidemiology of fragility fractures in Sakaiminato, Japan: Incidence, secular trends, and prognosis. In: *Osteoporosis international* 26 (2015), no. 9, pp. 2249–2255
- [Turner Biomechanics Laboratory 2011] TURNER BIOMECHANICS LABORATORY: *File:Bone Comparison of Healthy and Osteoporotic Vertebrae.png*. Osseon (<http://www.osseon.com/osteoporosis-overview/>). https://commons.wikimedia.org/wiki/File:Bone_Comparison_of_Healthy_and_Osteoporotic_Vertebrae.png. Version: 2011
- [Ural and Mischinski 2013] URAL, A. ; MISCHINSKI, S.: Multiscale modeling of bone fracture using cohesive finite elements. In: *Engineering Fracture Mechanics* 103 (2013), pp. 141 – 152
- [Ural et al. 2011] URAL, A. ; ZIOUPOS, P. ; BUCHANAN, D. ; VASHISHTH, D.: The effect of strain rate on fracture toughness of human cortical bone: a finite element study. In: *Journal of the mechanical behavior of biomedical materials* 4 (2011), no. 7, pp. 1021–1032
- [Uth et al. 2017] UTH, N. ; MUELLER, J. ; SMUCKER, B. ; YOUSEFI, A.-M.: Validation of scaffold design optimization in bone tissue engineering: finite element modeling versus designed experiments. In: *Biofabrication* 9 (2017), no. 1, pp. 015023
- [Vasquez-Sancho et al. 2018] VASQUEZ-SANCHO, F. ; ABDOLLAHI, A. ; DAMJANOVIC, D. ; CATALAN, G.: Flexoelectricity in bones. In: *Advanced materials* 30 (2018), no. 9, pp. 1705316
- [Vishnu et al. 2015] VISHNU, T. ; SARANYA, K. ; ARUNKUMAR, R. ; DEVI, M. G.: Efficient and early detection of osteoporosis using trabecular region. In: *2015 Online International Conference on Green Engineering and Technologies (IC-GET)*, 2015, pp. 1–5
- [Voigt 1889] VOIGT, W.: Ueber die Beziehung zwischen den beiden Elasticitätsconstanten isotroper Körper. In: *Annalen der Physik* 274 (1889), no. 12, pp. 573–587

- [Wade et al. 2014] WADE, S. W. ; STRADER, C. ; FITZPATRICK, L. A. ; ANTHONY, M. S. ; O'MALLEY, C. D.: Estimating prevalence of osteoporosis: Examples from industrialized countries. In: *Archives of osteoporosis* 9 (2014), no. 1, pp. 1–10
- [Wang et al. 2017] WANG, L. ; ZHANG, J. ; ZHANG, W. ; YANG, H.-L. ; LUO, Z.-P.: Analysis of the Osteogenic Effects of Biomaterials Using Numerical Simulation. In: *BioMed research international* 2017 (2017), pp. 6981586–6981586. – 28116309[pmid]
- [Wani and Arora 2020] WANI, I. ; ARORA, S.: Deep Neural Networks for Diagnosis of Osteoporosis: A Review. In: *Proceedings of ICRIC 2019*, Springer, 2020. – ISBN 978–3–030–29406–9, pp. 65–78
- [Willis 1981] WILLIS, J. R.: Variational and related methods for the overall properties of composites. In: *Advances in applied mechanics* 21 (1981), pp. 1–78
- [Witt et al. 2022] WITT, C. ; KAISER, T. ; MENZEL, A.: Modelling and numerical simulation of remodelling processes in cortical bone: An IGA approach to flexoelectricity-induced osteocyte apoptosis and subsequent bone cell diffusion. In: *Journal of the Mechanics and Physics of Solids* 173 (2022), pp. 105194
- [Wojcik et al. 1993] WOJCIK, G. L. ; VAUGHAN, D. K. ; ABBOUD, N. ; MOULD, J. J.: Electromechanical modeling using explicit time-domain finite elements. In: *1993 Proceedings IEEE Ultrasonics Symposium IEEE*, 1993, pp. 1107–1112
- [Wolff 1892] WOLFF, J.: Das Gesetz der Transformation der Knochen. In: *Verlag von August Hirschwald* (1892)
- [Wu et al. 2020] WU, J.-Y. ; NGUYEN, V. P. ; NGUYEN, C. T. ; SUTULA, D. ; SINAIE, S. ; BORDAS, S. P. A.: Phase-field modeling of fracture. In: *Advances in applied mechanics* 53 (2020), pp. 1–183
- [Yamamoto et al. 2020] YAMAMOTO, N. ; SHINTARO, S. ; KITAMURA, A. ; GOTO, R. ; NODA, T. ; NAKANO, K. ; TAKABATAKE, K. ; KAWAI, H. ; NAGATSUKA, H. ; KAWASAKI, K. ; FURUKI, Y. ; OZAKI, T.: Deep Learning for Osteoporosis Classification Using Hip Radiographs and Patient Clinical Covariates. In: *Biomolecules* 10 (2020), pp. 1534
- [Yang and Dayal 2011] YANG, L. ; DAYAL, K.: A completely iterative method for the infinite domain electrostatic problem with nonlinear dielectric media. In: *Journal of Computational Physics* 230 (2011), no. 21, pp. 7821–7829
- [Yu et al. 2016] YU, X. ; YE, C. ; XIANG, L.: Application of artificial neural network in the diagnostic system of osteoporosis. In: *Neurocomputing* 214 (2016), pp. 376–381
- [Yvonnet and Liu 2017] YVONNET, J. ; LIU, L. P.: A numerical framework for modeling flexoelectricity and Maxwell stress in soft dielectrics at finite strains. In: *Computer Methods in Applied Mechanics and Engineering* 313 (2017), pp. 450–482

- [Zheng et al. 2021] ZHENG, L. ; KUMAR, S. ; KOCHMANN, D. M.: Data-driven topology optimization of spinodoid metamaterials with seamlessly tunable anisotropy. In: *Computer Methods in Applied Mechanics and Engineering* 383 (2021), pp. 113894
- [Zhou et al. 2021] ZHOU, W. ; WANG, B. ; LIM, C. W. ; YANG, Z.: A distributed-parameter electromechanical coupling model for a segmented arc-shaped piezoelectric energy harvester. In: *Mechanical Systems and Signal Processing* 146 (2021), pp. 107005
- [Zhuang et al. 2020] ZHUANG, X. ; NGUYEN, B. H. ; NANTHAKUMAR, S. S. ; TRAN, T. Q. ; ALAJLAN, N. ; RABCZUK, T.: Computational modeling of flexoelectricity—a review. In: *Energies* 13 (2020), no. 6, pp. 1326
- [Zhuang et al. 2023] ZHUANG, X. ; THAI, T. Q. ; RABCZUK, T.: Topology optimization of nonlinear flexoelectric structures. In: *Journal of the Mechanics and Physics of Solids* 171 (2023), pp. 105117
- [Zienkiewicz et al. 2005] ZIENKIEWICZ, O. C. ; TAYLOR, R. L. ; ZHU, J. Z.: *The Finite Element Method: Its Basis and Fundamentals, Sixth Edition*. 6. Butterworth-Heinemann, 2005
- [Zysset et al. 2013] ZYSSET, P. K. ; DALL'ARA, E. ; VARGA, P. ; PAHR, D. H.: Finite element analysis for prediction of bone strength. In: *BoneKEy reports* 2 (2013)

Lebenslauf (CV)

Persönliche Daten

Name: Mischa Blaszczyk
Wohnort: Bochum, Deutschland
Geburtsdatum: 09. März 1994
Geburtsort: Recklinghausen, Deutschland
Staatsangehörigkeit: Deutsch

Beruflicher Werdegang

seit 06/2019 Wissenschaftlicher Mitarbeiter
am Lehrstuhl für Mechanik – Materialtheorie,
Ruhr-Universität Bochum

03/2015 – 05/2019 Studentische Hilfskraft
am Lehrstuhl für Mechanik – Kontinuumsmechanik,
Ruhr-Universität Bochum

02/2017 – 06/2017 Industriefachpraktikum bei der Siemens AG
in Mülheim an der Ruhr im Bereich Forschung und
Entwicklung Dampfturbine

03/2016 – 04/2016 Grundpraktikum bei der Wilo SE in Dortmund
in den Bereichen Mechanische Fertigung und Montage

02/2012 Grundpraktikum bei der Hella KGaA Hueck & Co. in
Recklinghausen

Universitäre Ausbildung

seit 2023	Ernennung zum GAMM-Junior der Gesellschaft für angewandte Mathematik und Mechanik e.V.
seit 09/2019	Doktorand an der Fakultät für Maschinenbau, Ruhr-Universität Bochum, Deutschland
07/2017 – 03/2019	Master-Studium Maschinenbau, Ruhr-Universität Bochum, Deutschland Vertiefungsrichtung: Angewandte Mechanik Abschluss: Master of Science
10/2013 – 06/2017	Bachelor-Studium Maschinenbau, Ruhr-Universität Bochum, Deutschland Vertiefungsrichtung: Angewandte Mechanik Abschluss: Bachelor of Science
10/2015 – 09/2018	Abschluss von Lehrveranstaltungen des Studiengangs Mathematik, Ruhr-Universität Bochum

Schule

08/2004 – 07/2013	Städtisches Gymnasium Herten Abschluss: Allgemeine Hochschulreife
08/2000 – 07/2004	Grundschule Ludgerus in Herten

Veröffentlichungen

Blaszczyk, M. und Hackl, K.: A fully coupled two-phase bone material model. In: *PAMM* 20 (2021), Nr. 1, e202000144.

Blaszczyk, M.; Gilbert, R. P. und Hackl, K.: The effective equations for the ultrasonic response of wet cortical bone. In: *Mathematical Methods in the Applied Sciences* 44 (2021), Nr. 11, S.9096-9109.

Schlick, T.; Portillo-Ledesma, S.; Blaszczyk, M.; Dalessandro, L.; Ghosh, S.; Hackl, K.; Harnish, C.; Kotha, S.; Livescu, D.; Masud, A.; Matous, K.; Moyeda, A.; Oskay, C. und Fish, J.: A multiscale vision — Illustrative applications from biology to engineering. In: *International Journal for Multiscale Computational Engineering* 19 (2021), Nr. 2, S.39-73.

Blaszczyk, M.; Gilbert, R. P. und Hackl, K.: An effective model for cancellous bone with a viscous interstitial fluid. In: *Applicable Analysis* (2021), S.1-12.

Blaszczyk, M. und Hackl, K.: Simulations of a multiscale bone material model. In: *PAMM* 21 (2021), Nr. 1, e202100052.

Blaszczyk, M. und Hackl, K.: Multiscale modeling of cancellous bone considering full coupling of mechanical, electric and magnetic effects. In: *Biomechanics and Modeling in Mechanobiology* 21 (2022), S.163-187.

Stieve, V.; Blaszczyk, M. und Hackl, K.: Inverse modeling of cancellous bone using artificial neural networks. In: *ZAMM - Journal of Applied Mathematics and Mechanics / Zeitschrift für Angewandte Mathematik und Mechanik* 102 (2022), Nr. 6, e202100541.

Blaszczyk, M.; Jantos, D. R. und Junker, P.: Application of Taylor series combined with the weighted least square method to thermodynamic topology optimization. In: *Computer Methods in Applied Mechanics and Engineering* (2022), Nr. 393, 114698.

Blaszczyk, M. und Hackl, K.: Direct stress minimization in electro-mechanical metamaterials. In: *PAMM* 23 (2023), Nr. 1, e202200087.

Blaszczyk, M. und Hackl, K.: On the effects of a surrounding medium and phase split in coupled bone simulations. In: *ZAMM - Journal of Applied Mathematics and Mechanics / Zeitschrift für Angewandte Mathematik und Mechanik* 104 (2024), Nr. 5, e202200595.

Blaszczyk, M. und Hackl, K.: On the influence of the microstructure on multiscale bone simulations. In: *PAMM* (2024), Nr. 2, e202400040.

**Mitteilungen aus dem Institut für Mechanik
RUHR-UNIVERSITÄT BOCHUM
Nr. 196**

ISBN 978-3-935892-74-2